Infrared Telescope in Space

IRTS

Its Instrumentation and Mission

IRTS team

The Institute of Space and Astronautical Science
Yoshinodai 3-1-1, Sagamihara, Kanagawa 229, Japan

A reprint of the
ISAS Research Note 544

Table of Contents

Preface

The *Infrared Telescope in Space* (IRTS) is the first Japanese orbiting telescope dedicated to infrared astronomy. It is optimized to observe diffuse infrared emission and will survey approximately 10% of the sky at wavelengths ranging from 1 to 1000 μm during its 20-day mission. The IRTS will add significant information on a wide range of astrophysical problems, including cosmology, interstellar matter, late-type stars, and interplanetary dust.

The IRTS is a cryogenically cooled telescope and will fly aboard the space platform SFU (Space Flyer Unit). The SFU will be launched by the Japanese new rocket H-II in 1995 and will be retrieved by the Space Shuttle.

This volume is a collection of preprints, which describe the instrumentation, the capability, and the mission of the IRTS. Six papers are contained: one on its general description, four on its focal-plane instruments, and one on its optical system.

January 1994
IRTS team *

* The IRTS team consists of members from *Communications Research Laboratory* (Japan), *Institute of Space and Astronautical Science* (Japan), *Nagoya University* (Japan), *NASA Ames Research Center* (USA), *Tokyo Metropolitan Institute of Technology* (Japan), *University of California at Berkeley* (USA), *University of Tokyo* (Japan), and *University of Tsukuba* (Japan).

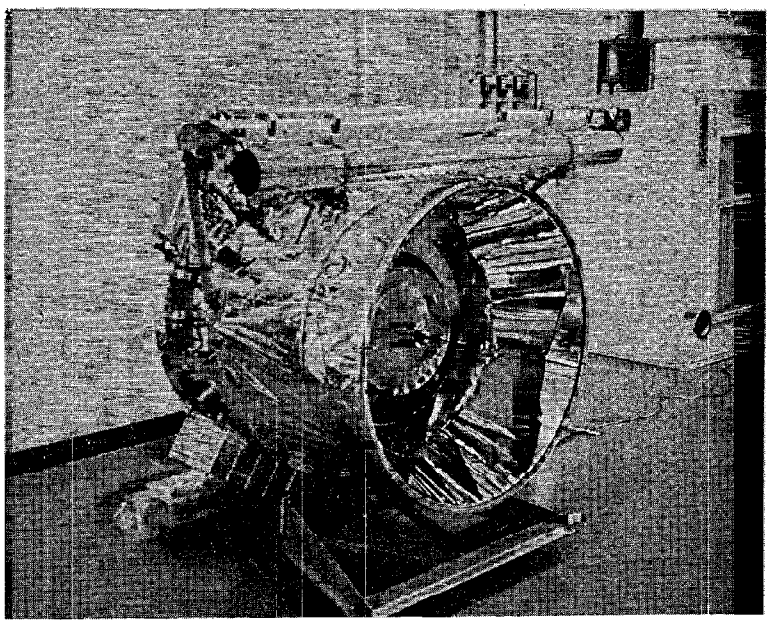

The *Infrared Telescope in Space* (IRTS).

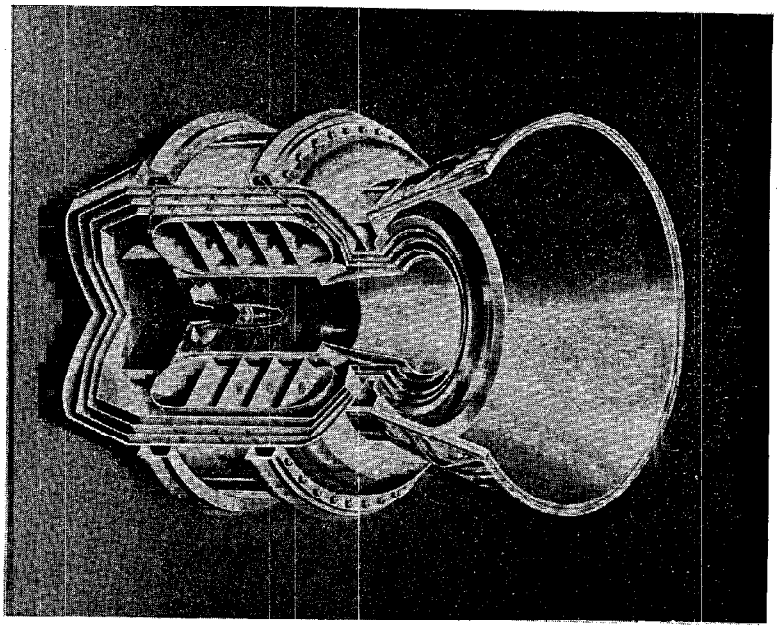

Cut-through View of the IRTS.

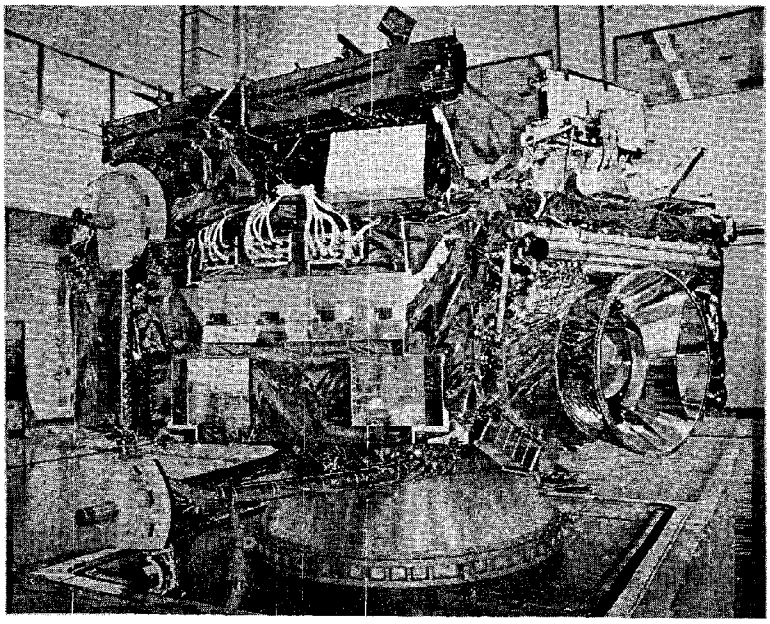

The IRTS on the *Space Flyer Unit* (SFU).

The Infrared Telescope in Space (IRTS)

H. Murakami,[1] J. Bock,[2] M. M. Freund,[2] H. Guo,[3,4] T. Hirao,[3]
A. E. Lange,[2] H. Matsuhara,[3] T. Matsumoto,[3] S. Matsuura,[3]
T. J. McMahon,[5,6] M. Murakami,[7] T. Nakagawa,[1] M. Noda,[3]
K. Noguchi,[3] H. Okuda,[1] K. Okumura,[8] T. Onaka,[8]
T. L. Roellig,[5] S. Sato,[3] H. Shibai,[1] T. Tanabe,[9] T. Watabe,[3]
T. Yagi,[10,11] N. Yajima,[1] and M.Yui [8]

Aceepted for Publication in the Astrophysical Journal

Abstract

The Infrared Telescope in Space (IRTS) is a cryogenically cooled small infrared telescope that will fly aboard the small space platform SFU (Space Flyer Unit). It will survey approximately 10 % of the sky with a relatively wide beam during its 20-day mission. Four focal-plane instruments will make simultaneous observations of the sky at wavelengths ranging from 1 to 1000 μm. The IRTS will add significant information on cosmology, interstellar matter, late type stars and interplanetary dust. This paper describes the instrumentation and mission.

Subject headings: artificial satellites, space probes - infrared: general

[1] Institute of Space and Astronautical Science, Yoshinodai 3-1-1, Sagamihara, Kanagawa 229, Japan

[2] Department of Physics, University of California at Berkeley, California 94720, USA

[3] Department of Astrophysics, School of Science, Nagoya University, Furo-cho, Chikusa, Nagoya 464, Japan

[4] Present address: Beijing Observatory, Beijing 100080, China

[5] Space Science Division, NASA Ames Research Center, Moffett Field, California 94035-1000, USA

[6] Present address: Yerkes Observatory, P. O. Box 258, Williams Bay, Wisconsin 53191, USA

[7] Institute of Engineering Mechanics, University of Tsukuba, Tsukuba, Ibaragi 305, Japan

[8] Department of Astronomy, Faculty of Science, The University of Tokyo, Bunkyo-ku, Tokyo 113, Japan

[9] Institute of Astronomy, Faculty of Science, The University of Tokyo, Mitaka, Tokyo 181, Japan

[10] Department of Mechanical System Engineering, Tokyo Metropolitan Institute of Technology, Hino, Tokyo 191, Japan

[11] Present address: Nippon Denso, Kariya, Aichi 448, Japan

1 Introduction

The Infrared Telescope in Space (IRTS) is an explorer-type instrument being developed as one of the experiments aboard the first mission of the Space Flyer Unit (SFU-1; Natori & Kuriki 1991), an unmanned, multipurpose platform facility to be launched by the Japanese HII launch vehicle and subsequently recovered by the Space Transportation System (STS) of the US National Aeronautics and Space Administration (NASA). The SFU is a multipurpose satellite on which many experiments are loaded and operated together, sharing such satellite resources as power, telemetry, launch vehicle and mission time. Infrared survey observations with a small-aperture cooled telescope are well matched to this type of mission. Such small telescopes can serve as very powerful tools for efficient surveys of extended sources with a relatively wide beam. The IRTS is the first Japanese orbiting telescope dedicated to infrared astronomy observations.

TABLE 1
Performance of the SFU (Natori & Kuriki 1991)

Item	Performance
Weight	approximately 4.0 metric tons at launch
Dimensions	4.46 m dia. x 2.8 m
Electric Power	1.4 kW (3 kW paddle generated power)
Command and Data Management System	S-band link Telemetry : 128 kbps Command : 1 kbps Data recorder : 80 Mbits Data rate : 16 kbps max.
Navigation & Guidance Control	Navigation : GPS and IMU Guidance : Onboard S/W Control : 3 axis stabilized, 1 accuracy
Reaction Control System	Hydrazine monopropellant system
Experiment resources	6 Payload Unit (PLU), 150kg/Unit Upper deck and center hole μG level : $< 10^{-4}$ G Available power for experiments : 1 kW

The advantages of infrared surveys from space have been thoroughly demonstrated in missions in the past, such as the Infrared Astronomical Satellite (IRAS; Neugebauer et al. 1984) and the Cosmic Background Explorer (COBE; Mather 1982). Such missions are totally free from atmospheric absorption and emission, and cryogenic cooling of the telescope provides a very low infrared background condition. In addition, the recent advances in detector technology enables one to observe with even higher sensitivities than in past missions.

The IRTS employs a cryogenically cooled telescope with a 15 cm primary mirror, and four focal-plane instruments that will observe the sky brightness over the 1 - 1000 μm wavelength region. The IRTS extends the wavelength coverage of IRAS to both shorter and longer wavelengths with higher sensitivity. In addition, the IRTS will add additional spectral information to the results of COBE in the near to far infrared region, where important spectral features such as the near/mid IR unidentified band emissions and far infrared [C II] and [O I] lines are found. The IRTS will also observe the submillimeter sky brightness with a higher spatial resolution than the COBE mission.

The following sections give an overview of the hardware of the IRTS and an outline of the IRTS mission, including the scientific goals.

2 Mission Description

2.1 SFU-1 and IRTS Mission

The SFU is a space-platform facility designed around an octagonal truss structure with a diameter of approximately 4.5 m (Fig.1). Eight thermal-controlled payload boxes, two of which are for the core system and six are for the user experiments, are attached to the truss. The user instruments can also be accommodated on the exposed upper deck and in the center hole. The core system of the SFU provides the electrical power, telemetry link, and attitude and orbit control to the user experiments. The SFU system performance is summarized in Table 1. The SFU has been developed by three Japanese organizations; the Institute of Space and Astronautical Science (ISAS), the National Space Development Agency (NASDA), and the Institute for Unmanned Space Experiment Free Flyer (USEF).

In the configuration used in the SFU-1, the orbit change thruster is mounted in the center hole, and the IRTS is directly attached to the SFU truss, replacing one of the payload boxes.

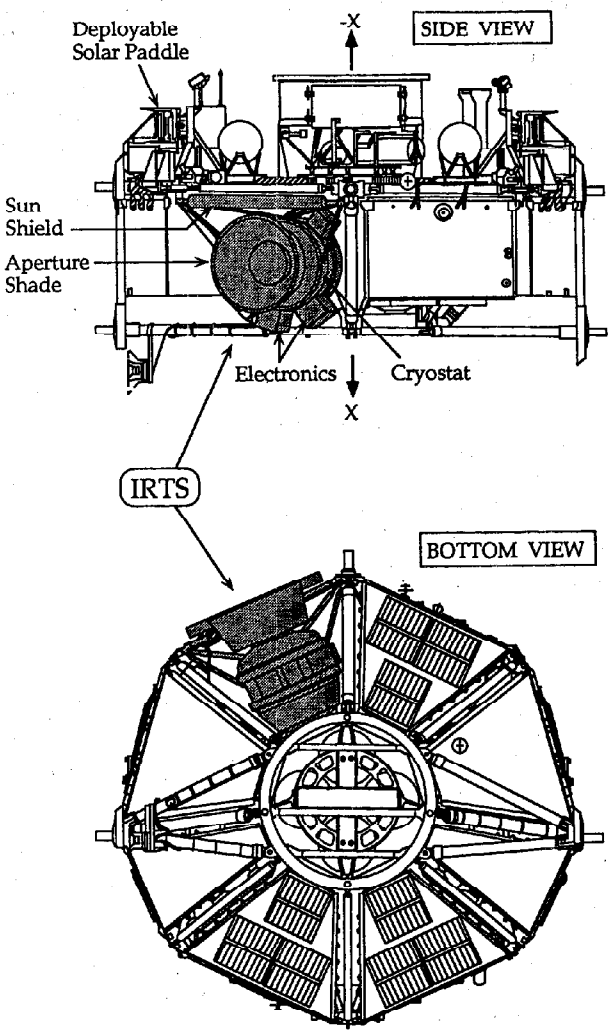

Fig.1 Side view and top view of the SFU-1. The IRTS is shaded.

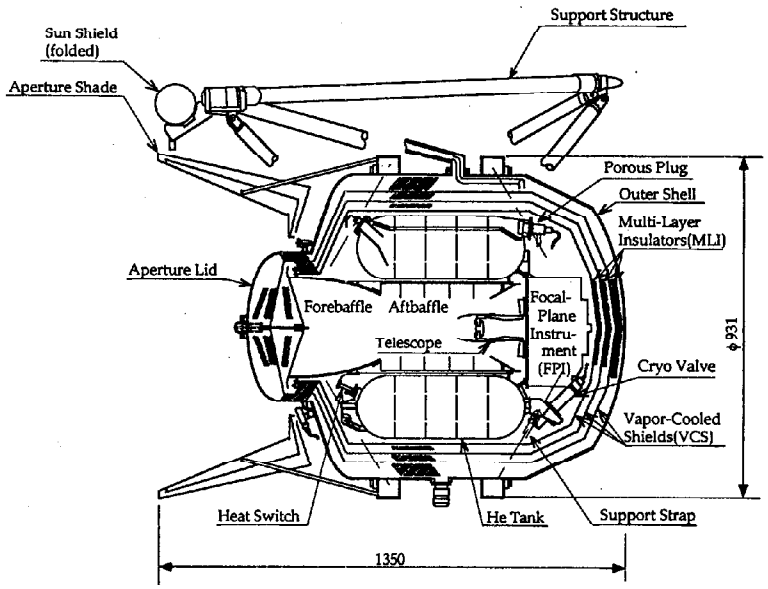

Fig.2 Cross sectional view of the IRTS. Typical dimensions are indicated in millimeters

The IRTS is a cryogenically-cooled telescope. The telescope system and the focal-plane instruments (FPIs) are contained in a cryostat whose dimensions are 93 cm in diameter and 110 cm long (Fig.2, Table 2). The aperture cover of the telescope, which is a part of the vacuum shell of the cryostat while on the ground, will be ejected in orbit. A circular aperture shade used for rejection of infrared radiation from the earth and three electronics boxes are attached to the outer shell of the cryostat. The whole system of the IRTS is attached to the SFU truss through a support structure. A deployable sun shield is fixed on this support structure.

Other SFU-1 experiments, including experiments in material science, life science, and some technology demonstrations, are accommodated in the remaining five payload boxes and on the upper deck. The launch weight of the complete SFU-1 is approximately 4 metric tons.

TABLE 2
Specifications of the IRTS

Item	Characteristics
Weight	Total weight : 183 kg
	Cryostat : 128 kg
	FPI +telescope : 9 kg
	Electronics : 16 kg
	Support structure : 18 kg
	Others : 12 kg
Dimensions	93 cm dia. (cryostat) x 135 cm (including aperture shade)
Power Consumption	80 W max.
Cryostat	Superfluid helium 90 liters
	FPI temperature : 1.9 K
	Cold lifetime : > 35 days after launch
Telescope	15 cm dia., F/4 Ritchey-Chretien type
	Effective collecting area : 113 cm^2
Focal plane instruments	Near-Infrared Spectrometer (NIRS)
	Mid-Infrared Spectrometer (MIRS)
	Far-Infrared Line Mapper (FILM)
	Far-Infrared Photometer (FIRP)
Telemetry	Data rate : 6 kbps (visible orbit) / 3 kbps (invisible orbit)
Observation	20 days, uniform sky survey
Sky coverage	approximately 10 % of the entire sky

The SFU-1 is scheduled to be launched in February 1995 by an HII launch vehicle which is under development by the NASDA. The SFU-1 will be initially injected into a low-earth orbit. Thirty minutes after launch, the IRTS electrical power will be turned on and the dedicated experiment processor (DEP) will automatically open the helium vent valve. The SFU-1 system will spend the first several days on-orbit in a checkout of the core system. During this period, the SFU will move up to the experiment operation orbit, a circular orbit of approximately 500 km altitude and 28.5 degrees inclination. This time will also be used in degassing the satellite surfaces.

The IRTS experiment will commence by deploying the sun-shield and ejecting the aperture lid. The IRTS observations will last for 20 days.

During this observation period, the IRTS will survey approximately 10 % of the entire sky, and will make absolute measurements in the near/mid infrared and submillimeter regions. In addition, the IRTS will also survey far-infrared fine-structure line intensities of carbon ions and oxygen atoms.

The down links of the IRTS telemetry data will be supported by the Kagoshima Space Center of the ISAS and three receiving stations of NASA s Deep Space Network (DSN), located at Goldstone, Canberra and Madrid. In about 2/3 of the observation orbits, the IRTS will be visible from these stations at least once per orbit and will generate data at the rate of 6 kbps. For those orbits where the IRTS will not pass over a ground station, the IRTS data rate will be reduced to 3 kbps. The data acquired by the Kagoshima Space Center will be transferred to the Sagamihara Operations Center (SOC) of ISAS in real-time and those acquired by the DSN stations will be transferred to the SOC through the Jet Propulsion Laboratory with a one-hour delay. The data will then be distributed to each experiments monitor systems.

After the IRTS observation period, the sun-shield will be ejected to allow for recovery by NASA s STS system. The SFU will descend to the retrieval orbit of 315 km altitude at the end of its six-month mission and will then be retrieved by the Space Shuttle.

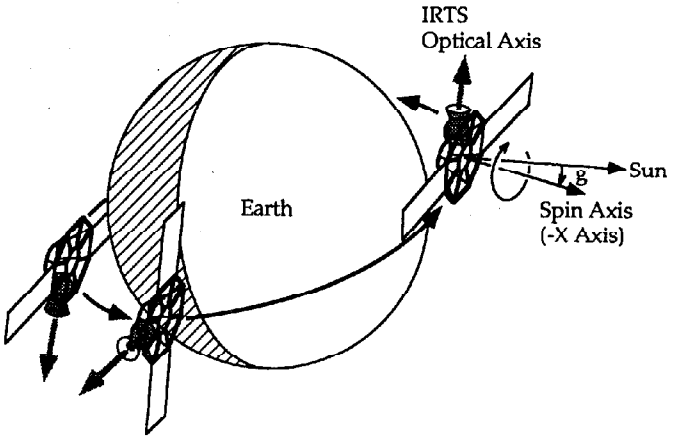

Fig.3 Attitude control of the IRTS in the mode-1 is illustrated.

2.2 Attitude Control and Sky Survey

The IRTS itself has no pointing capability. The scan paths in the sky are determined by maneuvering the entire SFU system. The SFU-1 will be operated in the solar-oriented attitude where the -X axis of the SFU-1 (see Fig.1) is pointed to the sun. During the IRTS observations, the SFU is rotated around this -X axis once an orbital revolution at a constant rate. As the optical axis of the IRTS is perpendicular to the -X axis, this attitude results in the IRTS scanning the sky along great circles at right angles to the sun (Fig. 3). The sky observed by the IRTS will change at a rate of approximately one degree per day with the orbital motion of the earth around the sun.

The IRTS rotation direction and phase will be determined so as to maximize the angular distance from the IRTS optical axis to the earth limb. There are basically two scanning modes. At the center of the day side on the orbit, the IRTS is directed to the north when the SFU passes through the northern side of the subsolar point (mode 1), or directed to the south when the SFU passes through the southern side (mode 2). Figure 3 shows the SFU attitude in mode 1. The rotation direction in the mode 2 is in the opposite

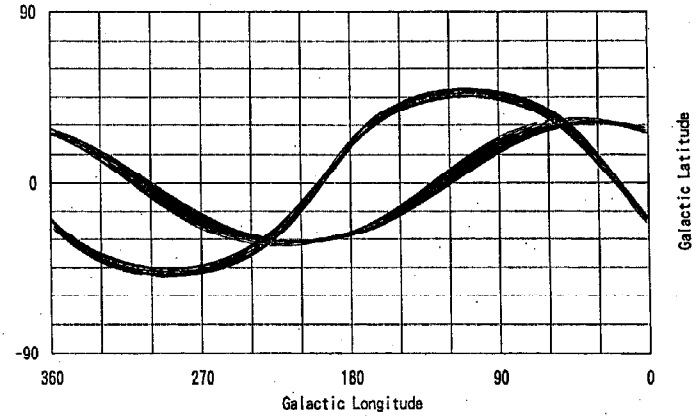

Fig.4 An example of the observed sky area is shown in galactic coordinates. A launch at UT 9h20m on Feb. 15 is assumed. The scan mode is changed from mode 1 to mode 2 in the middle of the observation period, and the two bands in the figure correspond to the observing areas before and after the mode change.

direction. As shown in Figure 3, the -X axis is in fact slightly off of the sun line (angle g in the figure), southwardly or northwardly depending the scanning mode, to avoid infrared radiation from the earth limb, which is only 22 degrees below the horizontal direction on the spacecraft.

The required attitude control depends on the date and the time of launch and when the IRTS will begin its observations. Therefore, the final attitude control sequence, including the selection of the mode mentioned above and detailed optimization, will be determined once the SFU-1 is launched. Figure 4 shows an example of the observed sky area. This figure assumes that the SFU will be launched at UT $9^{h}20^{m}$ on February 15, 1995 and that the IRTS will start observations on the 8th day after launch. In addition, the attitude control mode is assumed to change from mode-1 to mode-2 on the 17th day after launch.

The accuracy of the SFU attitude-control system is $\sim$ 1 degree. The actual scan path will be reconstructed to an accuracy of 1 arcminute after the mission using the data from the gyroscopes of the SFU core system and the IRTS star sensor, which is located on the IRTS telescope focal plane together with the FPIs.

3 IRTS Mission Hardware

3.1 Cryostat

A cross sectional view of the IRTS cryostat is given in Figure 2. A complete description of the IRTS cryostat is given in by Murakami et al. (1990). The cryostat has a torus-shaped liquid helium tank with a volume of one hundred liters. This tank will be filled to 90 % full with super-fluid helium by two successive transfers shortly before launch. In the first transfer, the tank will be filled with normal helium and then pumped to convert the helium to a super-fluid state. In the second transfer, the tank will be filled with helium at a temperature slightly higher than the lambda point and the tank will then be pumped again. The pumping will last until eleven hours before launch in the present operation schedule. The helium tank will be closed during the ascent of the vehicle and then opened to outer space to continue the evacuation.

The telescope and the FPIs are attached at the bottom of the helium tank and operate at a temperature of 1.9 K. The helium tank is suspended from the outer vacuum shell by twelve support straps which are made of glass fiber-reinforced plastic. Three vapor-cooled shields (VCS) to shield the helium tank from infrared radiation are also supported by these straps.

A porous plug made of alumina ceramics is employed as a phase

separator, separating the vapor from the liquid helium in zero gravity. The helium gas evaporated through the porous plug first cools the forebaffle and then circulates through the vapor-cooled shields.

The aperture lid has two radiation shields. These shields are passively cooled by thermal contact with the outer VCS and the forebaffle. The aperture lid will be ejected by springs at the beginning of the IRTS observation period.

The thermal performance of the cryostat has been evaluated by numerical model calculation and confirmed by testing. The temperature distribution results are compiled in Table 3. The heat load to the helium tank is about seventy milliwatts, half of which is due to heat conduction through the support straps. The FPIs generate about 10 milliwatts. The expected hold time of the liquid helium is greater than 35 days after launch, under standard conditions.

TABLE 3
Temperature distribution of the cryostat in orbit

Position	Case 1[a)]	Case2[b)]
	Conditions	
Outer Shell[c)]	300 K	300 K
Aperture heat load[d)]	10 mW	200 mW
Heat Switch[e)]	ON	OFF
	Temperatures	
Outer Vapor-Cooled Shield	201.3 K	191.6 K
Middle Vapor-Cooled Shield	107.5 K	96.5 K
Inner Vapor-Cooled Shield	24.3 K	26.1 K
Forebaffle	2.6 K	18.7 K
He Tank	1.9 K	1.9 K

a) The expected best case. The requirements of sun and earth avoidance are both satisfied.

b) The worst case. Radiation from the earth directly iluminates the upper part of the forebaffle. The heat switch is turned off to reduce the heat load to the helium tank.

c) The acurate calculation of the outer shell temperature is very difficult, because of the complex structure of the SFU. A temperature of 300 K is assumed here for both cases.

d) Heat absorbed by the forebaffle.

e) Heat switch for the forebaffle (see text).

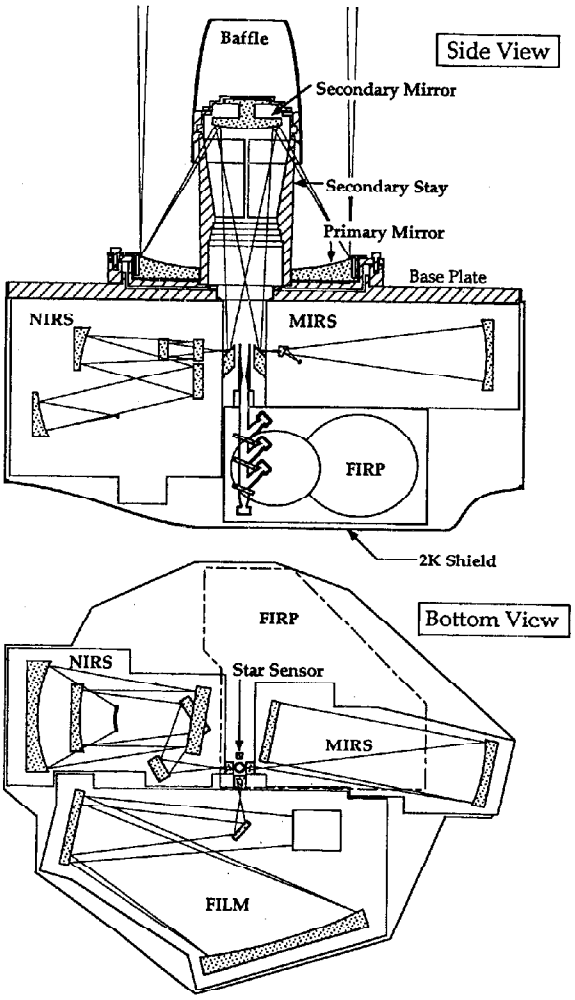

Fig.5 The arrangement of the telescope system and the focal-plane instruments.

3.2 Telescope and Baffling System

The IRTS telescope is a Richey-Chretien system with a effective diameter of 15 cm and a focal length of 600 mm, F/4 (Onaka et al. 1993). The mirrors are made of aluminum alloy, cut by a high-precision numerically-controlled machine, and coated with Ni before final cutting and polishing. The surface of the mirrors are coated with 0.2 μm of gold and 0.1 μm of SiO_2.

The primary mirror cell and the secondary mirror support are also made of aluminum alloy to minimize the degradation of the image quality due to differential thermal contraction. A schematic view of the telescope system together with the focal-plane instruments is given in Figure 5. The secondary mirror is supported by four stays from the central hole of the primary mirror. This configuration prevents the supporting stays from being directly illuminated by stray light scattered from the forebaffle.

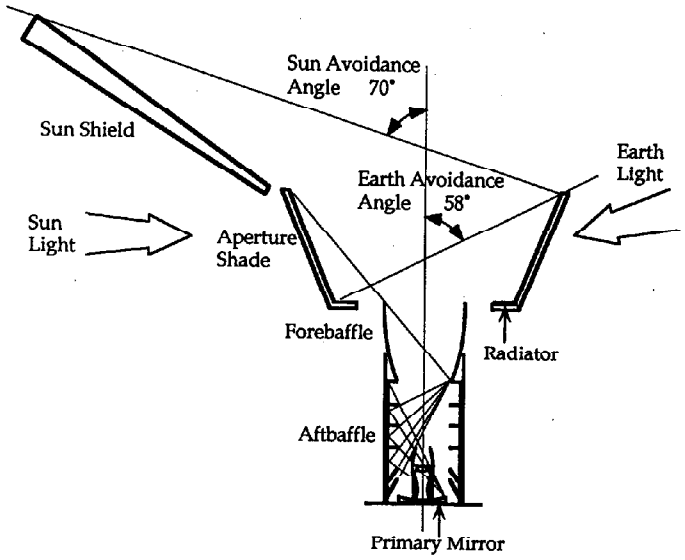

Fig.6 The IRTS baffle system.

Because the IRTS intends to make absolute measurements, good side-lobe rejection is required for the baffling system. Figure 6 shows the concept of the baffle system (Sato et al. 1993). The sun-shield is a carbon fiber-reinforced plastic sheet, 2 meters long, covered with an aluminized teflon film on the surface that is illuminated by sunlight. The sun-shield is stowed rolled up on the ground and is deployed in orbit to block the direct incidence of sunlight into the aperture shade. The aperture shade has a specular inner surface that reflects the thermal radiation from the earth and the sun-shield. It has two layers of radiation shielding and is cooled to below 200 K by a radiator located at the bottom. The forebaffle is a Winston-type reflector (Winston 1970) made of aluminum alloy coated with Au and reflects the thermal radiation of the aperture shade back to the sky. This reflecting forebaffle is essential for the cryostat design, since it reduces the aperture heat load considerably and makes the cryogenic system more compact. The forebaffle is usually cooled by evaporated helium to about 10 K. It can be cooled to below 4 K, depending on the observation mode in use, by a thermal connection to the helium tank through a heat switch, making the thermal emission negligible even in the submillimeter region. The heat switch utilizes copper cylinders separated by a small gap which is filled or emptied with helium gas to achieve the switching action (Duband, Hui & Lange 1990). The last stage of the baffle system is the aftbaffle which consists of a set of annular vanes. The aftbaffle is coated with a special paint which was chosen for its mechanical strength and its nearly perfect black properties from the near-IR to millimeter wavelengths (Bock & Lange 1993).

The combined performance of the forebaffle and the aftbaffle was evaluated at visible wavelengths in the laboratory and a high sub-millimeter side-lobe rejection was confirmed by a rocket experiment at 90 μm and 180 μm (Bock et al., 1993a).

3.3 Focal Plane Instruments

Four scientific instruments, the Near Infrared Spectrometer (NIRS), the Mid Infrared Spectrometer (MIRS), the Far Infrared Line Mapper (FILM) and the Far Infrared Photometer (FIRP) are installed in the focal plane of the telescope together with a near-infrared star sensor.

The NIRS is a spectrometer with a fixed grating and linear InSb arrays (Noda et al. 1993). It covers the shortest wavelengths of the IRTS coverage, from 1.4 μm to 4.0 μm, with a moderate resolution, $\Delta\lambda = 0.12$ μm. The detectors consist of two twelve-element InSb photodiode arrays aligned in the dispersion direction. Twenty-four channel charge integrating amplifiers, which are constructed with JFETs, are operated at about 70 K with a

readout noise of approximately 150 electrons.

The MIRS is a very simple and light-weight spectrometer covering the 4.5 to 11.7 μm wavelength range (Roellig et al. 1993). The light passing through the entrance slit is dispersed and refocused by a concave grating onto 32 off-axis parabolic field mirrors, which then focus the dispersed image onto 32 Si:Bi photoconductive detectors. The newly developed grating has variable line spacings and blaze angles. This grating realizes an astigmatism-free image and a flat focal plane at a given wavelength. The spectral resolution ranges from a minimum of 0.23 μm at a wavelength of 6.7 μm to 0.36 μm at 10.8 μm.

The FILM is also a grating spectrometer. This instrument has the highest spectral resolution, $\lambda/\Delta\lambda \sim 400$, among the four FPIs and is designed to observe the fine structure lines emitted by carbon ions and oxygen atoms (Shibai et al. 1993). A similar grating design to that employed in the MIRS was also adopted for the FILM. The FILM grating has a cylindrically concave shape and gradually varying line spacings. The [C II] and the [O I] lines are detected by stressed and non-stressed Ge:Ga photoconductive detectors, respectively. The FILM also has continuum channels at 155 μm and 160 μm, one on either side of the [C II] line wavelength.

The FIRP is a four-channel photometer covering the submillimeter wavelength region (Lange et al. 1993). Filters and dichroic beam splitters separate the incident light into four wavelength bands. The center wavelengths are approximately 140 μm, 230 μm, 400 μm and 700 μm. Each channel has a matched pair of composite bolometers, one illuminated by incident light and the other in a dark cavity. Each pair is biased in an AC bridge. Lock-in amplifiers detect only the difference of signals from paired bolometers, producing a stable output signal proportional to absolute power (Wilbanks 1990). The bolometers are cooled to 300 mK by a closed cycle ^{3}He refrigerator (Duband, Hui & Lange 1990).

A Ge photodiode with a slant mask is placed at the focal plane as a star sensor. The wavelength band, which is determined by the spectral response of the Ge photodiode operated at 2 K itself, is similar to the standard infrared J-band. The Ge photodiode has a 17 arcminutes square field of view and will detect stars brighter than $m_J = 6$ mag (5σ). Using this star sensor, the data from the gyroscopes can be calibrated once every few minutes with an accuracy of 0.02 degrees.

The NIRS, MIRS and FIRP have cold shutters, which are periodically closed during the observation in order to calibrate zero signal levels. All of the instruments except the star sensor have internal light sources of proper color temperatures which allow the detector responsivities to be periodically measured in flight.

Figure 5 shows the arrangement of the instruments on the focal plane. The NIRS, MIRS and FILM have ≈ 45-degree mirrors in front of the entrance slits and pick off beams 1 degree off of the optical axis. The FIRP uses the on-axis beam to achieve the best side-lobe rejection of the baffling system. The star sensor is also located at 1 degree off the optical axis. All of the FPIs are surrounded by a shield cooled to a temperature of approximately 2 K to reject the far-infrared emission from the vapor-cooled shields. The 2 K-shield was made of thin aluminum plates and aluminum foil lined with Kapton film.

The FPI system with the flight telescope was tested in the laboratory using a special test cryostat prior to installation to the flight cryostat. The test cryostat had a vacuum window and a neutral-density filter system to introduce an infrared beam from external light sources at backgrounds similar to those expected on-orbit. The beam pattern and responsivity of each FPI was evaluated in this configuration, except for the FIRP responsivity, which was measured with a low-temperature blackbody source inside the test cryostat.

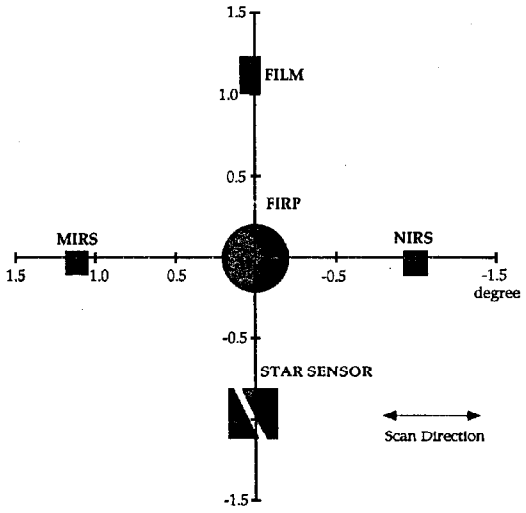

Fig.7 FPI field of view. Each shaded figure shows the relative position of the beam and the FWHM beam size. The shapes are rendered schematically only.

The FPI system was then installed into the flight cryostat and the performance was checked in a dark condition with a cold cover over the telescope forebaffle. In this test, no measurable light leak was detected by any instrument, a very important result for absolute measurements. We found an unknown light source inside the FILM, but it did not affect zero signal levels of the FPIs other than the FILM. The noise performance, including the effects of electrical interference among the FPIs and the other electronics components, was then evaluated. The noise floor due to electrical interference and cold preamplifier noise contributed equally to the noise performance of the NIRS and the MIRS. However the sensitivity of the MIRS will be limited by the Poisson noise of the relatively strong Zodiacal background in all but the very shortest wavelength channels. The noise due to the unknown internal light source and the electrical interference dominate for the FILM. The major noise source for the FIRP and the star sensor is the electrical interference.

Figure 7 shows the measured FPI beam sizes (FWHM) and the relative beam positions projected on the sky. The beams of the NIRS and the MIRS are aligned in the scan direction and they will observe approximately same sky region with a time delay of about 30 sec.

The 1s sensitivity of each instrument per field of view calculated from the measured laboratory performance is shown in Figure 8, with the brightness of some known extended sources. The integration time is approximately 64 seconds for FIRP, 6 seconds for FILM and 4 seconds for MIRS and NIRS. The IRTS sensitivity is compared with the sensitivity for IRAS (Neugebauer 1984) and the DIRBE and the FIRAS instruments on the COBE mission (Hauser et al. 1992). The NIRS and the MIRS are less sensitive than the DIRBE instrument, but they have a higher angular and spectral resolution with nearly continuous coverage from 1.4 to 12 μm. The FILM has similar spectral resolution to that of the FIRAS instrument near 100 μm, but has much higher sensitivity and angular resolution. The FIRP has angular resolution similar to that of the DIRBE, but has much higher sensitivity. A summary of the characteristics of the four FPIs is given in Table 4.

3.4 The Electronics and Telemetry Data System

The electronics system of the IRTS consists of three parts, a dedicated experiment processor (DEP), a data processing unit (DPU), and the FPI electronics (FPI-E). The FPI-E amplify the signals from the four FPIs and the Ge star sensor, and converts them to digital data of 16 bit length. In addition, this electronics package adjusts the bias voltages of the infrared sensors and drives the cold shutters and internal calibration sources

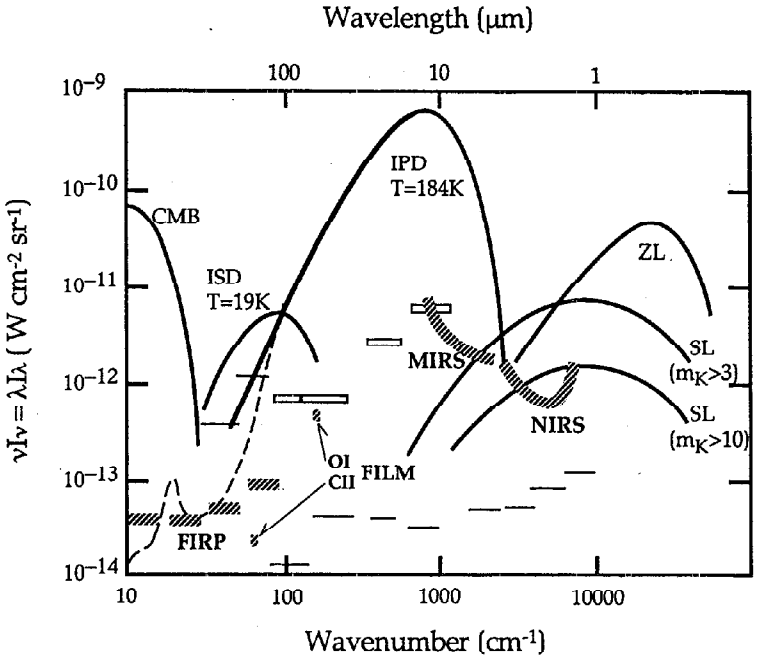

Fig.8 Detection limits of the focal plane instruments are indicated by hatched patterns. For the FILM, line intensities detectable with 1s are plotted. The detection limits are 1s per field of view, based on the measured laboratory performance of the fully integrated system. Solid lines show components of the sky brightness, zodiacal light (ZL), thermal emission of the interplanetary dust (IPD), integrated star light (SL), thermal emission of the interstellar dust (ISD), and 2.74 K cosmic background radiation (CMB). For the integrated star light, the contributions from stars fainter than 3 mag at K band and from only stars fainter than 10 mag are shown.

The 1s sensitivity of the COBE/DIRBE experiment (horizontal bar), the COBE/FIRAS experiment (dashed line) for a one-year mission (from Fig. 3. of Hauser et al. 1992) and the IRAS survey (open rectangle; Neugebauer et al. 1984) are also shown

TABLE 4
FPI Characteristics

Item	Focal Plane Instruments NIRS	MIRS	FILM	FIRP
Optical System	Grating Spectrometer	Grating Spectrometer	Grating Spectrometer	Wide-band Photometer
Wavelength Coverage	1.4 - 4.0 μm	4.5 - 11.7 μm	63 μm ([OI]) 158 μm ([CII]) 155, 160 μm (continuum)	140, 230, 400, 700 μm
Wavelength Resolution	Δλ = 0.12 μm	Δλ = 0.23 - 0.36 μm	λ/Δλ= 400 for [OI]&[CII] λ/Δλ= 150 for continuum	λ/Δλ= 3
Beam Size	8 x 8	8 x 8	8 x 13	30 circle
Detector System	Two InSb 12-element Arrays	Si:Bi x 32	Ge:Ga x 1 Stressed Ge:Ga x 3	0.3K bolometer x 4
	Charge Integrating Amplifiers	Charge Integrating Amplifiers	TIAs	AC-biased Bridge Circuit

according to the commands. The DPU processes the house-keeping signals, which come mainly from thermometers in the cryostat. For the house-keeping data, the word length is 8 bits.

Each experiment onboard the SFU-1 has its own microprocessor, and this processor controls the sequence of the experiment. The control of the IRTS observation sequence, however, is very simple, because the observation is a uniform sky survey. The IRTS DEP only generates the command sequences for an automatic in-flight calibration of the FPIs. The most important of these sequences are the commands for the FPI shutter open/close and calibration source on/off which are used to check sensitivity changes and zero-level drifts of the FPI signal output. This calibration sequence will be done every 17.5 minutes during the IRTS observation period.

The most important job of the DEP is to handle the telemetry data. The DEP gathers the data of the FPIs and the house-keeping system following a given telemetry format and passes them to the Command and Data Management System (CDMS) of the SFU. The IRTS has three telemetry modes. The telemetry format-1 is designed for a normal observation mode, where the IRTS generates data at the rate of 6 kbps and the data are sent to the ground once every orbital revolution. The FPI data occupies 94 % of 6 kbps and the house-keeping data and other engineering data the remaining 6 %. In orbits where the IRTS does not pass over a receiving station, the data rate is limited by the capacity of the on-board data recorder. During these orbits, the DEP reduces the data rate to one half of the normal mode, 3 kbps (telemetry format-2), by halving the sampling rate of all the data except for the NIRS. The data of only odd-number detectors of the NIRS are sampled in this telemetry mode. The last mode is a standby mode where only the house-keeping data are sent to the ground with a very low data rate, about 24 bps. The telemetry mode change is performed by commands from the ground. Those commands, as well as other control commands of the IRTS, are first stored in the main computer of the SFU-1, and subsequently passed to the IRTS DEP at a given time to be executed.

The aperture-lid open and the Sun-shield deploy/jettison are performed using pyro-devices, which are directly controlled by the core system of the SFU-1.

The characteristics of the IRTS hardware are summarized in Table 2.

4 Scientific Goals

4.1 Interplanetary Dust

The IRAS mission observed the thermal emission from the interplanetary dust in the mid to far infrared range at solar elongation angles near 90 (Hauser et al. 1984). However, the IRAS could not take spectra of this observed dust emission. The information on the scattered sunlight by the planetary dust is also still poor in the infrared region compared with that from optical and UV wavelengths.

The size distribution and the composition of the interplanetary dust will affect the infrared spectra of both the scattered light and the thermal emission. The nearly continuous spectra obtained by the NIRS and the MIRS in the wavelengths range from 1.4 μm to 11.7 μm, which includes the silicate feature at 9.7 μm, is an ideal tool for investigation of the interplanetary dust.

4.2 Interstellar Matter

The observations of interstellar matter are one of the major target of the IRTS mission. The FIRP sensitivity, spectral coverage and angular resolution enable it to study the emission from cold interstellar dust particles which comprise most of the dust mass. These measurements will yield a basic knowledge of the total mass of the dust clouds.

COBE experiment has found evidence for a low frequency (< 30 cm^{-1}) excess in the sub-millimeter spectra of the interstellar dust, that may be due to very cold (4.77 K; Wright et al. 1991) dust. The FIRP covers the entire spectral range from 100 μm to 1 mm, thus covering the region where emission from the cold dust component should be observable. The FIRP will determine whether this cold component is morphologically distinct from the warm (≈ 20 K) component on angular scales of 0.5 .

The spectra of the diffuse clouds have a hot component which is bright in the mid-infrared as well (Boulanger et al. 1985). This component is postulated to be due to very small dust particles transiently heated by a single UV photon. These very small particles are also believed to be the origin of the infrared band emissions located at 3.3, 3.4, 6.2, 7.7, 8.6, and 11.3 μm. The NIRS and the MIRS have a sensitivity to detect even weak features from the clouds illuminated by the general interstellar UV field without nearby sources. These two instruments will study the spatial variation of these features within the galaxy.

The UV photons which hit the dust particles also dissociate molecules

and heat up the gas in the clouds through a photo-electric heating process. The FILM will trace the resulting warm gas by observing the [C II] and the [O I] lines. The [C II] line at $\lambda = 158$ μm is the most important cooling agent of the warm gas and is therefore a very important probe to study the physical states of the interstellar clouds and the UV fields.

Recent observations have shown that the [C II] line is detected everywhere in the galactic plane (Shibai et al., 1991; Nakagawa et al., 1992) and at high galactic latitudes (Bock et at. 1993b). The origin of this diffuse [C II] emission is still uncertain. The [O I] line intensity simultaneously observed with the [C II] line will make it clear whether the [C II] line comes from the diffuse photodissociation regions or the extended HII regions, where is no neutral oxygen. In addition to the above, the [O I] line has been believed to be emitted from a interstellar gas heated by a shock wave (Hollenbach and McKee, 1989). The [O I] channel of the FILM will also trace the shocked regions around supernova remnants and in star forming regions.

4.3 Stars

Although the IRTS mission is optimized for observations of extended sources, it will also observe many point sources as well, such as late-type stars, stars with mass losses, planetary nebulae and so forth. The NIRS and the MIRS can together cover the wavelengths from 1.4 to 11.7 μm where important molecular bands, such as water vapor, ice, CO, silicate are included. In addition, the sensitivity of the MIRS is a factor of 5 higher than the similar instrument, the Low Resolution Spectrometer (LRS) in the IRAS mission over their overlapping wavelength ranges because of the advances in detector technology. The IRTS is therefore an ideal tool for a systematic study of the structure, atmosphere and evolution of the late-type stars and stars in the late stages of evolution.

4.4. Extragalactic Background Radiation

As shown in Figure 8, the brightnesses of the known extended sources are weak in the 3 to 4 μm and 300 to 500 μm regions, providing windows to search for extragalactic light. It has been theoretically predicted that there is a background radiation, other than the famous cosmic microwave background light, that is due to the integrated light from all galaxies on the line of sight out to the distance of galactic formation. The large amount of UV and visible radiation emitted when the galaxies were formed will be redshifted to the near-infrared wavelength range and may be detected. The extra-galactic radiation converted to far infrared light by any dust in the

galaxies should be observable in the submillimeter region. Some attempts to measure this background light have been made using sounding rockets (Noda et al. 1992) and the DIRBE experiment of the COBE has made an extensive search .(Hauser et al. 1992), but definite results have not been obtained yet. This situation is due to the fact that the observation requires an absolute measurement of the sky brightness; and the separation of the isotropic background from the foreground emission is a very difficult matter. A systematic search, independent of past observations, is therefore absolutely necessary. The NIRS, which covers the near-infrared window, is able to detect stars brighter than 8 mag at 2 μm. We can reduce the integrated light from stars in the Galaxy, one of the sources of foreground radiation, by removing the contribution of those stars from the measured brightness. The observation of the interplanetary dust emission by the MIRS is also very important for the separation of the foreground radiation. The FIRP will measure the diffuse background in the deep sub-mm window near 400 μm with greater angular resolution than FIRAS, which will assist in the identification and subtraction of local sources of emission.

The observations of the interstellar dust emission by the FIRP will also play an important role in the search for the anisotropy of the cosmic microwave background, the seeds of the observed structure in the present-day universe. Several experiments to measure the anisotropy with angular scales smaller than those found by the COBE experiment (Smoot et al. 1992) have been designed and are now operating in millimeter-wavelength range (Fischer et al. 1992). Confusion by interstellar dust emission will ultimately limit the sensitivity of the cosmic background anisotropy at wavelengths below 3 mm. Observations by the FIRP in the sub-millimeter region will improve the precision with which mm-wavelength interstellar dust emission can be modeled and subtracted from cosmic microwave background anisotropy measurements.

5 Conclusions

The IRTS is the first ISAS mission for infrared astronomy. It was initially planned as a step toward regular infrared-astronomy space missions of ISAS in the future. The IRTS has already contributed to advance of space cryogenics and infrared-detector technology in Japan. All four focal-plane instruments have been installed in the flight-model cryostat and their performance has been confirmed. The IRTS will make valuable contributions to a wide range of astrophysical problems.

We thank K. Kuriki, the project manager of the SFU, M. Natori of

ISAS and other SFU-1 team members for the kind support of the integration of the IRTS into the SFU-1.

Many people have contributed to the IRTS project. We especially thank T.Kono of Tokyo Metropolitan Institute of Technology for his support to the test of the telescope system, M. Narita of ISAS for management in the testing at ISAS, and N. Hiromoto of the Communication Research Laboratory for preparation of the detectors for the FILM.

We would also like to acknowledge corporate contributions to the IRTS project under contract to the ISAS. The system integration was performed by NEC Corporation. The cryostat was built by Sumitomo Heavy Industries. Nikon prepared the telescope and some mirrors for the FPIs. The mirror supports of the telescope system and mechanical structure of NIRS, MIRS, FILM were built by Mitaka Koki Co. Ltd.. The detector system of the NIRS was developed by Hamamatsu Photonics K. K. (HPK) under collaboration with Nagoya University. HPK also provided the signal-processing electronics for FPIs.

The fabrication of two of the four FPIs, the MIRS and the FIRP, have been financially supported by the NASA grants program. T. Yagi was supported by the Konica-Tachibana foundation during his work on IRTS.

References

Bock, J., Matsuhara, H., Matsumoto, T., Onaka, T., Sato, S., & Lange, A. E.1993a, Applied Optics, submitted

Bock, J. et al. 1993b, ApJ, submitted

Bock, J. & Lange, A. E. 1993, Applied Optics, submitted

Boulanger, F., Baud, B., & van Albada, G. D. 1985, A&A, 144, L9

Duband, L., Hui, L., & Lange, A. E. 1990, Cryogenics, 30, 263

Fischer, M. L. et al. 1991, ApJ, 388, 242

Hauser, M. G. 1984, ApJ, 278, L15

Hauser, M. G., Kelsall, T., Moseley, S. H., Silverberg, R. F., Murdock, T., Toller, G., Spiesman, W., & Weiland, J. 1991, in After the First Three Minetes, eds. S. S. Holt, C. L. Bennett, & V. Trimple, (New York: AIP Conf. Proc. 222), 161

Hollenbach, D., & McKee, C. 1989, ApJ, 334, 771

Lange, A. E., Freund, M. M., Sato, S., Hirao, T., Matsumoto, T., & Watabe, T. 1993, ApJ, in press

Mather, J. C. 1982, Opt. Engineering, 21, 769

Murakami, M. et al. 1990, in Advanced Cryogenic Engineering, Vol.35, ed. R. W. Fast (New York: Plenum Press), 295

Nakagawa, T., Doi, Y., Mochizuki, K., Yui, Y., Okuda, H., Yui, M., Shibai, H., Nishimura, T., & Low, F. J. 1993, Back to the Galaxy, eds. S. S. Holt & F. Verter, (New York: AIP Conf. Proc. 278), 303
Natori, M., & Kuriki, K. 1991, Space Technol., 11, 159
Neugebauer, G., et al. 1984, ApJ, 278, L1
Noda, M., Christov, V. V., Matsuhara, H., Matsumoto, T., Matsuura, S., Noguchi, K., Sato, S., & Murakami, H. 1992, ApJ, 391, 456
Noda, M., Matsumoto, T., Matsuura, S., Noguchi, K., Tanaka, M., Lim, M. A., & Murakami, H. 1993, ApJ, in press
Onaka, T., Yagi, T., Shibai, H., Murakami, H., Tanabe, T., & Kohno, T. 1993, Applied Optics, in press
Roellig, T. L., Onaka, T., McMahon, T. J., & Tanabe, T. 1993, ApJ, in press
Shibai, H., et al. 1991, ApJ, 374, 522
Shibai, H., Yui, M., Matsuhara, H., Hiromoto, N., Nakagawa, T., & Okuda, H., 1993, ApJ, in press
Sato, S., et al. 1993, in preparation
Smoot, G. F., et al. 1992, ApJ, 396, L1
Wilbanks, T., Devlin, M., Lange, A. E., Sato, S., Becman, J. W., & Haller, E. E. 1990, IEEE Transactions on Nuclear Science, 37, 566
Winston, R. 1970, J. Opt. Soc. Am., 60, 245
Wright, E. L., et al. 1991, ApJ, 381, 200

Near-Infrared Spectrometer on the Infrared Telescope in Space (IRTS)

Manabu Noda,[1] Toshio Matsumoto,[1] Shuji Matsuura,[1]
Kunio Noguchi,[1] Masahiro Tanaka,[1] Mark A. Lim,[1,2]
and Hiroshi Murakami[3]

Accepted for Publication in the Astrophysical Journal

Abstract

The Near-Infrared Spectrometer (NIRS) is a grating spectrometer with two 12 element InSb linear arrays, and is one of the four focal plane instruments of the Infrared Telescope in Space (IRTS) mission, which will be launched in early 1995. The NIRS was designed to measure the absolute sky brightness with coarse spectral resolution; searching for extragalactic background light is the primary purpose of our observations. The wavelength coverage of the NIRS ranges from 1.4μm to 4.0μm with a spectral resolution of 0.12μm. The field of view is $8' \times 8'$. The NIRS has been calibrated and tested with the flight IRTS telescope in the laboratory. The response and noise were found to be as expected from the design values. After integrating all of the focal plane instruments with the telescope into the flight cryostat, NIRS shows good performance and will be able to achieve a high sensitivity in orbit.

Subject headings: artificial satellites, space probes – instrumentation: spectrometers – infrared: general

---

[1] Department of Astrophysics, School of Science, Nagoya University, Chikusa-ku, Nagoya 464-01, Japan

[2] Present address: Physics Department, University of California at Santa Barbara

[3] Institute of Space and Astronautical Science, Sagamihara, Kanagawa 229, Japan

1 Introduction

The Infrared Telescope in Space (IRTS) is a cooled telescope that is scheduled to be launched on the first Space Flyer Unit mission (SFU-1) from Tanegashima Space Center in early 1995. The SFU is a multipurpose satellite on which many experiments are loaded, and will be placed into a nearly circular, 482 Km altitude, 28.5° inclination orbit (Natori & Kuriki 1991). During about 3 weeks of observing, the SFU mission will be dedicated to IRTS observations. After a period of 6-18 months from launch, the SFU-1 is scheduled to be retrieved by NASA's Space Transportation System for refurbishment and reuse in the future.

The IRTS will orbit the earth with the telescope sweeping across the sky at a rate of 4′/sec in great circles (Murakami et al. 1993). The axis of the great circle will be fundamentally pointed to the sun and precessed at a rate of approximately 4′/orbit. Approximately 10% of the sky will be observed in the anticipated 3 weeks mission.

The IRTS telescope is of Ritchey-Chrétien design with gold- coated aluminum optics (Onaka et al. 1993). The system of baffles employs a combination of sunshade, passively cooled aperture shade, cryogenically cooled specular forebaffle, and black aftbaffle (Sato et al. 1993). The telescope size of the IRTS is small (15 cm diameter), but the IRTS is optimized to observe diffuse extended infrared sources. Four scientific instruments and a star sensor (germanium photovoltaic detector) share a common focal plane in the IRTS telescope. This paper describes one of the instruments, the Near-Infrared Spectrometer (NIRS). Descriptions of the other three instruments (Mid-Infrared Spectrometer (MIRS), Far-Infrared Line Mapper (FILM), and Far-Infrared Photometer (FIRP)), and the telescope facility can be found in other reference (Roellig et al. 1993; Shibai et al. 1993; Lange et al. 1993; Murakami et al. 1993; Onaka et al. 1993; and Sato et al. 1993).

The NIRS is a simple grating spectrometer covering wavelength from 1.4μm to 4.0μm, with a resolution of 0.12μm. The field of view is $8' \times 8'$. The NIRS was designed to measure the absolute sky brightness with coarse spectral resolution. The origin of the light of the night sky has been one of the interesting subjects of astrophysics. The diffuse near-infrared background mainly consists of zodiacal light, thermal emission from interplanetary dust, starlight, and extragalactic background light (EBL). The spectral information obtained by the NIRS is useful to separate them into each component. The NIRS was optimized for diffuse sources, but can also observe bright point sources because the field of view is relatively small.

The NIRS observations are fairly unique as compared with other previous and future observations. The Infrared Astronomical Satellite (IRAS; Neugebauer et al. 1984) showed the great advantage of the orbiting cooled infrared telescope and contributed to revealing the general infrared view of the universe. There were, however, only four photometers centered at 12, 25, 60, and 100μm, and a low

spectral resolution spectrometer operating from 8 to 23μm.

The Diffuse Infrared Background Experiment (DIRBE) on the Cosmic Background Explorer (COBE) satellite, which was launched in 1989, was designed to conduct a sensitive search for an isotropic cosmic infrared background (Hauser et al. 1991). It observed the entire sky with a $0.°7 \times 0.°7$ field of view in 10 different bands from 1.2 to 240 μm, including the standard J, K, L, and M bands (Hauser 1993). It also observed the polarization of the sky at J, K, and L bands (Berriman et al. 1993). Compared with DIRBE, the NIRS is characterized by spectral observations with smaller beam size.

The Infrared Space Observatory (ISO), which will be launched in 1995, plans to measure the extragalactic background from the near-infrared to the far-infrared by photometry or imaging in selected areas. ISO has a coarse resolution grating spectrometer from 2.5 μm to 12μm (ISOPHOT-S), but the sensitivity for diffuse sources is worse than that of the NIRS. A non-biased survey with high sensitive spectrometry characterizes the NIRS in comparison with ISO.

2 Astrophyscial Objects

2.1 Zodiacal Light

The zodiacal light, which is sunlight scattered by interplanetary dust (IPD), has been studied in the ultra-violet and the optical band. An all-sky map of the zodiacal light at the V band (0.50μm) was summarized by Levasseur-Regourd & Dumont (1980). The color of the zodiacal light has been found to be close to the solar color (Leinert 1975). Based on these observations, various models for the volume scattering function and space distribution of the IPD have been proposed (Lamy & Perrin 1986). In the near- infrared region, there have been few observations of the zodiacal light. If the size of the dust grains is comparable to the wavelength of visible light, the color of the zodiacal light in the near-infrared would have to be bluer than the solar color. Matsumoto, Akiba, & Murakami (1988, hereafter MAM) reported that the color of the zodiacal light is bluer than the solar spectrum, but a recent rocket observation (Noda et al. 1992) indicates that near-infrared color of the zodiacal light is close to the solar color. Information of the near-infrared spectrum with wide sky coverage will reveal the size and spatial distribution of the dust.

At longer wavelengths, IRAS observed the thermal emission of the IPD with almost complete sky coverage (Hauser et al. 1984). From IRAS observations, the temperature of the IPD was estimated to be 275 ± 57K (gray body) at the ecliptic pole and 244 ± 44K (gray body) at the ecliptic plane, but MAM suggested that the temperature of the IPD is about 205K (gray body). The DIRBE on the COBE has obtained photometric maps of the full sky from 1.2 to 240μm (Hauser 1993). Detailed analysis will add new information about IPD. The NIRS on the IRTS, together with the MIRS (from 4.5μm to 11.7μm), will give us an almost

continuous spectrum of the Wien part of the thermal emission of the IPD. The spectrum data will be important to estimate the temperature of the IPD and investigate the composition of the interplanetary dust particles.

2.2 Diffuse Galactic Light

The main component of starlight in the near-infrared is emission from faint late type stars. A near-infrared balloon-borne survey of the Galactic plane clearly revealed the stellar distribution (Hayakawa et al. 1981), but was performed only for the Galactic plane with a few infrared wavelength bands, which do not suffer strong atmospheric emission. The spectral coverage and resolution of the NIRS will allow observation of molecular bands (ex. CO at 4.6μm, H_2O at 2.7μm) from late type stars. Observations of stars at high galactic latitude are important in studying the nature of the galactic halo stars.

Unidentified infrared bands (3.3, 3.4, 6.2, 7.7, 8.6, 11.3μm etc.) have been observed in planetary nebulae (Gillet, Forrest, & Merrill 1973; Russell, Soifer, & Willner 1977). The origin of these IR emission features is suggested to be polycyclic aromatic hydrocarbons (PAHs) heated by absorption of single UV photons of the interstellar radiation field (Léger & Puget 1984). A 3.3μm feature in the diffuse emission of the galactic disk was reported by Giard et al. (1988). The NIRS and the MIRS will be able to observe these spectral features in various sites: circumstellar clouds, star forming regions, and general interstellar clouds. Not only the intensities of these band emissions but also correlation with the [CII] line emission and the far-infrared dust emissions observed by the FILM and the FIRP will give us information about the composition of the interstellar dust and the physical conditions of the interstellar radiation field.

2.3 Extragalactic Background Light

Although it has not been observed unambiguously so far, an infrared extragalactic background has been postulated to exist in cosmological theories (Partridge & Peebles 1967). The infrared EBL is the integration of redshifted light from galaxies or Population III stars, which would have emitted a huge amount of UV and optical radiation (Carr, Bond, & Arnett 1984; McDowell 1986). A spectral window exists in foreground emission in the vicinity of 3μm (cf. Figure 8), in which the infrared EBL may be observable.

Since the 1970s, searches for the EBL have been tried in the optical and near-infrared region, but have produced only upper limits because of strong foreground emissions or thermal emission from the instruments (Hofmann & Lemke 1978; Mattila 1990). Recently, the brightness of the EBL has been derived from galaxy counts (Tyson 1990; Cowie et al. 1990). Near-infrared observations using sounding rockets with cooled optics have attempted to measure the EBL (MAM; Noda et al. 1992). These rocket observations suggested unknown isotropic emission

$\sim 10^{-11}$W cm^{-2} sr^{-1} in the K band, which would be attributed to an extragalactic origin. The DIRBE result shows the almost same absolute sky brightness with the rocket observations, but the shape of the energy distribution is reported to be different and some doubt about the rocket measurements is indicated (Hauser et al. 1991). In order to discriminate the EBL from the observed sky brightness, careful analysis and modeling about the DIRBE data will be expected. The NIRS spectral observation which covers the "window" in the near-infrared will give us more reliable information about the EBL.

2.4 Point Sources

Because of its moderate spatial resolution and high sensitivity the NIRS will be able to separate stars brighter than 7th K-magnitude from the diffuse background and measure their near-infrared spectrum. Combining the NIRS data with the data from the MIRS will produce continuum spectra from 1.4μm to 11.7μm, the wavelength region containing H_2O, H_2O ice, CO, Si, and SiC bands. The NIRS and MIRS observations will measure spectra of sources at shorter wavelength and one or two orders of magnitude fainter than the low resolution spectrometer of IRAS. These data will be valuable for studying evolution and physical process of late type stars.

3 Instrument

The NIRS is a grating spectrometer with two 12 element InSb (indium antimonide) linear arrays. In order to achieve a good S/N ratio, we have developed a sensitive and low noise detection system, with an InSb detector array and a charge integrating amplifier. Given the performance of the detector system, we fixed the field of view to be $8' \times 8'$ and the spectral resolution to be $\Delta\lambda = 0.12\mu$m. The characteristics of the NIRS are summarized in Table 1.

3.1 Spectrometer

The schematic view of the optical system of the NIRS is shown in Figure 1. The 1.4mm×1.4mm slit is located at the IRTS telescope focal plane. The cylindrical mirrors (CM1 and CM2) change the $F/4$ beam to $F/8$ along the Z-axis only. A large F number makes the spectrometer compact with small aberrations. The beam is made parallel by the parabolic mirror (PM) and is diffracted by the grating. It is focused again on the detector by the spherical mirror (SM). The two 12 element InSb linear arrays are aligned in the focal sphere, and each of them has an order- sorting band pass filter. The wavelength range of the shorter wavelength array is from 1.43μm to 2.54μm and that of longer wavelength side is from 2.88μm to 3.98μm. A channel number is assigned to each detector element in order of increasing wavelength.

Table 1: Characteristics of the NIRS

Size (mm^3)	135 × 154 × 102 overall
Weight(kg)	1.18
Entrance Sperture (mm^2)	1.4 × 1.4
Field of View ($arcmin.^2$)	8 × 8
Temperature (K)	~1.8
Detection System	2 × 12 ch. linear arrays with low resolution grating spectrometer
Detector	InSb
Element Size (mm^2)	1 × 0.5 (per element)
Number of Elements	24 (2 × 12 elements)
Wavelength Coverage (μm)	1.43 - 2.54, 2.88-3.98 (0.1 μm interval)
Resolution (μm)	0.12 (0.10 at channel 1)
Dark Current (A)	several $\times 10^{-17}$
Total Capacitance (pF)	~50
Readout Method	charge integration amplifier
Temperature of J-FETs (K)	~70

The grating of the NIRS, made by Hitachi Corp. has a ruling number of 93 lines/mm, blaze angle of 4.°8, and blaze wavelength of 1.80μm. The aluminum mirrors were machined and polished by Nikon Corp. Their surface is coated with Au and SiO_2, and has a measured reflectivity of more than 96% from 1μm to 5μm.

In order to calibrate D.C. drifts of the electronics and to measure the zero signal level, a cold shutter is located at the entrance slit and is closed for 8*s* every 66*s* automatically. A small wolfram lamp is installed near the shutter for an internal calibrator, which turns on for 8*s* every 17.5 minutes to monitor the stability and linearity of the instrumental response.

3.2 Detection System

Each channel of the detection system consists of an InSb photodiode and a charge integrating amplifier. The InSb array detector was developed under a collaboration with Hamamatsu Photonics K.K. (Murakami et al. 1987; Yamamoto et al. 1989). Important features of this detector are its low capacitance and very low dark current at low temperature. Since a large capacitance increases the voltage noise of amplifier, the low capacitance of the detector reduces the system noise. For the flight detector module, the element size is 1mm by 0.5 mm and the total capacitance, including stray capacitance, is about 50 pF. The typical dark current at 2K is several times 10^{-17} A.

The charge integrating amplifier, consists of an InSb photodiode and three

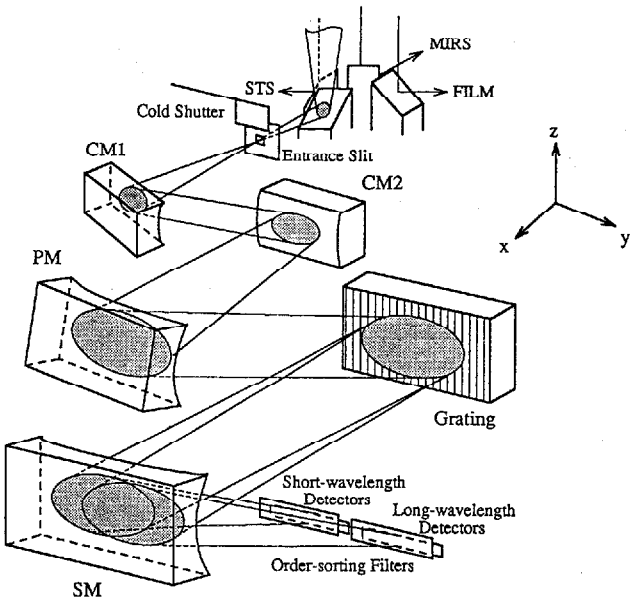

Figure 1: The schematic view of the optical system of the near-infrared spectrometer.

FETs, shows better noise performance than the usual TIA at longer integration time (Murakami et al. 1988; Yamamoto et al. 1989; Noda 1991). Figure 2 shows a portion of the circuit diagram of the 24 channel array. Charges generated by incident photons are integrated in the electric capacitance of the photodiode and are read out nondestructively without transfer. The integrated charges are periodically discharged every 66s through a reset FET. The detectors are not explicitly biased in this system. They are automatically biased to about a hundred millivolts by a charge injection following a charge reset. The well capacity is typically 3×10^7 electrons. The dynamic range required for the NIRS observation is about 10% of the total capacity, that guarantees a good linearity. The corresponding values of noise equivalent power are 2×10^{-17} W at 1s integration, and $< 3 \times 10^{-18}$ W for

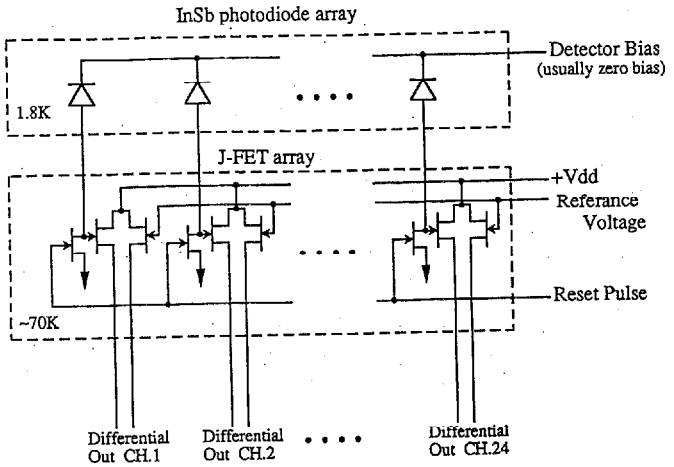

Figure 2: A portion of the circuit diagram of the 24 channel array.

longer than 10s integration. The linearly improvement of S/N ratio with integration time is the important feature of the charge integrating amplifier.

The operating temperature of the InSb detectors is 1.8K, but the J-FETs do not work well below 50K. Thus, the J-FETs have to be thermally isolated from the cryogenic work surface and their temperature must be controlled to about 70K. Twenty-four discrete sets of amplifiers are mounted on a thin sapphire substrate, which has both good electrical isolation and high thermal conductivity at low temperature. On the substrate, a metal film resistor and a platinum chip resistor are also installed and a bridge circuit was used to control the resistance of platinum to remain constant. This circuit can control temperatures around 70K with 50mK stability, and the settling time from turn on is about 5 minutes.

The sapphire substrate is suspended from the frame by bundles of aramid fibers, and 10μm stainless wires are used for signal lines from the sapphire substrate to the frame. This design has low thermal conductivity and is strong enough to survive the vibrations at the launch of the satellite. A few mW is necessary to keep the temperature of J-FETs around 70K, given the thermal conductivity of the aramid fibers.

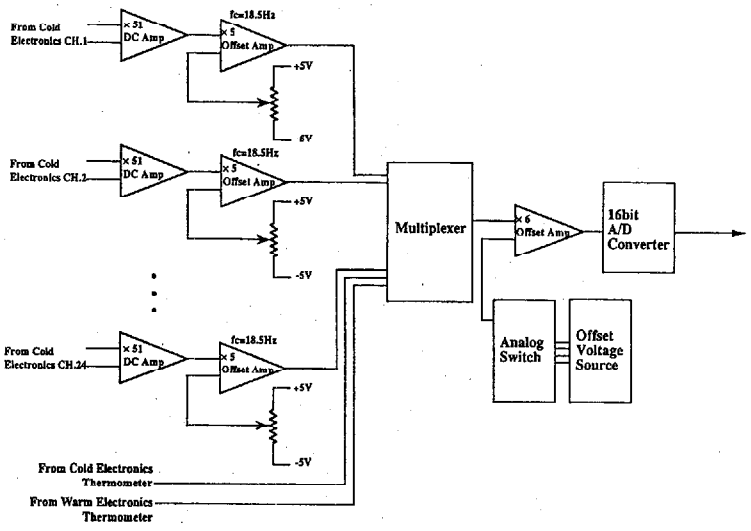

Figure 3: The block diagram of the NIRS warm electronics.

3.3 Warm Electronics and Telemetry Data

A block diagram of the warm electronics, constructed by Hamamatsu Photonics K.K., is shown in Figure 3. The output signals from the cold electronics are coupled to discrete low-noise differential amplifiers. Since the mismatch of the dual J-FETs results in scattered output signals, individual offset amplifiers are used after the pre-amplifiers in order to cancel this scatter. The total gain of the warm electronics is 1600 and the sampling frequency for each detector is 4Hz.

Data from all four of the focal plane instruments, a star sensor, and telescope housekeeping are multiplexed into a 6Kbps common telemetry stream, and stored in the spacecraft's 80Mbit bubble memory. The data is telemetered to the ground during brief downlinks as the spacecraft passes over receiving stations in NASA's Deep Space Network and Japan's Kagoshima Space Center. After recording and one-site archiving, the data will be transmitted to the IRTS Sagamihara Operating Center at the Institute for Space and Astronautical Science (ISAS) for processing. The entire IRTS data set will eventually be made available to the public through the Image Processing and Analysis Center (IPAC) in the United States.

4 Calibration in the Laboratory

4.1 Individual Spectroscopy

Initially, the optical system was aligned using a He-Ne laser at room temperature. The higher orders of laser light were aligned onto the corresponding positions of the detector array. The order-sorting filters were removed during this alignment. Next, the NIRS was installed on the cold plate of a 12 inch dewar and was cooled to 4.2K by liquid helium. The spectral response was measured using calibrated monochrometer at Nagoya University. The measurements were carried out with a CaF_2 vacuum window. A cold fused quartz window at the outer radiation shield ($\sim$ 100K) which blocked long wavelength radiation was used to achieve a low thermal background condition. Since water was excluded from this fused quartz, there was no absorption bands of H_2O at 2.7μm. A CaF_2 lens, placed between monochrometer and the NIRS, made a F4 beam corresponding to the F number of the IRTS telescope. We ran air conditioners in order to keep the humidity low and purged the light path with dry N_2 gas, because some channels suffered the absorption from molecules such as H_2O and CO_2.

The measured center wavelengths for the detectors ranged from 1.43μm to 2.54μm and from 2.88μm to 3.98μm, with 0.10μm interval. Spectral resolution (FWHM) was 0.12μm except for channel 1. The short wavelength end of channel 1 was defined by an order-sorting filter, which provided a bandwidth of 0.10μm. The optical blocking properties of the spectrometer were verified below 10^{-3} for incident radiation from 1μm to 5μm, where InSb is sensitive.

4.2 Absolute Calibration Using a Large Size Blackbody

The NIRS was mounted at the focal plane of the IRTS flight telescope at the ISAS. They were installed in a special test cryostat and the absolute sensitivity to diffuse emission was measured. The absence of stray light or internal thermal background was verified by putting a cold lid in front of the telescope.

A CaF_2 vacuum window and a cold fused quartz window were also used for absolute calibration. The size of both windows was 170 mm which was large enough not to interrupt the étendue of the NIRS. Since the $\sim$ 300K emission from the laboratory was too strong for the longer wavelength channels, an aluminum plate with 1mmϕ holes on a 10mm$\times$10mm grid was placed at the inner radiation shield. It reduced the incident light by 8.6×10^{-3}. The configuration of the calibration is schematically shown in Figure 4.

A large aperture blackbody (180mm diameter)was placed in front of the test cryostat and output signals were measured for various temperatures of the blackbody. The temperature of the large aperture blackbody could be varied from 312.6K (39.4°C) to 469.6K (196.4°C). An accurate measurement of the temperature is very important because our wavelength region belongs to the Wien part

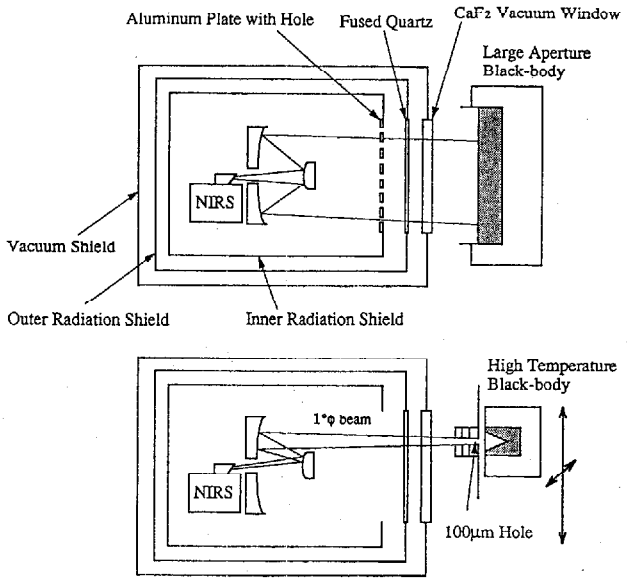

Figure 4: Schematic diagram of the absolute calibration.

of the blackbody radiation curve. The sensitivity of the NIRS taken by these measurements is shown in Figure 5. The sensitivity is defined as

$$\frac{\Delta V(T)/\Delta t}{F_\lambda(T) \cdot \lambda_c/\Delta\lambda} \quad \mathrm{V\,sec^{-1}/W\,cm^{-2}sr^{-1}}, \tag{1}$$

where λ_c is the central wavelength of the channel, $\Delta\lambda$ is the spectral resolution, $\Delta V(T)$ is increment of the output voltage for $\Delta tsec$, and $F_\lambda(T)$ is the incident flux calculated by the convolution of the blackbody spectrum at T°K and the measured spectral response of each channel. This sensitivity gives the output response of the NIRS per unit surface brightness.

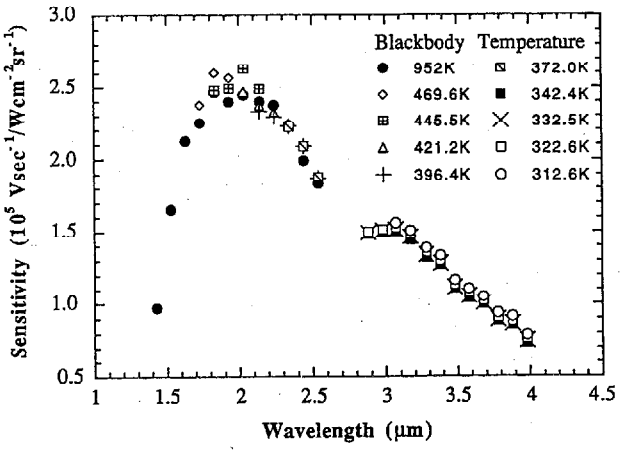

Figure 5: The sensitivity of the NIRS measured by different blackbody temperatures.

4.3 Absolute Calibration Using High Temperature Blackbody

For the short wavelength channels, the input energy from the large aperture blackbody was too small for an accurate calibration, so a high temperature calibration source was necessary. We put a small, high temperature blackbody (952K) and measured the response as the blackbody was moved over a grid with 5mm×5mm spacing. Since the aluminum plate with small holes on the inner radiation shield was removed for this measurement, the longer wavelength channels were saturated by the strong thermal background radiation from the laboratory. The middle wavelength channels could confirm the consistency of the small-blackbody measurements with the large-blackbody measurements. We used a mask with a 100μm hole and a baffle to make a 1° diameter beam which filled the solid angle of the NIRS beam. We also measured the signal of the room temperature's radiation, and corrected the incident energy from the high temperature blackbody.

The integrated value of the data after correction of the aperture size of the blackbody represents the output signal when the whole field of view of the NIRS is covered with the high temperature blackbody. The calculated sensitivity defined

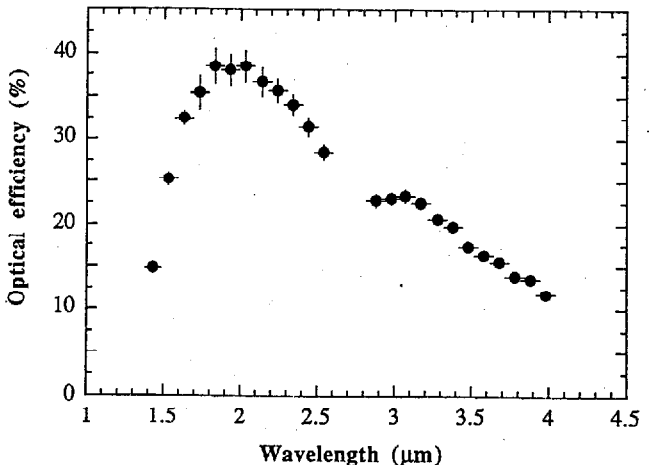

Figure 6: The optical efficiency of the NIRS.

in the previous section is shown in Figure 5 as filled circles. In spite of the extensive temperature change and the different methods, the discrepancy between the two methods is less than 5% at the overlapped wavelengths.

Based on the data from these experiments, the optical efficiency of the NIRS (including telescope) was estimated and is shown in Figure 6. For this estimate, we assumed that the field of view of the NIRS is a $8' \times 8'$ rectangular, that the effective area of the telescope is 113cm^2 (64% of the primary mirror), and that the quantum efficiency of the InSb is 0.5. The wavelength dependence of the estimated efficiency is mainly due to the characteristics of the grating. This optical efficiency was found to be as expected from the design value.

4.4 Measurement with Collimated Beam

The instrumental polarization, spectral response, and beam pattern of the NIRS were measured with a collimated beam. The test cryostat was aligned with a large (60 cm diameter) collimator mirror. A blackbody source was mounted on the X-Y stage at the focus of the collimator mirror, so that the image of the blackbody aperture was focused in the plane of the NIRS entrance slit.

When we inserted a polarizer into the beam just in front of the blackbody, a significant instrumental polarization was observed. The position angle and the

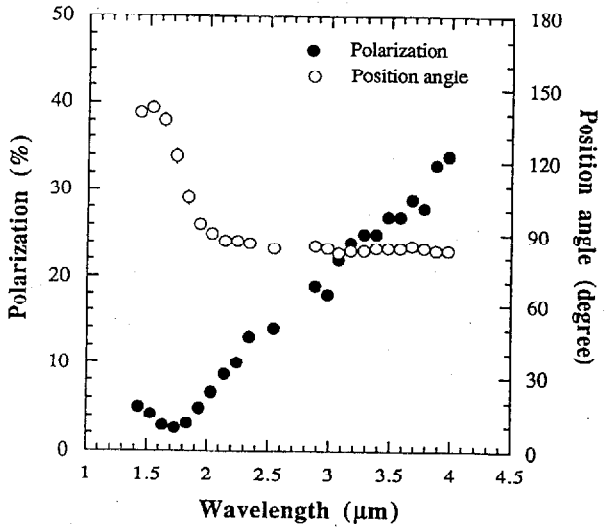

Figure 7: The measured polarization of the NIRS. Open circles represent the angle of polarization and filled circles show the magnitude of polarization.

magnitude of polarization are shown in Figure 7. The position angle is defined from the direction parallel to the ruling direction. The magnitude of polarization is smallest and the position angle changes most rapidly in the vicinity of the blaze wavelength of the grating. This is due to the characteristics of the grating. In the wavelength range shorter than the blaze wavelength, the linearly polarized light along the direction parallel to the ruling direction is stronger than that along the perpendicular to it. In the longer wavelength region, the perpendicularly polarized light is stronger, and the magnitude of the polarization increases with increasing wavelength. The measured position angles in the longer wavelength region were not 90 degrees, probably due to other polarization effects and the systematic error of the measurement of the angle. This instrumental polarization will add to the flux measurement uncertainties, because there is not *a priori* knowledge of the magnitude and direction of the polarization for the NIRS astronomical sources.

In place of the polarizer, a calibrated circular variable filter was inserted in front of the blackbody to confirm the spectral response of each detector. The result was consistent with the previous measurements using the calibrated monochrometer at Nagoya University.

Finally, we tried to measure the beam pattern of the NIRS moving the black-

body on the X-Y stage. Because of the severe time limitation of the IRTS project, the measurement was made along a few paths parallel to the axis of the stage. The result only confirms that there is no serious problem in the optics of the NIRS. We plan to measure the beam pattern of the NIRS in orbit using stars, and calibrate the sensitivity for point source by known standard stars.

5 Performance of NIRS in the Flight Cryostat

After the calibration for each focal plane instrument, optical and electromagnetic interference were measured for all scientific instruments and the star sensor using the test cryostat. The results were reflected to the construction of the electrical ground network, the optical shielding, and the timing of the calibration light for each instrument in the flight configuration.

All aligned components were carefully taken out from the test cryostat, and re-installed in the flight cryostat. Because of the release mechanism of the flight lid, a dark condition for all instruments can not be realized in the flight configuration. A cold lid was placed in front of the telescope and the absence of stray light or internal thermal background for all instruments was ascertained. After this test, we operated the IRTS system at the flight condition, and could confirm the basic performance of IRTS. NIRS showed good noise performance in the flight cryostat, and did not suffer interference from other instruments. During the tests which simulate the space environments, such as vibration and radio frequency interference, no serious problems were observed in the NIRS performance. The r.m.s. noises of all the NIRS detectors were at normal levels of about 150 electrons for several second integration time.

6 Expected Detection Limit

The sensitivity of the NIRS, according to the calibrations and the noise performance, are shown in Figure 8. Open circles indicate the 1σ sensitivity for one field of view (1 FOV) of the NIRS. Since 1 FOV of the NIRS is $8' \times 8'$ and the IRTS scans $4'$/sec overlapping one half of the 1 FOV, the sensitivity is calculated from 2 times 2 seconds integration. At high galactic latitudes, there will be some areas that the NIRS observes no bright stars for more than 10 seconds. Open squares indicate the 1σ detection limit for 10 seconds integration in such dark sky areas. Since the integrated charges are read out nondestructively at 4Hz and reset automatically every 66s, integration time can be taken until 66s. In this case, however, the space resolution becomes worse and the probability of source confusion becomes larger with increasing the integration time because of the scanning observation.

The sky brightness observed by recent rocket observation (Noda et al. 1992) and by COBE (Hauser et al. 1991) are also shown by filled circles and open

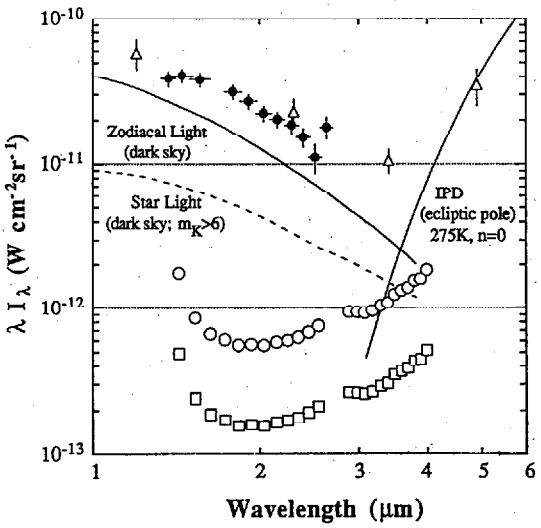

Figure 8: The detection limits of the NIRS. The total predicted sensitivity of the NIRS is shown by open circles (1 FOV 1σ) and by open squares (10sec. integration 1σ). The observed sky brightness is also shown by filled circles and open triangles. Lines represent the estimated zodiacal light, star light fainter than 6th K-magnitude at dark sky (higher ecliptic and galactic latitude), and thermal emission of the IPD at ecliptic pole.

triangles, respectively. Lines represent the estimated zodiacal light, star light fainter than 6th K-magnitude at dark sky (higher ecliptic and galactic latitude), and thermal emission of the IPD at ecliptic pole (Hauser et al. 1984). The NIRS has met its design objectives and will be able to make a highly sensitive spectral survey in the region which includes the window in the astrophysical foreground emission.

We are grateful to H. Okuda, H. Shibai, T. Onaka, and T. Watabe for help on this project and useful discussions. Thanks are also due to other members of IRTS mission, including S. Sato, H. Matsuhara, and T. Hirao. This work was supported in part by the Daiko Science Foundation and the Scientific Research Fund of the Japanese Ministry of Education, Science and Culture under Grant No.02952011.

References

Berriman, G. B., et al. 1993, COBE preprint

Carr, B. J., Bond, J. R.,& Arnett, W. D. 1984, ApJ, 277, 445

Cowie, L. L., Gardner, J. P., Lilly, S. J., & McLean, I. 1990, ApJ, 360, L1

Giard, M., et al. 1988, A&A, 201, L1

Gillett, F. C., Forrest, W. J.,& Merrill, K. W. 1973, ApJ, 183, 87

Hayakawa, S., Matsumoto, T., Murakami, H., Uyama, K., Thomas, J. A.,& Yamagami, T. 1981, A&A, 100, 116

Hauser, M. G. 1993, COBE preprint

Hauser, M. G., et al. 1984, ApJ, 278, L15

Hauser, M. G., et al. 1991, in Proc. AIP vol.222, After the First Three Minutes, ed. S.S. Holt, C.L. Bennett,& V. Trimble (AIP: New York),161

Hofmann, W., & Lemke, D., 1978, A&A, 68, 389

Lamy, P. L., & Perrin, J. M., 1986, A&A, 163, 269

Lange, A. E., Freund, M., Sato, S., Hirao, T., Matsumoto, T., & Watabe, T. 1993, ApJ, in press

Léger, A. & Puget, J. L., 1984, A&A, 137, L5

Leinert, C., 1975, Space Sci. Rev., 18, 281

Levasseur-Regourd, A. C., & Dumont, R. 1980, A&A, 84, 277

Matsumoto, T., Akiba, M., & Murakami, H. 1988, ApJ 332, 575(MAM)

Mattila, K. 1990, in IAU Symp. 139, Galactic and Extragalactic Background Radiation, ed. S. Bowyer & C. Leinert (Dordrecht: Kluwer), 257

McDowell, J. C. 1986, MNRAS, 223, 763

Murakami, H., Akiba, M., Matsumoto, T., & Noda, M. 1988, Jap. J. Appl. Phys., 27, L1973

Murakami, H., Noguchi, K., Matsumoto, T., Noda, M., Fujisada, H., Hara, K., & Sasase, T. 1987, in Infrared Astronomy with Arrays, ed. C. G. Wynn-Williams & E. E. Becklin (Univ. of Hawaii: Honolulu), 41

Murakami, H., et al. 1993, ApJ, in press

Natori, M., & Kuriki, K. 1991, Space Technol., 11, 159

Neugebauer, G., et al. 1984, ApJ, 278, L1

Noda, M., 1991, Ph.D. thesis Noda, M., Christov, V. V., Matsuhara, H., Matsumoto, T., Matsuura, S., Noguchi, K., Sato, S., & Murakami, H. 1992, ApJ, 391, 456

Onaka, T., et al. 1993, in preparation

Partridge, R. B., & Peebles, P. J. E. 1967, ApJ, 148, 377

Roellig, T. L., Onaka, T., McMahon, T. J., & Tanabe, T. 1993, ApJ, submitted

Russell, R. W., Soifer, B. T., & Willner, S. P. 1977, ApJ, 217, L149

Sato, S., et al. 1993, in preparation

Shibai, H., et al. 1993, ApJ, in press

Tyson, J. A. 1990, in IAU Symp. 139, Galactic and Extragalactic Background Radiation, ed. S. Bowyer & C. Leinert, (Dordrecht: Kluwer), 245

Yamamoto, K., Fujisada, H., Matsumoto, T., & Murakami, H. 1989, in Proc. SPIE vol.1157, Infrared Technology XV, ed. I. J. Spiro (Bellington, WA: SPIE), 338

The Mid-Infrared Spectrometer on the Infrared Telescope in Space (IRTS) Mission

Thomas L. Roellig,[1] Takashi Onaka,[2] Thomas J. McMahon,[3] and Toshihiko Tanabé [4]

Accepted for Publication in the Astrophysical Journal

Abstract

The Mid-Infrared Spectrometer (MIRS) is one of the four focal plane instruments on the Infrared Telescope in Space (IRTS) mission. The instrument has been constructed, tested, and calibrated in the laboratory and is presently scheduled to be launched by a Japanese expendable launch vehicle as part of the Space Flyer Unit-1 mission in early 1995. The wavelength coverage of the MIRS ranges from 4.5 μm to 11.7 μm, with a spectral resolution of 0.23 to 0.36 μm. With the cryogenically-cooled optics of the IRTS telescope assembly, the MIRS will be able to make an extremely sensitive survey of both point-source and extended objects over an estimated 10 % of the sky.

Subject headings: instruments - Infrared: Spectra - Artificial satellite, space probes - Interstellar: Matter

---

[1] MS 245-6, NASA Ames Research Center, Moffett Field, CA 94035-1000

[2] Department of Astronomy, School of Science (Formerly Faculty of Science), University of Tokyo, Bunkyo-ku, Tokyo 113, Japan

[3] Yerkes Observatory, P.O. Box 258, Williams Bay, WI 53191

[4] Institute of Astronomy, Faculty of Science, University of Tokyo, Mitaka, Tokyo 181, Japan

1 Introduction

The Infrared Telescope in Space (IRTS) is one of seven experiments on the first Space Flyer Unit (SFU-1), scheduled for launch from Tanegashima Space Center in Japan in early 1995. After a planned mission duration of 6-18 months, the SFU-1 will be retrieved by NASA's Space Transportation System and returned to earth for refurbishment and reuse. The IRTS telescope is cooled by superfluid Helium, lowering the infrared background seen by the instruments to the levels set by the natural Zodiacal, galactic, and cosmological emission. Four scientific instruments and a near-infrared star sensor used for telescope pointing reconstruction share a common focal plane in the IRTS telescope. This paper describes one of the instruments, the Mid-Infrared Spectrometer (MIRS). Descriptions of the other three instruments and the telescope facility can be found elsewhere (Murakami et al. 1993; Onaka et al. 1993; Bock et al. 1993; Noda et al. 1993; Shibai et al. 1993; Lange et al. 1993). A brief review of the telescope and mission parameters is given in § 2, the MIRS design and description is given in § 3, the results of the laboratory calibrations are given in § 4, and an estimate of the on-orbit sensitivity of the MIRS and its ability to meet its science goals is given in § 5.

2 The IRTS Mission

After separation from the launch booster, the SFU will be inserted into a nearly circular, 482 km altitude, 28.5° inclination orbit. After a checkout period lasting approximately one week, the IRTS aperture cover will be ejected and observations will begin from all four focal plane instruments for a period of 20 days. Upon termination of the 20 day IRTS observation period, the IRTS will be turned off and other experiments on the SFU-1 will commence. Present tests of the flight cryostat indicate that the superfluid helium hold time will be approximately 35 days, more than adequate to last through the observation period. After a period of 6-18 months from launch, the SFU-1 is scheduled to be retrieved by NASA's Space Transportation System for refurbishment and reuse in the future.

The IRTS will orbit the earth with the telescope sweeping across the sky at a rate of 0.067° sec^{-1} in great circles that are defined by the various earth and sun avoidance angle constraints (Murakami et al. 1993). Each of the great circle scans will be offset from one another by approximately 0.067°, or approximately one-half of the MIRS beam size. This means that the IRTS will survey up to approximately 1.3 steradians or 10 % of the sky during the

anticipated 20 days of IRTS observations.

3 The MIRS Instrument Description

The modest scale of the IRTS mission presented all of the focal plane instruments with severe size, weight, power dissipation, and data rate constraints. As the IRTS facility did not provide infrared calibration sources, each instrument had to incorporate its own. To meet the MIRS science goals, a low resolution spectrometer operating from 5 to 11 μm was indicated. In order to meet the power and weight constraints it was decided that the MIRS would have a fixed grating with a cold instrument entrance aperture shutter as the only moving part. Closing this shutter provides an absolute zero infrared background condition for measuring detector dark currents and also blocks the emission of stray infrared light from the MIRS when the internal calibration source is on. If this stray light were not blocked, it could produce optical interference in the other focal plane instruments during calibration periods. Since all of the IRTS focal plane instruments will be operated simultaneously, it was important that all sources of optical, electrical, thermal, and mechanical interference between the instruments be eliminated. The MIRS optical design that was developed to meet the above constraints is shown in Figure 1. The overall specifications are given in Table 1. Further details of the individual MIRS components are given below.

3.1 Optical Components

The IRTS telescope output is divided among the four focal plane instruments and the near-IR star sensor by a set of pick-off mirrors mounted just in front of the telescope focal plane. The MIRS pick-off mirror is constructed of TiN-coated polished aluminum and was manufactured by Nikon Corp. of Japan. The IRTS telescope images the sky off of this mirror onto the 1.4 mm $\times$ 1.4 mm (8' $\times$ 8 ' field-of-view) MIRS entrance aperture. A 3.4 μm long-pass filter located immediately behind the entrance aperture is used to eliminate second-order dispersed light from the grating at wavelengths shorter than 6.8 μm. As this filter also begins to gradually cut out light at wavelengths longer than 8 μm, it also limits the infrared emission that could conceivably arise from the warm JFETs within the MIRS and interfere with the longer wavelength instruments on the IRTS. The light emerging through the entrance long-pass filter then travels the length of the MIRS and strikes a concave grating which simultaneously

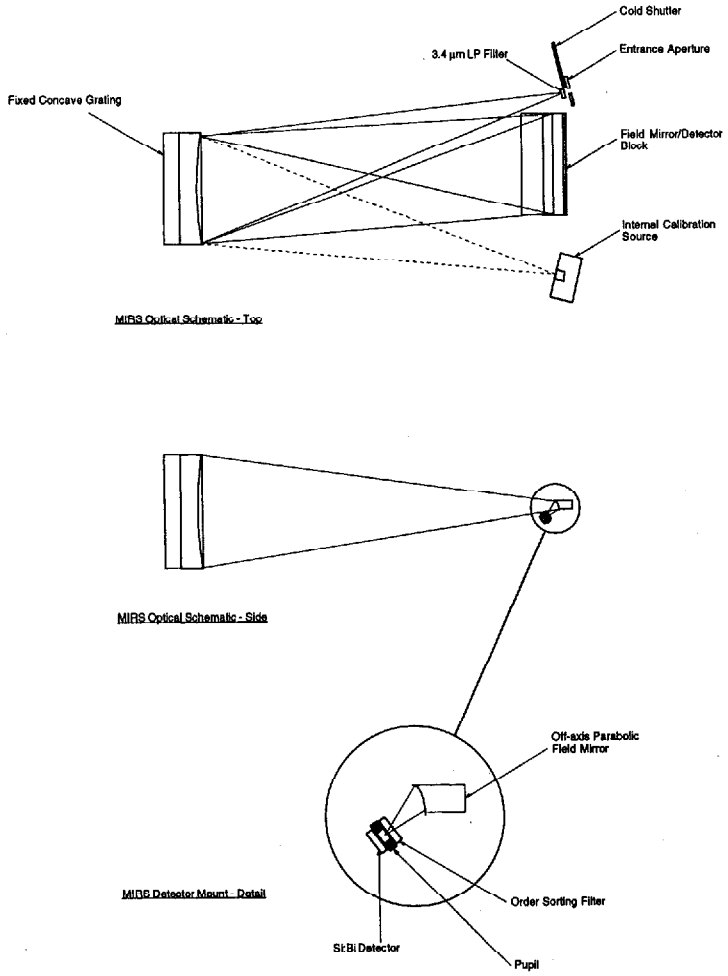

Fig.1 Schematic diagram of the optical layout of the Mid-Infrared Spectrometer.

Table 1
MIRS Specifications

Wavelength range	4.495 to 11.703 μm
Resolution	0.23 to 0.36 μm
Size	Irregular shape 210 mm × 137 mm × 75 mm overall
Weight:	805 g
Electrical power dissipation	Cold electronics - 4 mW Warm electronics - 2.9 W
Operating temperature	1.8 K
Detectors	32 Si:Bi photoconductors, (Aerojet ElectroSystems)
Entrance Aperture	1.4 mm × 1.4 mm (0.14° × 0.14° on sky)
Integrating Amplifiers	Model JF-4 (IR Labs)
Cold Multiplexers	CD4067B (RCA Electronics Corp.)
Warm electronics package	Hamamatsu Photonics K. K.
MIRS data rate	1,188 bits/sec (standard operating mode) 594 bits/sec (reduced data-rate mode)

Table 2
MIRS Grating Parameters

Grating size	50 mm × 50 mm × 17 mm
Effective area illuminated by telescope	46 mm dia.
Grating surface	Gold
Radius of curvature	160 mm
Incidence angle	14°
Blaze wavelength	6.0 μm
Nominal grating spacing	37.56/mm
Spacing variation parameters [a]:	b_2 = 0.12822 b_3 = 0.026531 b_4 = 0.0076869

[a] Definitions can be found in Harada & Kita (1980) or Onaka (1993).

refocuses the light onto the field mirror set and disperses it.

The MIRS grating is of a novel design that incorporates variable line spacings and blaze angles in order to both correct for astigmatism and flatten the focal plane (Harada & Kita 1980). With this grating design, essentially all of the aberrations can be eliminated at a given wavelength by adjusting the groove spacing parameters. In our application, we need to cover a wide range of wavelengths, so the grating parameters given in Table 2 were chosen to give the best compromise performance over the entire wavelength range (Onaka 1993). As a result, there are some un-corrected aberrations (mostly astigmatism) remaining for the wavelengths on each side of the 6 μm aberration minimum. The effect of this aberration is to broaden the base of the spectral response function for a single detector, but to leave the full-width-half-maximum (FWHM) value at the level set by the dimensions of the entrance aperture and detector. In the worst case, the increase in the wings of the response function will be 0.15 μm, which is still less than the 0.23 μm resolution imposed by the size of the MIRS entrance aperture and detector. With the MIRS grating there are essentially no aberrations in the spatial dimension, so that the spatial resolution of extended sources is not compromised. Further details of the MIRS grating construction and performance can be found in Onaka (1993).

The spectrally dispersed image of the MIRS entrance aperture is focused by this grating onto 32 off-axis parabolic field mirrors. These field mirrors in turn image the grating onto 0.85 mm diameter pupils located immediately in front of the MIRS infrared detectors. Between the field mirrors and the pupils, 6.1 μm long-pass interference filters are used for removing second-order light in the 24 longest wavelength channels. In order to keep the optical path length the same for all the channels, wide-band anti-reflection coated germanium of the same thickness as the long-pass order-sorting filters is located in front of the 8 shortest wavelength channels. The entire inside of the MIRS is highly baffled and is painted with an infrared-absorbing black paint to minimize stray light.

3.2 Detectors

The MIRS uses thirty-two individual Si:Bi photoconductor detectors to detect incoming infrared radiation. Detectors of this construction were chosen because of their relative freedom, when biased appropriately, from long-term time-constant effects in low background environments and their relative immunity to radiation-induced responsivity changes (Young 1989). Measurements taken in the laboratory indicate that the detector responsivity change is expected to be less than 5 % after a passage through the South Atlantic Anomaly. The measured performance of the MIRS flight

detectors is given in able 3

3.3 Electronics

A schematic diagram of the cold electronics is shown in Figure 2. The integrating amplifiers were obtained commercially (Infrared Laboratories, Model JF-4) and include internal heaters to prevent carrier freeze-out in their JFET transistors at liquid helium temperatures. A total heater power of 3.0 mW for all 32 units is sufficient to warm the amplifiers enough to meet the MIRS performance specifications of an output impedance of less than 50 kΩ and a voltage gain of better than 0.9. With the 1.0 mW of bias power that the integrating amplifiers dissipate when operational, a total of 4.0 mW of electrical power is generated in the cold electronics that needs to be absorbed by the superfluid helium cryogen. The other active cold electronics components, the CMOS cold multiplexers, dissipate negligible power at the low switching rates of the MIRS. Each of the amplifiers is enclosed in its own individual light-tight radiation shield, so that the warm JFETs do not introduce any extra infrared background onto the detectors. The input capacitance of the integrating amplifiers is 7.5 pF, which means that the output of the amplifiers is approximately 1.2×10^{11} V sec^{-1} amp^{-1}. Each of the two cold multiplexers consists of a 16-channel commercial CMOS-type unit (RCA Corp., CD 4067B). In order to keep the multiplexer on-state impedance low throughout the output voltage range of the

Table 3
MIRS Detector Characteristics

Detector material	Si:Bi
Supplier	Aerojet ElectroSystems
Size	$1.1 \times 1.6 \times 0.5$ mm^3
Bias voltage	2.0 V
Dark current [a]	< 1,400 $c^- s^{-1}$
Quantum efficiency [b]	6 - 70 %, 27 % average
Photoconductive gain-quantum efficiency product [a]	0.03 - 0.28
Responsivity [a]	0.1 - 2.6 A W^{-1}

[a] Measured at 2.0 V bias and 1.8 K operating temperature.
[b] Measured by vendor at 3.0 V bias, 2.8 K operating temperature, and 13.4 μm wavelength.

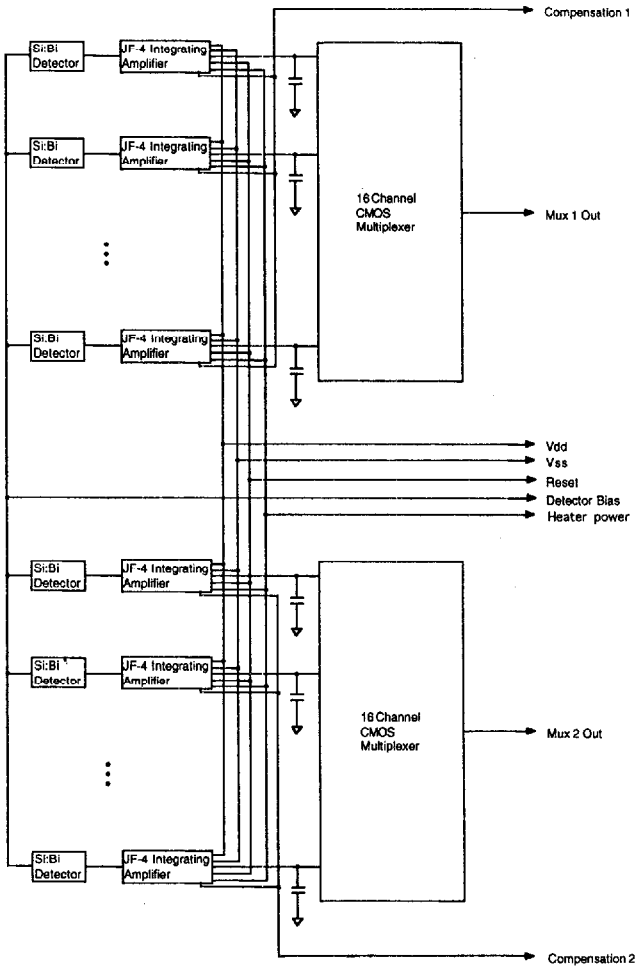

Fig.2 Schematic diagram of the 1.8 K electronics in the Mid-Infrared Spectrometer.

integrating amplifiers, the multiplexers are biased with ±5 volts and are also addressed with ±5 V logic.

The warm electronics package for the MIRS was constructed by Hamamatsu Photonics K. K. of Japan and is diagrammed schematically in Figure 3. The final output of the electronics is a serial data stream of 16 bit numbers from the detectors, thermometers, and voltage references. The total noise of the detector/electronics system with the bias voltage applied to the detector, no incident infrared flux, and sampling each detector at a 2 Hz rate, was measured to be 180 electrons read-1, referred to the detector.

During most of the IRTS mission, the integrated signal from each MIRS detector output will be sampled at a rate of 2 Hz, allowing four samples in the time it takes a point-source object to cross the MIRS entrance aperture. For approximately one third of the mission orbits, the SFU-1 spacecraft will not pass over the field-of-view of a Deep Space Network receiving station. In these orbits, the recorded data would overflow the onboard memory if the data rate from the instruments were not reduced. As a result, in the case of these orbits, the IRTS will enter a reduced data-rate operations mode where the MIRS detector outputs are sampled at a rate of 1 Hz.

3.4 In-Flight Calibration Source and Thermometry

In addition to calibrations provided by observing standard astronomical sources while scanning the sky, the MIRS will be calibrated every 15 minutes on-orbit by an internal calibration source. Each of these calibration periods will last one minute, during which all of the focal plane instruments on the IRTS will conduct their internal calibrations. The MIRS calibration source consists of a hot metal wire with a tiny drop of black epoxy acting as a black-body emitter. Tests have shown that the wire/epoxy combination heats up reproducibly to a constant emission level in approximately three seconds. The entire wire and epoxy bead assembly is located in an enclosure with a 12.5 μm diameter aperture hole, which defines a point-source and also limits the amount of far-infrared radiation from the MIRS calibration source that might interfere with the other longer-wavelength IRTS focal plane instruments. As is shown in Figure 1, the calibration source is located at the same angle relative to the grating as is the entrance aperture, but on the other side of the grating. As a result, the wavelength assignments for each detector are reversed compared to the wavelength assignments for the light from the MIRS entrance aperture. Some of the long-pass order sorting filters are therefore in the wrong positions with this scheme, so that little infrared flux is seen in the 8 longest-wavelength detectors. In spite of these

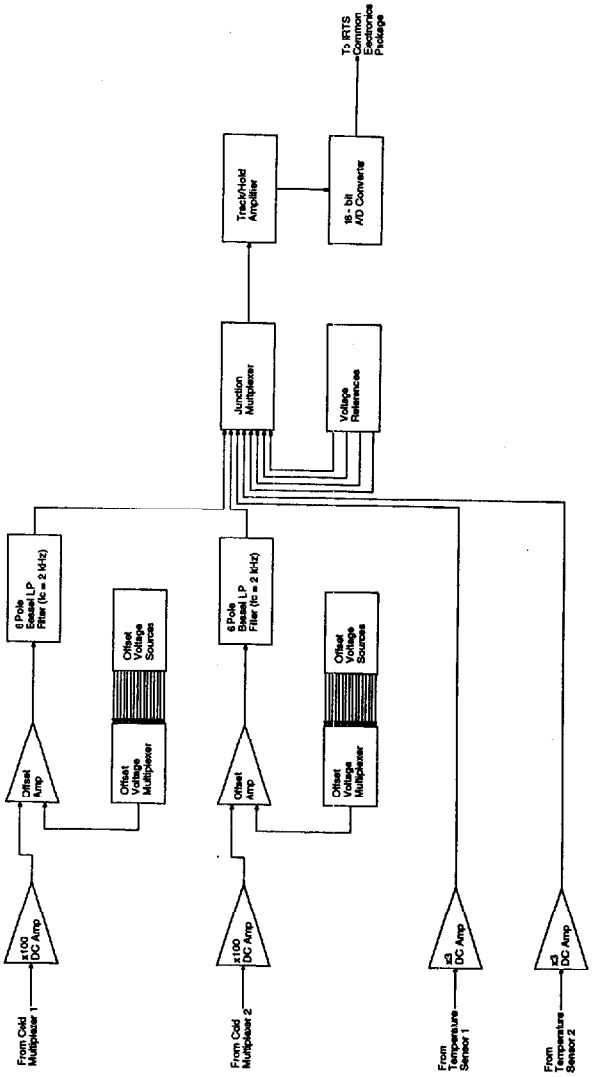

Fig.3 Schematic diagram of the warm electronics for the Mid-Infrared Spectrometer.

disadvantages, tests have shown that the calibration source will reproducibly illuminate all of the 24 shortest-wavelength detectors so that gain and detector responsivity variations can be monitored. Two Si diode thermometers (Lakeshore Cryotronics, Model DT-470) are used to monitor the temperature of the MIRS. One of the thermometers is mounted on the base of the MIRS housing, the second is mounted on the MIRS detector block holding the Si:Bi detectors.

4 Laboratory Calibrations

The MIRS was tested and calibrated extensively in the laboratory both at NASA/Ames and the Institute for Space and Astronautical Science (ISAS) prior to delivery to the spacecraft. For the initial tests and calibration the instrument was mounted at the focal plane of the IRTS flight telescope and both telescope and instrument were enclosed in a special test cryostat located at ISAS. In order to emulate the low infrared background conditions expected on-orbit, a combination of cold neutral density filters were used, reducing the infrared background seen by the MIRS/IRTS telescope in the laboratory to that of a 295 K grey body with an emissivity of $(5.6 \pm 1.5) \times 10^{-8}$. Laboratory measurements of the ND filters using an infrared spectrometer showed their spectral response to be flat to within 5 % over the wavelength range of the MIRS. Using this test cryostat, together with calibrated black body sources, the MIRS sensitivity, telescope focus, spectral range and resolution, polarization, and detector time-constant effects were measured in the laboratory. The results from these calibrations are presented in more detail below. After these calibrations were performed, the telescope assembly was installed in the IRTS flight cryostat together with the other focal plane instruments, and tests were conducted ensuring that there was no significant cross-talk or interference between any of the instruments while they were all operational.

Spectral and tests of the MIRS were made with a calibrated circular variable filter, a series of calibrated narrow band-pass filters, and two polymer plastic filters whose absorption spectrum had been previously been determined at NASA/Ames with a Fourier transform spectrometer. The full wavelength coverage of the MIRS was found to range from 4.495 to 11.703 μm, while the center wavelengths for the detectors ranged from 4.608 to 11.590 μm. The relationship between the detector center wavelength and the detector spatial position was almost exactly linear. In theory, the grating and optical parameters of the MIRS should give a spectral resolution with a FWHM of 0.23 ± 0.01 μm over the full spectral range of the MIRS (Onaka, 1993). In actuality, once corrected for the finite spectral width of the test

filters, the measured instrumental FWHM spectral resolution was found to range from a minimum of 0.23 μm at a wavelength of 6.7 μm to a maximum of 0.36 μm at 10.8 μm. The reason for the observed excess in the spectral bandwidth at the longer wavelengths is unknown at this time, although since our test set-up did not fully illuminate the grating, our measurements are only approximations to the true spectral resolution that will be achieved on-orbit. The on-orbit spectral resolution will be determined by careful comparison of observations of standard astronomical sources with known spectral lines.

The MIRS instrumental polarization was measured using a wire grid polarizer. Significant instrumental linear polarization was observed in the MIRS, with the angle of polarization coincident with the grating dispersion direction. The magnitude of the instrumental polarization is shown in Figure 4, and was found to increase with wavelength, from a value of nearly zero at the shortest wavelengths up to a value of approximately 30 % at 11.6 μm. This observed instrumental polarization is unfortunate, because although few of the MIRS astronomical sources are anticipated to be highly

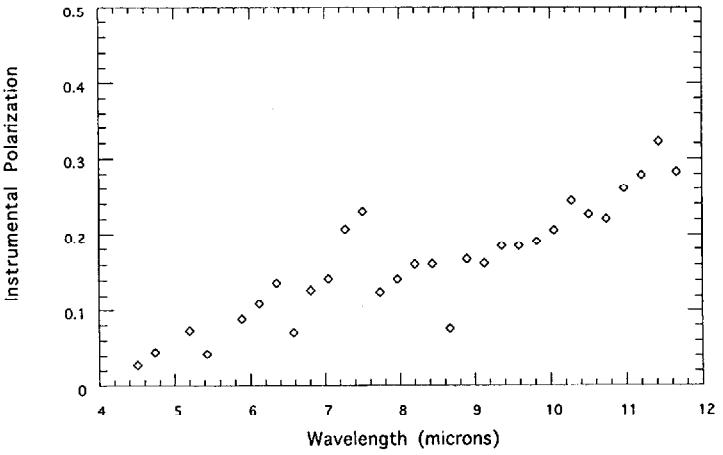

Fig.4 The instrumental polarization in the MIRS. The instrumental polarization is defined as the fraction of linearly polarized light lost in transmission through the instrument when the incident beam position angle is orthogonal to the instrumental polarization direction.

polarized in the mid-infrared, the instrumental polarization will add to the flux measurement uncertainties for those objects for which there is not *a priori* knowledge of the magnitude and direction of the source polarization.

Data were also obtained on the magnitude of long time-constant effects in the MIRS detectors. Previous experience with bulk-doped silicon photoconductors indicated that time-dependent variations in the detector responsivity are common in low infrared background environments (Beichman et al. 1988). The magnitude of such variations in the MIRS detectors was measured by applying a variable-length step function to the infrared flux received by the MIRS. Although some of the MIRS detectors exhibited responsivity changes lasting up to 4 minutes in length, the magnitude of these changes was never greater than 8 % in the worst cases. These responsivity changes were also observed to increase in magnitude with increases in the infrared flux received, so the realistic responsivity variations are expected to be less than 3 % for all except the few very brightest sources seen by the MIRS while on-orbit. Previous laboratory investigations with similar Si:Bi detectors have indicated that any on-orbit ionizing radiation-induced responsivity changes are expected to be less than 5 %.

Measurements were also taken at different MIRS operating temperatures to determine the instrument sensitivity to variations in the IRTS cryostat temperature. The instrument signal response was found to decrease by a factor of two when the temperature was reduced from 4.2 K to 2.0 K. However, the temperature response curve was fairly flat for temperatures near the expected operating temperature; the instrument responsivity changed by only 0.9 % when the temperature was increased from 1.75 K to 2.17 K.

5 The MIRS Instrumental Sensitivity

Based on the signal and noise data from these laboratory tests, the MIRS on-orbit surface-brightness sensitivity was derived and is shown in Figure 5 in a νF_ν plot. In this plot, the estimated MIRS 1-s sensitivity for one MIRS beam size is indicated by the filled black diamonds, assuming that the IRTS great circle scans are offset from one another by one half of an MIRS beam size. This estimate includes the contributions from both the measured instrumental noise as well as the estimated Zodiacal background noise. The fine line associated with the diamonds is the sensitivity limit arising from fluctuations in the Zodiacal background alone. As can be seen, the MIRS is Zodiacal background-limited in sensitivity at all but the shortest wavelengths. The derived MIRS sensitivity given above is likely to be

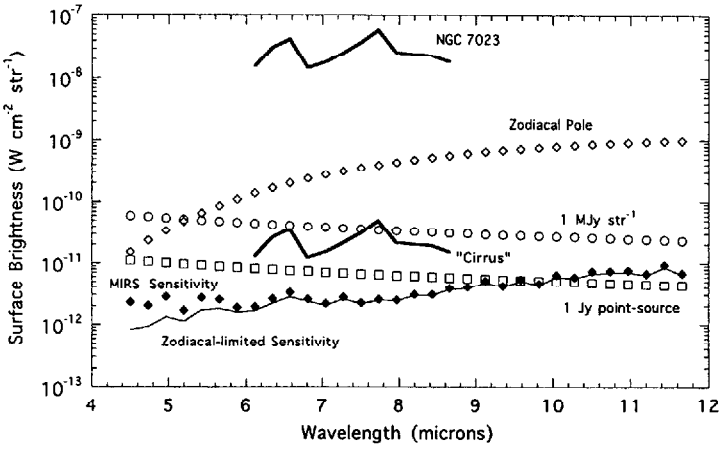

Fig.5 The sensitivity of the MIRS in a νF_ν plot, expressed as a 1 σ surface-brightness limit. The total predicted sensitivity of the MIRS is shown by the filled diamonds. The sensitivity limits imposed by fluctuations in the Zodiacal background are shown by the fine line associated with the filled diamonds. The worst-case estimate of the effects of systematic errors in the laboratory calibration are shown by the barred symbol. For comparison, the surface-brightness of various infrared sources is also indicated and are explained in more detail in the text.

affected by systematic errors from a number of sources in our laboratory measurements, including uncertainties in the transmission of the test cryostat optical train, less-than-ideal performance of the black body sources, and particularly by the fact that the MIRS grating was only being partially illuminated in our laboratory test set-up. Making our best estimates of the worst-case magnitudes for these systematic error sources, we find that the MIRS sensitivity line in Figure 5 could possibly be moved up or down by as much as the amount indicated by the barred symbol in the figure. As with the spectral resolution, the true instrumental sensitivity will have to be determined by observations of standard sources while on-orbit.

The three primary science goals of the MIRS are to: (a) take spectra of the diffuse galactic emission (cirrus), (b) take spectra of the Zodiacal light, and (c) measure the spectra of the estimated 9,800 point-sources that will fall

within the IRTS scan path and are bright enough to be seen by the MIRS. The ability of the MIRS to meet these science goals is also shown in Figure 5. In this figure, the observed spectrum of the extended reflection nebula NGC 7023 from Sellgren et al. (1985) is shown. A second spectrum of NGC 7023 is also displayed, but in this case shifted down in flux in order to match the intensity of a typical galactic infrared cirrus cloud observed by IRAS (Boulanger et al. 1985). If this shifted spectrum can be used as an estimate of what may be expected from an average cirrus cloud, it can be seen that the MIRS will have enough sensitivity to measure the spectral features at a signal to noise of over 5:1, even with the worst-case estimate of the instrument sensitivity. If the "generic" IR emission feature strength ratios from Cohen et al. (1986) are used to extrapolate the strength of the 7.7 μm feature from the measured emission from the 3.3 μm feature (Giard et al. 1989), it can be seen that the diffuse emission from the 7.7 μm feature should be detected by the MIRS to galactic latitudes greater than $|b| > 10°$.

The flux from the Zodiacal pole is shown in Figure 5 as open diamonds. It can be seen that the MIRS has the sensitivity to measure the spectrum of this emission at very high signal-to-noise. The observed flux from a hypothetical 1 Jy point-source is shown as open squares, as is the observed flux from a hypothetical 1 MJy ster^{-1} extended source, shown as open circles. The high point-source sensitivity of the MIRS will ensure that most of the IRAS 12 μm point-sources will also be bright enough for MIRS spectral studies. Confusion from more than one point-source within the MIRS beam may turn out to be the limiting factor in the ability of the MIRS to detect faint point-sources at some wavelengths. For the longest MIRS wavelengths, the IRAS data set gives an estimate of approximately 34 sources per square degree that will be seen by the MIRS at the 1 σ level in the center of the galactic plane ($|b| < 0.05°$, averaged over all galactic longitudes, Cohen et al. 1990). As the MIRS beam is only $0.14° \times 0.14°$ in size, the average number of IRAS 12 μm point-sources in the MIRS beam within the plane is 0.67. As a result, at the longer MIRS wavelengths point-source confusion is only just starting to become a problem. At the short end of the MIRS wavelength range, the situation is likely to be worse. At 4.8 μm the MIRS 1 σ point-source sensitivity is approximately 0.2 Jy or +7.2 magnitude. Estimating the density of sources at this wavelength is difficult, but an upper limit can be approximated by using the density of 2.2 μm sources from the sky model of Cohen et al. (1990). Using this model in the galactic plane ($l = 49.7°$, $b = 0.16°$) we find a number density of approximately 100 sources per square degree brighter than +7.2 magnitude at K (2.2 μm). For the MIRS beam this translates into an average of 2 sources per beam in the galactic plane. It is therefore likely that the MIRS will be confusion-limited at its shortest wavelengths within the center of the galactic plane.

6 Conclusions

A Mid-Infrared Spectrometer for the Infrared Telescope in Space mission has been constructed, tested, and calibrated in the laboratory. The MIRS has met all of the design objectives and will be able to make a very high sensitivity survey of up to 10 % of the sky, including both point-sources and extended objects. This high sensitivity will allow spectral studies of low surface-brightness extended objects, the Zodiacal dust emission, and many of the point-sources in the IRAS survey.

We are grateful for the support of this program from the NASA Astrophysics Grants Program and the Institute for Space and Astronautical Science. We also wish to thank the many people who contributed to the construction of this instrument, including N. Jennerjohn, M. Brousse, R. Zieger, and D. Lesberg. We would also like thank S. Sandford and other members of the NASA/Ames Astrophysics Laboratory for their assistance in measuring some of the MIRS filter transmission curves. Finally, we wish to thank A. Sakata, H. Okuda, T. Matsumoto, H. Shibai, H. Murakami, and M. W. Werner for useful discussions and help on this project.

References

Beichman, C.A., Neugebauer, G., Habing, H. J., Clegg, P. E., & Chester, T. J. 1988, Infrared Astronomical Satellite (IRAS), Catalogs and Atlases, Vol. 1, NASA RP-1190

Bock, J. Matsuhara, T. Matsumoto, T., Onaka, T., Sato, S. & Lange, A. E. 1993, Appl. Opt., submitted

Boulanger, F., Baud, B., & van Albada, G. D. 1985 A&A., 144, L9

Cohen, M., Allamandola, L., Tielens, A. G. G. M., Bregman, J., Simpson, J. P., Witteborn, F. C., Wooden, D., & Rank, D. 1986, ApJ, 302, 737

Cohen, M., Walker, R., Wainscoat, R., Volk, K., Walker, H., & Schwartz, D. 1990, An Infrared Sky Model Based on the IRAS Point Source Data, NASA Contractor Report 177526

Giard, M., Pajot, F., Lamarre, J. M., Serra, G., & Caux, E. 1989, A&A, 215, 92

Harada, T. & Kita, T. 1980, Appl. Optics, 19, 3987

Lange, A. E., Freund, M., Sato, S., Hirao, T., Matsumoto, T., & Watabe, T. 1993, ApJ, in press

Murakami, H. et al. 1993, ApJ, in press
Noda, M., Christov, V. V., Matsuhara, S. Noguchi, K., Sato, S., & Murakami, H. 1993, Ap.J , in press
Onaka, T. 1993, in preparation
Onaka, T. et al. 1993, Appl. Opt., in press
Sellgren, K., Allamandola, L. J., Bregman, J. D., Werner, M. W., & Wooden, D. H., 1985 ApJ, 299, 416
Shibai, H., Yui, M., Matsuhara, H., Hiromoto, N., Nakagawa, T., & Okuda, H. 1993, ApJ, in press
Young, E. 1989, Private communication

Far-Infrared Line Mapper (FILM) on IRTS

Hiroshi Shibai,[1] Masao Yui,[1,2] Hideo Matsuhara,[3]
Norihisa Hiromoto,[4] Takao Nakagawa,[1] and Haruyuki Okuda [1]

Accepted for Publication in the Astrophysical Journal

Abstract

We have developed a Far-Infrared Line Mapper (FILM) as one of the four focal plane instruments on the Infrared Telescope in Space (IRTS). The FILM is a grating spectrometer designed to simultaneously measure [C II] 158 μm and [O I] 63 μm line intensities and continuum emission near the [C II] line with spatial resolution of 8 arcmin. Very high sensitivity and accuracy are achieved by using stressed and unstressed Ge:Ga detectors at 1.8 K with a helium cooled telescope and by using a spectral scanner to distinguish the line emission from the continuum emission. Line intensities of the [C II] and the [O I] will be mapped over 10 % of the sky with much higher sensitivity than the previous survey measurements.

Subject headings: artificial satellites, space probe - instrumentation: spectrograph - methods: observational - techniques: spectroscopic -surveys - infrared: interstellar: lines

---

[1] Institute of Space and Astronautical Science, Yoshinodai 3-1-1, Sagamihara, Kanagawa 229, Japan

[2] Department of Astronomy, Faculty of Science, University of Tokyo, Yayoi 2-11-16, Bunkyo-ku, Tokyo 113, Japan

[3] Department of Astrophysics, School of Science, Nagoya University, Furo-cho, Chikusa, Nagoya 464, Japan

[4] Communications Research Laboratory (CRL), Nukui-kitamachi 4-2-1, Koganei, Tokyo 184, Japan

1 Introduction

The far-infrared wavelength region is heavily obscured by the earth's atmosphere. In order to measure astronomical far-infrared radiation, we must lift up the instruments to the stratosphere at least. The Infrared Astronomical Satellite (IRAS) has mapped the far-infrared continuum radiation with high sensitivity and high spatial resolution over the entire sky. On the other hand, spectroscopic measurements using balloons and aircraft have not been extended over wider area of the sky such as the Galactic plane.

Recently, two balloon projects, the Balloon-Borne Infrared Telescope (BIRT) and the Balloon-Borne Infrared Carbon Explorer (BICE), have succeeded in making line intensity maps of [C II] 158 μm of the Galactic plane (Shibai et al. 1991; Nakagawa et al. 1993), M17 complex (Matsuhara et al. 1992), the Galactic center (Okuda et al. 1989), and Cygnus-X region (Doi et al. 1993) with good spatial resolution and wide sky coverage. It has been demonstrated by their observational results that measurements of the [C II] line emission are important and powerful tools for investigating the interstellar gas.

On the other hand, the Cosmic Background Explorer (COBE) has provided all sky intensity maps of [C II] 158 μm and [N II] 205 μm (Wright et al. 1991). The maps reveal an entire view of the Galactic interstellar gas. However, because of its large beam size of 7 degree, the maps do not have enough spatial resolution to resolve the Galactic plane.

This paper describes the Far-Infrared Line Mapper (FILM), which has been developed to be the first satellite-borne instrument optimized to map far-infrared line intensities. It is an order of magnitude more sensitive than the balloon-borne instruments, has a better spatial resolution than the COBE, and will survey a wider sky coverage than the ISO-LWS (Infrared Space Observatory - Long Wavelength Spectrometer).

The FILM is one of the four focal plane instruments of the Infrared Telescope in Space (Murakami et al. 1993) (IRTS). The IRTS is one of the eleven experiments of the Japanese Space Flyer Unit (SFU) which will be launched in early 1995. The IRTS is a 15 cm liquid helium cooled telescope that will survey approximately 10 % of the sky during its three-week mission. Other focal plane instruments are a Near-Infrared Spectrometer (Noda et al. 1993) (NIRS), a Mid-Infrared Spectrometer (Roellig, Onaka, & McMahon 1993) (MIRS), and a Far-Infrared Photometer (Lange et al. 1993) (FIRP).

2 Scientific Goals

The FILM is aimed to investigate far-infrared line emissions of [C II] ($^2P_{3/2}$-$^2P_{1/2}$) 157.7408 μm (Cooksy, Blake, & Saykally 1986) and [O I] ($^3P_1$-$^3P_2$) 63.1837 μm (Zink et al. 1991) from extended sources described below.

2.1 Origin of the Diffuse [C II] Emission

It has been shown that, in interstellar space, the carbon atom tends to be singly ionized by ultra-violet (UV) photons coming from early-type stars (the ionization potential is 11.26 eV) and that the C^+ ion provides the most important process by the [C II] 158 μm line emission for cooling of the gas (Pottasch, Wesselius, & van Duinen 1979; Tielens & Hollenbach 1985; van Dishoeck & Black 1988).

Stacey et al. (1985) detected the extended [C II] emission from the Galactic plane. Shibai et al. (1991) confirmed the [C II] emission is extended and strong everywhere in the Galactic plane between l = 30 ° and 51 ° and that the [C II] emission probably comes from "diffuse photodissociation regions" surrounding giant molecular clouds. The derived total luminosity of the [C II] emission is 3×10^7 $L_\odot$ for the inner Galactic plane and the derived mass fraction of the C^+ region is 30 - 50 % of that of the molecular mass traced by CO (J = 1-0). These observational results have been confirmed by a recent complete [C II] survey of the Galactic plane (Nakagawa et al. 1993). Wright et al. (1991) also reported the total Galactic luminosities of 9 far-infrared lines including [C II].

The origin of the diffuse [C II] component, however, has not yet been explained. It is still unknown whether the emission originates in neutral gas clouds where the temperature is 100-300 K and the density is 100-1000 cm^{-3}, or in extended low density (ELD) HII regions where the temperature is 5000-10000 K and the density is 1-10 cm^{-3}.

Unlike carbon, the ionization potential of oxygen is approximately equal to that of hydrogen. Hence neutral oxygen does not exist in the ELD HII regions. In low-density ($\approx$ 100 cm^{-3}) photodissociation regions, the [O I] intensity is expected to be 10-100 times smaller than the [C II] intensity (Hollenbach, Takahashi, & Tielens 1991). The observed [C II] intensity at the ridge of the Galactic plane is approximately a few times 10^{-4} ergs cm^{-2} s^{-1} sr^{-1}. Therefore, the expected [O I] intensity is a few times 10^{-5} to 10^{-6} ergs cm^{-2} s^{-1} sr^{-1}. If diffuse [O I] emission associated with the diffuse [C II] emission is detected and is stronger than 10^{-5} ergs cm^{-2} s^{-1} sr^{-1}, the origin of the [C II] and [O I] line emissions can be attributed to the diffuse photodissociation regions.

The FILM is designed to survey the Galactic plane with higher sensitivity and to provide an accurate intensity maps of the [C II] and the [O I] line. We, therefore, expect that the FILM will reveal the origin of the diffuse [C II] emission.

2.2 Physical Condition of Cirrus Clouds

The IRAS discovered many infrared cirrus clouds at high Galactic latitudes (Low et al. 1984). The temperature and the optical depth of the dust in the cirrus clouds were derived from their far-infrared continuum spectra. However, since the cirrus clouds are thought to be far from a thermal equilibrium state between the gas and the dust, it is difficult to deduce the physical condition of the gas from that of the dust. Far-infrared atomic lines, such as [C II] 158 μm and [O I] 63 μm, can be good diagnostic tools to investigate the physics of the gas in the cirrus clouds.

Pottasch et al. (1979) derived, from the UV absorption line measurements, the result that the cooling rate by the [C II] line emission is 10^{-25} ergs s^{-1} per H-atom. Gry et al. (1992) have reported a smaller but more scattered value for the [C II] cooling rate from a compilation of the UV measurements. Recently, the [C II] line emission from high-latitude clouds has been measured by a rocket-borne cooled spectrophotometer system (Bock et al. 1993). From the correlation with the HI column density, a [C II] gas cooling rate of 2.3 ($\pm$ 0.3) $\times$ 10^{-26} ergs s^{-1} per H-atom was derived. Using the above cooling rates, we estimate the [C II] line intensity of (2 - 0.4)$\times$ 10^{-6} ergs cm^{-2} s^{-1} sr^{-1} for a typical cirrus cloud with an HI column density of 2 $\times$ 10^{20} cm^{-2} corresponding to $A_V = 0.1$ mag.

According to Stark (1990), the expected [O I] intensity of the typical cirrus cloud is a few times 10^{-6} ergs cm^{-2} s^{-1} sr^{-1}, which is less than the detection limit of the FILM (see section 4.6).

The FILM has a high sensitivity so that the [C II] line emission from the cirrus clouds can be detected and could provide a clue to understand the excitation mechanism and the physical condition in the cirrus clouds.

2.3 Search for Interstellar Shocks

The [O I] 63 μm emission is theoretically expected to be strong in interstellar shocked gas (Draine, Roberge, & Dalgarno 1983; Hollenbach & McKee 1989). Interstellar shock waves are driven by various phenomena including stellar winds, cloud-cloud collisions, supernova explosions, and Galactic density waves. The [O I] emissions from such shocks have been detected (Cohen et al. 1988; Burton et al. 1990). According to the observational result on IC 443, a supernova remnant, by Burton et al., the

[O I] 63 μm line intensity is expected to be (8.0 - 0.7) $\times$ 10^{-5}ergs cm^{-2} s^{-1} sr^{-1} for a FILM beam.

Draine et al. (1983) calculated the [O I] line intensity of 1×10^{-4} ergs cm^{-2} s^{-1} sr^{-1} from a C-shock wave with shock speed of 10 km s^{-1} into molecular gas with a density of 10^{2-4} cm^{-3}, a fractional ionization of 10^{-1}, and a magnetic field of 50 μG. This shock velocity is comparable with the velocity dispersion of the proper motion of the molecular clouds, and it can be expected, therefore, that such kinds of shocks generally occur in the galactic plane. Therefore the FILM can detect the [O I] 63 μm emission from weak and diffuse shock waves, if a shocked area extends over a few arcminutes.

3 Design of the FILM Hardware

3.1 Optical System

The FILM has a noble design in its optical system. It uses a "varied line-space cylindrically concave grating" which has been developed for the first time for the FILM. This grating allows us to achieve high throughput, reliability, moderately high resolution in the strict limits of small volume and light weight. All optical components as well as the grating itself are made of aluminum alloy by machining and are evaporated with gold.

Figure 1 shows the optical system of the FILM. At the focal plane of the IRTS, a small diagonal mirror is mounted for the FILM. The incident light from the telescope is reflected by 90 degrees and makes a focus on the input slit of the FILM. The slit is a rectangle of 1.4 $\times$ 3.5 mm whose elongated direction is perpendicular to the scanning direction of the IRTS. The light passes through the input slit with a F/4 divergence, is reflected by a plane mirror again, and is collimated by a cylindrical mirror in the Z-axis. The light diverging in the other direction reaches the cylindrically concave grating which has a ruling along the Z-axis.

After reflection and dispersion by the grating, the light goes back nearly along the path of the incident light and makes a focus at the front of the detector aperture. The location of the focus is shifted by 20 mm above that of the input slit in the Z-axis. The direction of the spectral dispersion at the focus is along the Y-axis. The slit width of the detector aperture is the same as that of the input slit.

Conventional concave gratings which have envelopes of a part of a sphere do not need any collimator optics. However, in order to minimize the size in the perpendicular direction of the paper, we adopted a unique idea which uses a cylindrical mirror and a cylindrically concave grating. A result of a

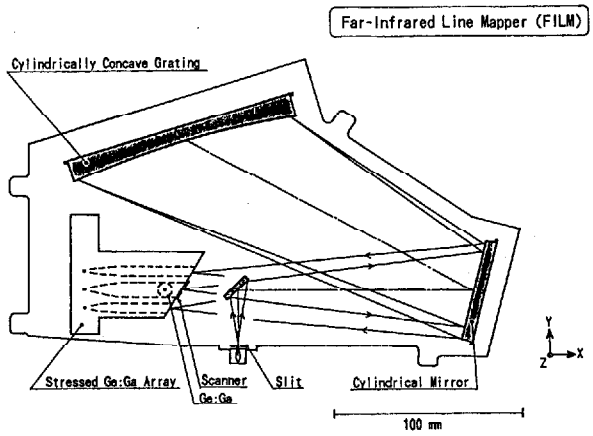

Fig.1 Schematic diagram of the FILM, viewed from behind the focal plane at the optical axis of the IRTS telescope. The converging beam to the detector mount is shifted from the diverging by 20 mm in the direction perpendicular to the sheet.

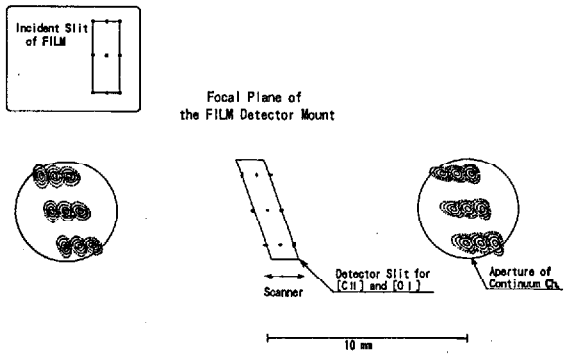

Fig.2 A ray trace of the FILM optical system. The shape of the incident rectangular slit is projected as a rhomboid at the focus in front of the detector mount. The residual aberration of the [C II] channel is very small as shown in the figure. The aberration of the continuum channels on both sides is larger but small enough compared to the FILM slit size and the diffraction limited image size.

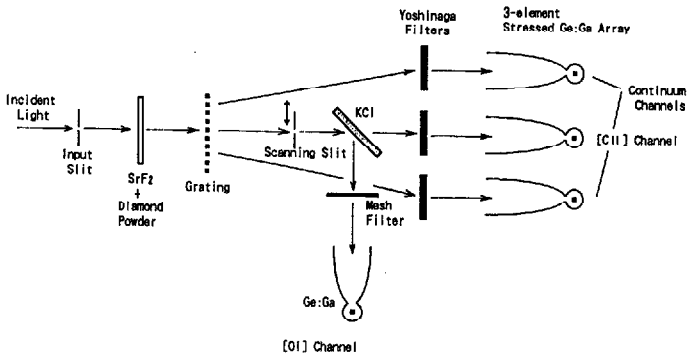

Fig.3 Schematic diagram of the filtering system.

geometrical ray trace is shown in Figure 2. The aberration for the [C II] and the [O I] channels is much smaller than the slit size, which is nearly equal to the diffraction-limited image size for 158 μm. It is noted that the image of the rectangular shape of the input slit is deformed into a rhomboid.

The pitch of the grating was controlled so that the [C II] 157.7408 μm line is exactly equal to the second order light of the spectrometer. Then the [O I] 63.1837 μm line is almost the 5th order light. The separation of the two lines at the focus is only 0.7 mm. The pitch surface of the grating is exactly a part of the cylinder but the ruling pitch is varied within $\pm$ 0.9 % in order to decrease the aberration. This grating has been made by Nikon for the FILM.

Figure 3 shows a schematic diagram of the filtering system of the FILM. A SrF_2 filter coated with diamond powder is used to block radiation at wavelength shorter than 50 μm. After the dispersion by the grating, lights of all orders near the blaze wavelengths are selected for the two line channels. Then, a KCl beam splitter reflects only fourth to sixth order light to the [O I] channel, and an interference filter passes only fifth order light. On the other hand, the light passing through the KCl beam splitter contains first to fourth and sixth orders of the light reflected by the grating. A Yoshinaga filter (Sakai, Nakagawa, & Yoshinaga 1968) passes

only first and second orders and completely blocks higher order light. Because a stressed Ge:Ga detector cannot detect the first order light (305 μm), only the second order light (158 μm) is selected. The two continuum channels have a nearly identical filtering system with the [C II] channel except that they do not have a KCl beam splitter. Figure 4 shows the spectroscopic response for each channel and it can be seen that the blocking and order selections are complete.

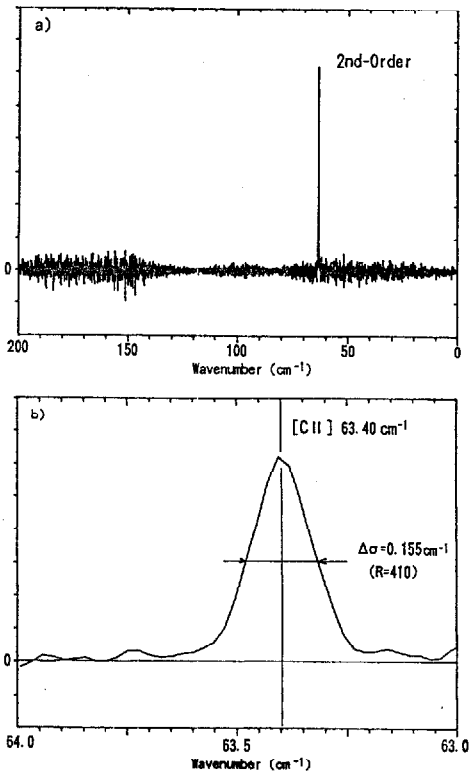

Fig.4 Results of the laboratory measurement of the spectral responses of the [C II] channel in a wide band (a) and in a narrow band near the [C II] line (b). The measurements were done by a Fourier transform spectrometer.

3.2 Detectors

Detectors used in the FILM have been developed by a collaboration between ISAS and CRL (Hiromoto et al. 1992). A linear three element array of Ge:Ga photoconductor with a stress assembly is used for the [C II] 158 μm and the two continuum channels. On the other hand, a single element unstressed Ge:Ga photoconductor is used for the [O I] 63 μm channel. The two line channels have a common slit which is scanned in the direction of the spectral dispersion at 2 Hz by a spectral scanner. This mechanism allows us to extract the line intensity components from the total signals.

The light passing through the slit is divided into two spectral channels by a KCl beam splitter. Each beam is collected by a Winston cone collector into a detector cavity.

In order to stabilize the detector responsivities and suppress non-linear responses, weak and constant light sources ("bias lights") are incorporated to the detector assembly. The lights are introduced from the sources through thin stainless steel pipes into the detector cavities. They can be continuously turned on during observations in order to reduce the dependence of the responsivity on the total incident flux. When this light is on, the responsivity change caused by the total flux change should decrease, but the photon noise would slightly increase under a lower total flux condition described below.

It has been pointed out that performance of detectors is also affected by cosmic high energy particles (Oda, Lemke, & Wolf 1984). During the IRAS mission, cosmic rays hit on each detector at the rate of about one per twenty seconds (IRAS Explanatory Supplement 1985). Because the volume of the detector element (0.125 mm^3) is less than one-tenth of that of the IRAS (2 mm^3) and because the orbital altitude is 482 km while the IRAS into 900 km, the rate of cosmic rays' hits will be much smaller than that of the IRAS. Except for passage through the South Atlantic Anomaly (SAA), the hit rate is estimated to be about one event in ten minutes. For annealing the radiation effect after passing through the SAA, the detector bias voltage can be increased above the breakdown voltage ("bias boosting").

3.3 On-board Electronics

The first stage of each sensor channel is a conventional transimpedence amplifier (TIA). Four JFETs (Infrared Laboratories, Inc.) are mounted near the detectors. The TIA method has an advantage of a wide dynamic range, which covers both the bright Galactic plane and faint cirrus clouds.

After passing a low-pass-filter, the signal voltage is converted by a

square-root amplifier, by which the dynamic range can be increased significantly in the photon noise limited condition without any degradation of the signal to noise ratio. The resultant dynamic range can be about 108 with a 16 bit A/D converter without any electronics for changing gains.

The detector bias voltages are changeable in order to optimize operating conditions of the detectors and apply high voltages to them for quick recovery after the passage of cosmic particles through the detector.

4 Laboratory Tests

We have measured the performance of the FILM, and have confirmed that it has excellent performance as designed. For almost all the tests, the FILM was mounted on the focal plane of the IRTS flight telescope. Part of the spectroscopic performance of the FILM was measured before being mounted on the telescope. The results of these measurements are summarized in Table 1.

Table 1
FILM Summary

Size	:	250 × 150× 130(H) mm			
Weight	:	1950 g			
Grating	:	a varied line-space cylindrically concave grating			
Beam size (FWHM)	:	8 arcmin (dispersion direction) × 13 arcmin			
Area to be observed	:	10 - 20 % of the sky			
Channel	:	Ch.1	Ch.2	Ch.3	Ch.4
Band Center (cm^{-1})	:	64.4	63.4[a]	62.4	158.4[b]
Resolving Power	:	130	409	130	405
Detectors	:	(linear 3-el. stressed Ge:Ga array)			Ge:Ga
Optical through-put[c]	:	0.34	0.30	0.34	0.15
S(detector) (A/W)[d]	:	10.1	11.1	9.7	0.51
System NEP (10^{-16} W $Hz^{-1/2}$)	:	1.8	0.60	1.7	12

[a] scanning range is 63.2-63.6 cm^{-1}
[b] scanning range is 157.9 - 158.9 cm^{-1}
[c] calculated efficiency of the FILM optics including filters
[d] including all unknown loss

4.1 Responsivity

For a DC responsivity measurement of the FILM detector, we used a neutrally attenuated blackbody source attached in front of the telescope aperture. It is a copper disk coated with special black paint (Bock & Lange 1993) and has a thermometer, a heater for temperature control, and a mask with grid-patterned holes for suitable attenuation.

In the source temperature range between 20 K and 70 K, the measured responsivities of the FILM detectors were constant within 10 %. The results are shown in Table 1. The values of the responsivity listed in the table include all unknown losses; known losses are included in the optical throughput. Comparing this responsivity with those measured prior to the installation on the telescope, there remain discrepancies of a factor of two at most. These discrepancies have not been resolved. As for the absolute responsivity, observations of astronomical objects whose fluxes have been measured previously will provide a good calibration.

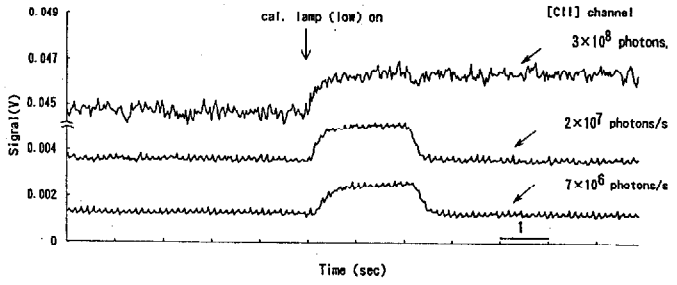

Fig.5 The signal output (the [C II] channel) of one of the calibration lamps under three different backgrounds. The lowest DC level was achieved by making the shutter closed, the middle and highest level by turning each of the bias lamps on. In case of the lowest and middle level, the calibration lamp was activated for two seconds. The spectral scanning was not active.

Since the detectors of the FILM are photoconductors, there may be responsivity changes due to changes of the total incident flux and the temperature, and a transient response caused by a stepwise change of the incident flux. First, the change of the responsivity due to the temperature change was less than 5 % between 1.75 K and 2.0 K; the expected detector temperature in orbit is 1.8 K - 1.9 K. Second, measured DC responsivities were constant within 10 % under the total incident flux $< 10^9$ photons per second, which corresponds to the sky brightness of < 100 GJy sr^{-1}. Third, as shown by Hiromoto et al. (1992), the AC responsivities of the detectors (Channels 1, 2 and 3) depend on the total incident flux. It was found that the change of signal voltage after the calibration lamps turn on depends on incident radiation flux. Figure 5 shows examples of the slower and non-linear responses for a signal change under various conditions of the total incident flux.

The FILM has two calibration lamps in order to correct any changes of the responsivities during the observation, including the effect caused by background radiation. The calibration light generates a rectangular pulse of 2 seconds every 64 seconds. Since the rectangular signal includes higher frequency components, the measured calibration signal is affected by the AC responsivity change due to the total flux change described above. However, it was found that, using laboratory measurements, this effect can be corrected with a residual error of 10 %.

4.2 Noise

Measured noise voltages of all channels are nearly proportional to a square root of the detector current when the photon flux is high (1 GJy sr^{-1}), and otherwise are nearly constant. The continuum brightness of 1 GJy sr^{-1} corresponds to that of the bright ridge of the Galactic plane. In a dark condition, the measured noise is a few times larger than the expected thermal noise of the feedback resister. This enhancement is caused by electrical interferences and by a photon noise of an unidentified light source in the FILM. The surface brightness at high Galactic latitudes is on the order of 10 MJy sr^{-1}. Therefore, the noise and the resultant system noise-equivalent-power (NEP), shown in Table 1, will be nearly constant except near the Galactic plane.

4.3 Spectral Characteristics

Spectral characteristics of the FILM have been measured using a Fourier transform spectrometer before the installation on the IRTS flight telescope. The spectral resolution and the central wavenumber of each detector channel

are shown in Table 1, which are just as designed. As shown in Figure 4, we can see no diffuse spectral component, which would be mainly caused by the stray light in the spectrometer system. The diffuse spectral component obtained is less than 10^{-3} of the 2nd order light, and therefore its effect should be quite small.

The performance of spectral scan of the [C II] channel (Channel 2) was measured. At the measurement, the FILM was mounted on the IRTS telescope, and a parallel beam from a spectral line source whose wavelength is equal to the [C II] line was introduced into the IRTS. The scan worked correctly as designed. As for the spectral scan of the [O I] channel (Channel 4), it is also expected to work properly, because the aperture slit is common for Channels 2 and 4.

4.4 Instrumental Polarization

Because the FILM is a grating spectrometer, a certain degree of instrumental polarization was expected. The instrumental polarization was measured for Channels 1 and 2 by using a polarized source. Both channels have instrumental polarization of 25 % along the direction parallel to the ruling of the grating. However, because the [C II] 158 μm and the [O I] 63 μm lines are predominantly emitted by spontaneous transitions from collisionally excited states, it can be assumed that the line emissions have no polarization.

On the other hands, the continuum emission may have a small polarization, of the order of 1 %. Therefore, the instrumental polarization will introduce an error of less than 1 % into the continuum channels.

4.5 Beam Size

The beam pattern of the FILM mounted on the IRTS was measured for Channels 1, 2, and 4. The beam pattern is nearly elliptical and the FWHM is 8 arcmin along the dispersion direction and 13 arcmin along the scanning direction. Observations of point-like sources in orbit will provide another accurate measurement of the beam pattern.

4.6 Sensitivity and Comparison with Other Instruments

On the basis of those measurements described above, we have calculated the detection limits for the two spectral lines under low background radiation. The results are shown in Figures 6 and 7. In these figures, the intensities from typical astronomical objects and the detection limits of

other instruments are also shown.

The three sigma detection limit of the [C II] channel is 1×10^{-6} ergs cm^{-2} s^{-1} sr^{-1}, which is one to two orders of magnitude better than those of the airborne and balloon-borne telescopes. The diffuse [C II] emission from the Galactic plane, which is one of main observational targets, will be detected with a high signal to noise ratio ($\simeq$ 100). Moreover, the FILM is expected to detect a weak [C II] emission from regions outside the Galactic plane.

The FIRAS on the COBE has measured the extended [C II] emission (Wright et al. 1991), but the beam size of 7 degrees is too large to distinguish the individual Galactic components from the general Galactic plane component in the [C II] intensity map of the whole sky. By contrast, it is expected that the FILM can resolve those components with its smaller beam size of 8×13 arcminutes.

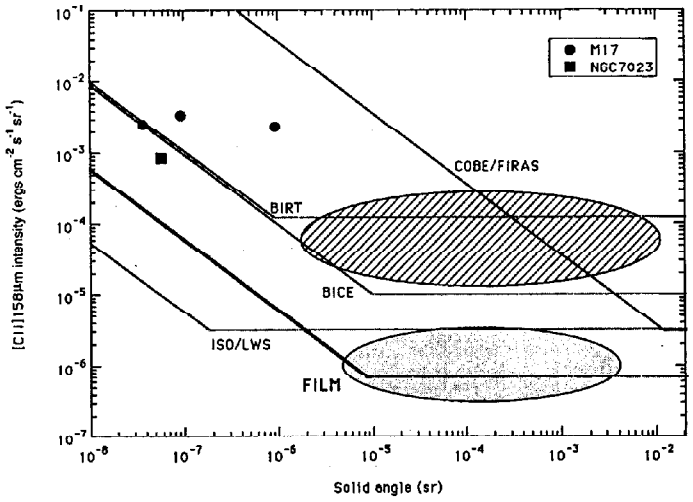

Fig.6 The sensitivity of the [C II] channel of the FILM (3σ, 1 FOV), compared with those of BICE (3σ, 1 FOV) (Nakagawa et al. 1993), BIRT (3σ, 1 FOV) (Shibai et al. 1991), FIRAS on COBE, and LWS on ISO (3σ, integration time is 1 second) (Scientific Capabilities of the ISO Payload 1991). The detection limit of the FIRAS is an approximate estimate using the all-sky [C II] 158 μm map of Wright et al. (1991). The limit of the ISO/LWS is inversely proportional to the square root of the integration time. The observed or estimated intensities of some astronomical sources are also shown. Hatched region: diffuse [C II] emission from the Galactic plane (see 2.1). Shaded region: cirrus clouds (see 2.2).

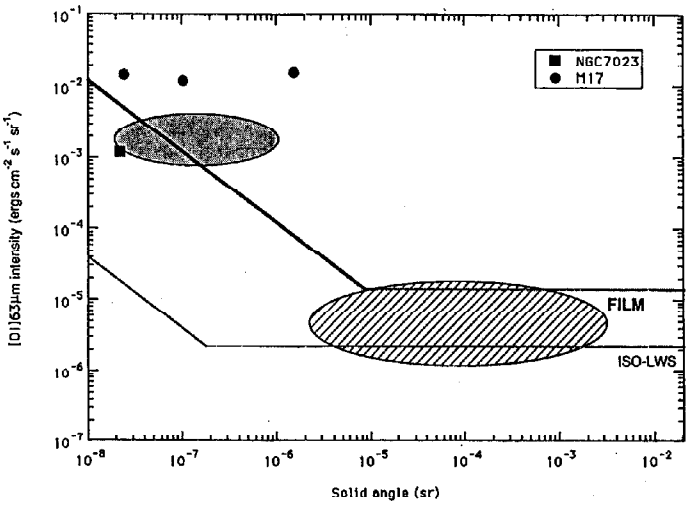

Fig.7 Same as Figure 6, except for the [O I] channel. Hatched region: expected diffuse [O I] emission from the Galactic plane (see 2.1). Shaded regions: shocked gas (see 2.3).

The FILM also has an advantage over the LWS on the ISO (Scientific Capabilities of the ISO Payload, 1991) in observing the [C II] emission from sources which extend over 10 arcminutes.

However, as for the detection limit of the [O I] channel, it is 3 times worse than that of the ISO-LWS. The FILM will survey about 10 % of the entire sky with these detection limits, where the ISO-LWS is expected to concentrate mainly on mapping and resolving of small scale structures. Therefore, the FILM and ISO-LWS can be a complementary pair of far-infrared spectroscopic instruments, not only for the [O I] line but also for the [C II] line.

5 Summary

The Far-Infrared Line Mapper (FILM) on the Infrared Telescope in Space (IRTS) has been developed and tested in the laboratory. The FILM will simultaneously measure the [C II] 158 μm and [O I] 63 μm line intensities

with high sensitivity for extended sources and spatial resolution of 8 arcmin × 13 arcmin, and provide intensity maps over 10 % of the sky. Investigations of diffuse [C II] emission from the Galaxy, infrared cirrus clouds, and the cooling process of interstellar clouds will be significantly advanced by the FILM.

Many people at ISAS have contributed to the development of the FILM, including M. Narita and other members of IR group at ISAS. Among them, Mrs. Y. Yamashita Yui fabricated an excellent low-pass filter for the FILM. K. Okumura and H. Yano assisted us at the laboratory calibration of the FILM. We have been supported technically by Prof. H. Ishimoto at University of Tokyo for making a high thermal conductive copper, by S.M. Smith at NASA/ARC for providing a black coating, by Mitaka Kohki for machining the complex FILM structure, and by Nikon for developing a unique grating. We specially thank T. Matsumoto, H. Murakami, T. Onaka, and other members of IRTS project.

References

Bock, J., et al. 1993, in AIP Conf. Proc. No. 278, Back to the Galaxy, ed. S. S. Holt and F. Verter (New York: AIP), 299

Bock, J., & Lange, A. E. 1993, preprint

Burton, M. G., Hollenbach, D. J., Haas, M. R., & Erickson, E. F. 1990, ApJ, 355, 197

Cohen, M., Hollenbach, D. J., Haas, M. R., and Erickson, E. F. 1988, ApJ, 329, 863

Cooksy, A. L., Blake, G. A., & Saykally, R. J. 1986, ApJ, 305, L89

van Dishoeck, E. F., & Black, J. H. 1988, ApJ, 334, 771

Doi, Y., Nakagawa, T., Yui, Y. Y., Okuda, H., Shibai, H., Nishimura, T., & Low., F. J. 1993, in AIP Conf. Proc. No. 278, Back to the Galaxy, ed. S. S. Holt and F. Verter (New York: AIP), 307

Draine, B. T., Roberge, W. G., & Dalgarno, A. 1983, ApJ, 264, 485

Gry, C., Lequeux, J., & Boulanger, F. 1992, A&A, 266, 457

Hiromoto, N., Itabe, T., Shibai, H., Matsuhara, H., Nakagawa, T., & Okuda, H., 1992, Applied Optics, 31, No.4, 460

Hollenbach, D., & McKee, C. 1989, ApJ, 342, 306

Hollenbach, D. J., Takahashi, T., & Tielens, A. G. G. M. 1991, ApJ, 377, 192

IRAS Catalogs and Atlases: Explanatory Supplement. 1988, ed. C. A. Beichman, G. Neugebauer, H. J. Habing, P. E. Clegg, & T. J. Chester (Washington, DC:GPO)

ISO Scientific Capabilities of the ISO Payload. 1991, ISO-SSD-8805, Issue 1.0, ESA

Lange, A. E., Freund, M. M., Sato, S., Hirao, H., Matsumoto, T., & Watabe, T. 1993, ApJ, in press

Low, F. J., et al. 1984, ApJ, 278, L19

Matsuhara, H., et al. 1992, in Chemistry and Spectroscopy of Interstellar Molecules, ed. D. K. Bohme, E. Herbst, N. Kaifu, & S. Saito (Tokyo: Univ. Tokyo Press), 277

Murakami, H., et al. 1993, ApJ, in press

Nakagawa, T., et al. 1993, in AIP Conf. Proc. No. 278, Back to the Galaxy, ed. S. S. Holt and F. Verter (New York: AIP), 303

Noda, M., Matsumoto, T., Matsuura, S., Noguchi, K., Tanaka, M., Lim, M. A., & Murakami, H. 1993, ApJ, in press

Oda, N., Lemke, D., & Wolf, J. 1984, Inter. J. of Infrared and Millimeter Waves, 5, No.11, 1499

Okuda, H., et al. 1989, in IAU Symp. No. 136, The Center of the Galaxy, ed. M. Morris (Dordrecht: Reidel), 145

Pottasch, S. R., Wesselius, P. R., & van Duinen, R. J. 1979, A&A., 74, L15

Roellig, T., Onaka, T., & McMahon, T. 1993, ApJ, in press

Sakai, K., Nakagawa, Y., & Yoshinaga, H. 1968, Jpn. J. Appl. Phys., 7, 792

Shibai, H., et al., 1991, ApJ, 374, 522

Stacey, G. J., Viscuso, P. J., Fuller, C. E., and Kurtz, N. T. 1985, ApJ, 289, 803

Stark, R. 1990, A&A, 230, L25

Tielens, A. G. G. M., & Hollenbach, D. 1985, ApJ, 291, 722

Wright, E. L., et al. 1991, ApJ, 381, 200

Zink, L. R., Evenson, K. M., Matsushima, F., Nelis, T., & Robinson, R. ApJ, 371, L85

The Far-Infrared Photometer on the Infrared Telescope in Space

A.E. Lange,[1] M.M. Freund,[1]
S. Sato,[2] T. Hirao,[2] T. Matsumoto,[2] and T. Watabe [2]

Accepted for Publication in the Astrophysical Journal

Abstract

We describe the design and calibration of the Far-Infrared Photometer (FIRP), one of four focal plane instruments on the Infrared Telescope in Space (IRTS). The FIRP will provide absolute photometry in four bands centered at 150, 250, 400, and 700 μm with spectral resolution $\lambda/\Delta\lambda \approx 3$ and spatial resolution $\Delta\Theta = 0.5$ degrees. High sensitivity is achieved by using bolometric detectors operated at 300 mK in an AC bridge circuit. The closed-cycle ^{3}He refrigerator can be recycled in orbit. A 2 K shutter provides a zero reference for each field of view. More than 10 % of the sky will be surveyed during the 3 -week mission lifetime with a sensitivity of $< 10^{-13}$ W cm^{-2} sr^{-1} per 0.5 degree pixel.

Subject Headings: Cosmology, Photometry, Infrared: General, Instruments

[1] Department of Physics, UC Berkeley, Berkeley, CA 94720, U.S.A
[2] Department of Physics, Nagoya University, Furocho, Chikusa-ku, Japan

1 Introduction

The diffuse brightness of the sky has been mapped over most of the electromagnetic spectrum, from radio to gamma rays. The sub-millimeter region (wavelengths from 100 μm to 1 mm) is a particularly rich area of the spectrum, containing the Wien limit of the 2.74 K cosmic microwave background (CMB), the peak of thermal emission from interstellar dust (ISD), a rich spectrum of fine-structure and molecular transitions from the gas phase of the interstellar medium (ISM), and the long wavelength tail of emission from interplanetary dust (IPD). The brightness of the diffuse continuum emission at wavelengths of 300 to 500 μm is lower than any other portion of the spectrum between the UV and the radio. This spectral window coincides with the peak brightness of the diffuse background expected from distant, infrared-bright galaxies.

Measurements of the absolute brightness of the diffuse sub-mm continuum require a space-borne, liquid ^{4}He-cooled telescope with excellent sidelobe rejection, and sensitive detectors. Several generations of rocket-borne instruments have measured the spectrum of the CMB (Gush, Halpern, & Wishnow 1990), the distribution of ISD emission (Lange et al, 1993), and line emission from the ISD (Bock et al. 1993a). Recently the first comprehensive, all-sky view of the sub-mm background has been produced by the COsmic Background Explorer (COBE) (Boggess et al. 1990). The FIRAS experiment on COBE has measured the spectrum of emission over the entire sky at wavelengths between 100 μm and 1 cm with 7 degree angular resolution, confirming the blackbody spectrum of the CMB (Mather et al. 1990), measuring the average spectrum of ISD emission, and detecting several lines emitted by the diffuse ISM (Wright et al. 1991). The DIRBE experiment has mapped the sky with finer resolution (0.7 degrees) in two sub-mm passbands, centered at 150 and 250 μm (Hauser et al. 1991).

This paper describes the Far InfraRed Photometer (FIRP), a multichannel absolute photometer with four passbands centered at 150, 250, 400, and 700 μm. The FIRP is one of four focal plane instruments on the InfraRed Telescope in Space (IRTS) (Murakami et al. 1993). The 15 cm, liquid ^{4}He-cooled telescope (Onaka et al. 1993; Sato et al. 1993) provides a 0.5° field of view for the FIRP, which is diffraction limited at a wavelength of 1 μm. Approximately 10 % of the sky will be surveyed during the 3 week mission. Other instruments include a Near Infrared Spectrometer (NIRS) (Noda et al. 1993), a Mid Infrared Spectrometer (MIRS) (Roellig et al. 1993), and a Far-Infrared Line Mapper (FILM) (Shibai et al. 1993).

2 FIRP Science Goals

Coverage over the entire sub-millimeter band with high sensitivity and 0.5 degree spatial resolution makes the FIRP ideal for studying continuum emission from ISD, and for probing the cosmological "window" at 300 - 500 μm. The FIRP observations will complement both the FIRAS and the DIRBE observations by providing higher angular resolution than FIRAS, and by extending the DIRBE observations to longer wavelengths and higher sensitivity.

2.1 Temperature distribution of the ISD

The sky-averaged spectrum of the diffuse sub-millimeter continuum background measured by FIRAS is dominated by the CMB at wavelengths > 500 μm, and by emission from ISD at wavelengths of 100 to 500 μm. When the spectrum of the CMB is removed, the residual spectrum is best fit by a two-temperature model of the form (Wright et al. 1991):

$$I_\nu \propto \nu^2 \{B_\nu\,(20.4\ \mathrm{K}) + 6.7\ B_\nu\,(4.77\ \mathrm{K})\}$$

where $B_\nu(T)$ is the Plank function and the n^2 dependence describes the scaling of emissivity with frequency expected for emitters that are small in comparison with the wavelength of emission. That this two component model formally fits the data better than a single component model suggests the existence of a population of interstellar dust grains that are efficient long wave emitters, such as conducting needles or fractal dust grains (Wright 1987). The observed spectrum of ISD emission could result either from a mixture of two populations of ISD that equilibrate at different temperatures, or from the existence of efficient long-wave emitters that have a heat capacity sufficiently small that absorption of a single UV photon heats them significantly. In the latter case, the observed "two-component" spectrum could be an artifact resulting from a homogeneous population of dust emitting over a range in temperature. In either case, the spectrum of the ISD emission should exhibit spatial variation due to the variation in dust grain properties and/or incident radiation field. Sub-mm measurements at higher angular resolution probe this variation with greater sensitivity, and should, when combined with other probes of the ISM, provide clues to the detailed nature of the ISD emission. DIRBE provides limited information on this aspect of ISD emission. Its spectral coverage extends only to 300 μm, and thus misses the region of the spectrum from 300 μm to 1 mm where emission from the "cold component" should be

observable. In addition, the sensitivity of the DIRBE sub-mm channels at 150 and 250 μm provides only modest signal-to-noise at high galactic latitudes.

2.2 Anisotropy of the Cosmic Background Radiation

Though the FIRP beamsize is matched to the angular scales on which standard cold dark matter scenarios predict that the temperature anisotropy of the CMB will peak (Bond 1989) the confusion from ISD at sub-mm wavelengths will prevent the FIRP from reaching interesting limits. Several experiments have been designed and are now operating which attempt to measure the anisotropy of the CMB at mm wavelengths on these angular scales (Fischer et al. 1991). Confusion by ISD emission will ultimately limit the sensitivity of measurements of CMB anisotropy at wavelengths of 1 to 3 mm (Fischer et al. 1993). Attempts to model this emission using high signal-to-noise data available from IRAS and DIRBE at wavelengths $\leq$ 100 μm may be confounded by spatial inhomogeneities in the temperature and/or spectral index of the dust, since these measurements are made in the Wien limit of the dust spectrum, and must be extrapolated over a decade of frequency. Observations of ISD emission with the FIRP at wavelengths adjacent to those at which CMB anisotropy observations are conducted will improve the precision with which mm-wavelength ISD emission can be modeled and subtracted from CMB anisotropy measurements.

2.3 The Extragalactic Sub-mm Background

Measurements of the diffuse electromagnetic background probe all radiative processes in the universe over a volume which depends on the absorption depth for radiation. For sub-mm measurements, this volume includes the entire universe back to the last scattering surface of the CMB at $z = 1000$, in the standard scenario in which the reionization occurs at $z < 4$. The sub-mm background thus contains the integrated light from all radiative processes that have taken place in the post-recombination universe at wavelengths of $(100 - 1000)/(1 + z)$ μm where z is the redshift of emission. The sub-mm extragalactic background is thought to be dominated by emission from distant, infrared bright galaxies (Beichman, & Helou 1990; Wang 1991). The brightness and spectrum of the sub-mm extragalactic background depends on the rate of star formation as a function of redshift, and on the dust opacity along the line of sight. For high dust opacity, most of the starlight emitted at high redshift will be absorbed and re-radiated in the infrared, and will appear in the sub-mm. For low dust opacity, the optical depth to starlight emitted at high redshift will be small, and the

starlight will appear in the near infrared.

The extragalactic infrared background has yet to be reliably detected at any wavelength. Observations to date have shown that the diffuse background over most of the sky is dominated by foreground emission from the Galaxy and the Solar System throughout the infrared. Accurate modeling of the spectrum and spatial distribution of these local sources of emission is necessary in order to detect an isotropic extragalactic background. Emission from ISD is the dominant source of foreground emission in the sub-mm. This emission decreases rapidly at long wavelengths, creating a deep spectral window at 300 to 500 μm between the ISD emission and the CMB through which the infrared emission form distant galaxies may be observable. Another window at 3 to 5 μm, between the scattered sunlight and the thermal emission from the interplanetary dust, provides the best hope of observing the near infrared background due to redshifted starlight. These two windows are targeted by the FIRP and the NIRS, respectively, which will have overlapping sky coverage.

The sensitivity and spatial resolution of the FIRP will allow the diffuse background to be mapped with good signal-to-noise in the dimmest regions of the sky. The wavelength coverage extends to 800 μm, and includes a passband tailored to the 300 to 500 μm spectral window. This data set, in addition to the data from the NIRS, MIRS, and FILM should significantly improve models of the local backgrounds based on the all-sky coverage of the DIRBE and FIRAS experiments on COBE, allowing a more accurate determination of the isotropic extragalactic background.

3 The IRTS Misson

The IRTS is one of ten experiments that will be placed into orbit on the first Space Flyer Unit (SFU-1), which is scheduled for launch from Tanegashima Space Center in early 1995. The SFU will be placed into a nearly circular, 482 km altitude, 28.5 degree inclination orbit. The entire IRTS experiment, including the warm electronics, has a mass of 182.6 kg, and a volume of approximately 3 m^3.

After a nominal seven day checkout and degassing period in orbit, the IRTS aperture cover will be ejected, and observations will begin for all four instruments. During the twenty days of observing, the SFU mission will be dedicated to IRTS observations. The SFU attitude will be determined by the earth and sun avoidance requirements of the IRTS, and all other experiments on the SFU will be powered down in order to eliminate potential interference with the sensitive IRTS electronics. Present tests of

the flight cryostat indicate that the superfluid ^{4}He hold time will be more than adequate to last through the extended observation period. After a period of 6 - 18 months after launch, the SFU-1 is scheduled to be retrieved from orbit by NASA's Space Transportation System for refurbishment in the future.

The scan pattern of the IRTS telescope is determined by earth and sun avoidance requirements, and the low-inclination orbit (Murakami et al. 1993). The scan keeps the sun > 70 ° from the optical axis at all times, and the earth's limb > 93° from the optical axis in the best orbits, and > 43 ° from the optical axis in the worst orbits. The optical axis of the telescope will sweep a great circle on the sky once per orbit, the plane of the circle inclined 20 degrees to the earth-sun axis. Sky coverage will thus include solar elongation angles of 70 to 110 degrees. The scan rate will be 0.067 degrees/sec, or 8 sec/field-of-view for the FIRP. The axis of the great circle scan will be precessed at a rate of 360 degrees/year, or 0.067 degrees/orbit. The FIRP will thus observe point sources on eight or more consecutive orbits, the redundant coverage being minimal in the plane of the ecliptic, and maximum near the ecliptic poles. Approximately 10 % of the sky will be observed in the anticipated 21 day mission.

The IRTS telescope is of Ritchey-Chretien design with gold-coated aluminum optics (Onaka et al. 1993). The system of baffles employs a combination of sunshade, passively cooled aperture shield, cryogenically cooled specular forebaffle, and black aftbaffle (Sato et al 1993). The specular forebaffle reflects radiation incident at > 40 degrees off axis out of the telescope, keeping the aperture heat load below 20 mW for earth-avoidance angles of > 40 degrees (Bock et al. 1993b). The telescope is surrounded by a 100 liter liquid ^{4} He cryostat, which is pumped through a porous plug to the vacuum of space to a temperature of < 1.8 K. The aftbaffle and the telescope optics are thermally coupled directly to the ^{4}He tank, and are cooled to < 2 K. The forebaffle is cooled to < 10 K by heat exchange with the venting ^{4} He gas in the least favorable orbits, and can be cooled to < 2.5 K via a gas-gap heat switch that thermally grounds the forebaffle to the ^{4}He tank during more favorable orbits, when the earth limb remains > 58 degrees off-axis.

Data from all four of the focal plane instruments, a focal plane star-sensor, and telescope housekeeping are multiplexed into a 6 kb/s common telemetry stream, and stored in the spacecraft's 80 Mbit bubble memory. The data is telemetered to the ground during brief downlinks as the spacecraft passes over receiving stations in NASA's Deep Space Network and Japan's Kagoshima Space Center. After recording and on-site archiving, the data will be transmitted to the IRTS Science Operations Center at the Institute for Space and Astronautical Science in Japan for processing. The entire IRTS data set will eventually be made available to the public through

the Image Processing and Analysis Center (IPAC) in the United States.

4 FIRP Instrument Description

The modest scale of the IRTS mission presented all of the focal plane instruments with severe constraints in size, mass, power dissipation, complexity, and data rate. Since all four focal plane instruments are intended to be operated simultaneously, it was important to eliminate all sources of optical, electrical, thermal, and mechanical interference between the instruments. As the IRTS facility does not provide infrared calibration

TABLE 1
FIRP Specifications

Size Irregular shape	16 cm x 15 cm x 11 cm overall
Weight	2185 gm
Electrical Power Dissipation	Cold Part: 2 3 mW typical, 17 mW peak, Warm Part: 2 W
Cryogenic Parameters:	
$T_{\text{coldplate}}$	< 1.8 K
T_{housing}	1.92 K
$T_{\text{telescope}}$	1.91 K
T_{still}	≈ 293 mK
T_{phot}	≈ 319 mK
T_{pump}	≈ 2.1 K
^{3}He Lifetime	≈ 9-10 days
^{3}He Cycle Time	≈ 20 hours
Cooling Power of Still	≈ 12 J
Heatload (on still)	≈ 14.6 μW
Entrance Aperture	4 mm diameter (0.5 degree on sky) Winston Concentrator with flared entrance aperture.
Detectors	Composite bolometers in AC bridge with dark reference detectors.
Shutter Frequency	1/8 Hz (4 s open / 4 s closed 8 s per FOV)
Cold Amplifiers	Model J-1, Infrared Laboratories
Data Rate	6 kb/s (standard) 3 kb/s (reduced)

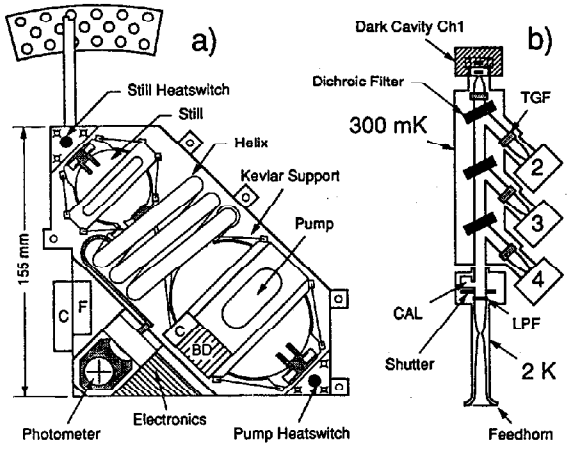

Fig.1a The FIRP, viewed from top along the optical axis of the telescope. The photometer and the refrigerator are optically isolated from each other. Two gas-gap heat switches are used to cycle the ^{3}He refrigerator in zero-g. Kevlar suspension systems thermally isolate the pump, still, and photometer from the 2 K housing. The Cu cold strap minimizes thermal gradients between the FIRP and the ^{4}He cryostat. A burst disk "BD" attached to the refrigerator prevents overpressure. The cold electronics consist of four dual JFET amplifiers. Electrical connection to the refrigerator and to the photometer is made separately via two connectors "C" with integrated Eccosorb filters "F" (Emmerson Cuming) for RF-noise protection, with about 100 db attenuation above about 100 MHz.

Fig.1b A schematic of the FIRP optical path. After the 2 K feed optic the beam passes the primary low pass filter (LPF), the shutter, and the CAL lamp cavity, before entering the 300 mK photometer. The beam propagates via light pipe inside the photometer. Three dichroics separate the incoming beam into 4 passbands, labeled by wavelength. Thick-grill filters (TGF) provide additional high-pass filtering for each band. Radiation from each band is concentrated into an integrating cavity containing a composite bolometric detector. A second, matched detector is located in an adjacent dark cavity. The two detectors are operated in an AC bridge.

sources, each instrument must incorporate its own. To meet the FIRP science goals within these constraints, a simple optical system based on a four-channel photometer was chosen. The design of the FIRP is illustrated in Figs. 1 a, b. A closed-cycle ^{3}He refrigerator that can be recycled in orbit, and has no moving parts was developed to provide a 0.3 K heat sink for the bolometric detectors. A novel bolometric detector system was developed that eliminated the need for rapid signal modulation via a mechanical chopper. The only moving part in the instrument is a 2 K shutter that provides a zero reference. The most important specifications and performance characteristics of the FIRP are given in Table 1. A more detailed description of the instrument is given below.

4.1. Optical Components

The IRTS focal plane is divided among the science instruments and a near infrared star sensor by a set of pick-off mirrors. The FIRP feed optic, a compound parabolic concentrator (Winston 1970), occupies the center of the focal plane, and defines a 0.5 degree FWHM field of view. The acceptance angle of the FIRP is matched to the f/4 beam at the focal plane. The entrance apertures of the NIRS, FIRP and MIRS are collinear along the scan direction of the telescope. The entrance apertures of the FILM, FIRP, and star sensor are collinear perpendicular to the scan direction.

The optical path of the FIRP is shown in Fig. 1b. The entrance aperture of the FIRP feed optic is smoothly flared with a 2 mm constant radius of curvature in order to reduce diffraction. A second compound parabolic reflector placed at the exit aperture of the feed optic re-collimates the beam to f/2.8 into light-pipe optics before it enters the instrument.

The beam first passes through a Yoshinaga-type filter (Yamada, Mitsuishi, & Yoshinaga 1962) with a low-pass cut-off at 100 cm^{-1}. The filter is identical to that used previously in rocket-borne measurements of the sub-mm background (Lange et al. 1987), and has been confirmed to have high out-of-band rejection throughout the infrared. The filter forms the high frequency edge of the 150 μm passband, and provides additional out-of-band blocking for the other passbands.

After passing the shutter, described below, the beam enters the 300 mK photometer which houses the dichroic beamsplitters (Ade et al. 1984), out-of-band blocking filters, and bolometric detectors. The 300 mK photometer is thermally isolated from the 2 K shutter module by a 300 μm gap in the 4 mm diameter light pipe. The photometer is held rigidly in place via an 8-point Kevlar suspension system (Duband, Hui, & Lange 1993).

Each of the three dichroic beamsplitters is a multi-layer capacitive-mesh

low-pass filter used at 22.5 degrees angle of incidence (Ade et al. 1984). The half-power points of the three dichroics are at 200, 350, and 600 μm. The beam is incident on the dichroic filters in order of decreasing cut-off frequency, separating off the passbands in order of decreasing frequency. This ordering provides additional blocking of high frequency out-of-band leaks for the lowest frequency channels. The long wavelength edge of the three shortest wavelength passbands is formed by the reflection spectrum of the dichroics, which drops to < 3 % in-band. The inband transmission of the dichroics is high (80 %) so that the loss incurred by transmission through several dichroics is small.

After emerging from the system of dichroics, each beam passes through a thick-grill filter (Timusk & Richards 1981) which provides low-frequency blocking, and is then concentrated into an integrating cavity by an f/2.8 compound parabolic reflector. The thick-grill filter in the 700 μm channel forms the long-wavelength edge of the band and has cut-off at 850 μm. The thick grill filters in the other three channels are used to improve the long-wavelength blocking in the region where the CMB spectrum is steeply rising, and they have identical half-power points at 475 μm.

4.2 Shutter

The shutter is located immediately behind the low-pass filter. In normal operation, the shutter modulates the beam at 1/8 Hz in a square wave with 4 s open and 4 s closed, providing a zero-reference for each field-of-view. The large number of duty cycles, the strict limits on power dissipation, and the acoustic sensitivity of bolometric detectors required a novel design. The shutter that we have developed is a modification of a shutter developed for the Long-Wave Spectrometer on ISO. The blade is mounted on a flex pivot, along with two SmCo permanent magnets. Two solenoids with soft iron cores are positioned such that the combination of the spring force due to the flex pivot, and the magnetic force between the permanent magnets and the solenoid cores creates a potential with two stable minima corresponding to the open and closed positions of the shutter. When the solenoids are energized, the permanent magnets are repulsed form one pole piece and attracted towards the other, temporarily creating a potential with a single stable position.

In order to cycle the shutter between open and closed, the solenoids are energized for 50 ms with approximately 10 mA of current, alternating the polarity of the pulse every 4 s. The absence of hard-stops makes the motion acoustically quiet. Oscillation of the shutter blade in the magnetic potential is damped by Eddy current damping induced in the high-purity copper blade by two small SmCo magnet placed beneath the blade. The switching

time is less than 100 ms, shorter than the time constant of the bolometric detectors. After each shutter operation, a transient in the signal in the lowest frequency channel is observed, due to heating of the shutter blade by the Eddy current damping. This transient decays with a 300 ms time constant, and is approximately symmetric with respect to the shutter opening and closing. The response to the transient is thus subtracted to first order in the signal processing, described below, which difference the average signal observed during the shutter open and closed phases.

4.3 Detectors

The FIRP achieves high sensitivity by using low-background, long time-constant bolometric detectors cooled to 0.3 K. The details of bolometer theory have been described by Mather (1984). The FIRP bolometers have been described by Devlin et al. (1993). An infrared absorber with a heat capacity C is thermally isolated from a heat sink of temperature T_0 by a link with a thermal conductivity G. The power P incident on the absorber induces a temperature difference $(T - T_0) = P / G$. The absorber temperature responds to changes in the power with a time constant $t=C/G$. A thermistor is attached to the absorber, and measures the temperature. The FIRP bolometers at 300 mK have a thermal conductivity $G = 1.5 \times 10^{-10}$ W/K, a heat capacity $C = 10^{-11}$ J/K, and a time constant t=150 ms. The measured electrical noise equivalent power (NEP) of each detector is 2×10^{-17} W/Hz$^{1/2}$.

The bolometers are biased in an unconventional manner that reduces 1/f noise. Each illuminated detector is paired with a thermally-matched dark detector in the bridge circuit shown in Fig. 2. The bridge is biased with a square-wave AC voltage between 73 and 215 Hz, depending on the channel, producing a carrier frequency that is well above the 1/f knee of the amplifier. The output of the bridge is amplified by a cold J-FET source follower, and then differentially amplified by warm electronics, producing an AC signal that has an amplitude proportional to the power absorbed in the active detector. The AC signal is phase-synchronously demodulated and integrated before digital sampling at 4 Hz. The AC bridge readout is described in detail by Wilbanks et al (1990).

Differencing the signal between detectors with matched thermal response reduces 1/f noise due to fluctuations in the heat sink temperature. Using the AC bias eliminates contributions from 1/f noise in the amplifier chain. The reduction in 1/f noise allows signal modulation at low frequency, thus eliminating the need for a chopper and allowing slower, and thus more sensitive, detectors to be used. The FIRP signal modulation is accomplished by operating a cold shutter at 1/8 Hz.

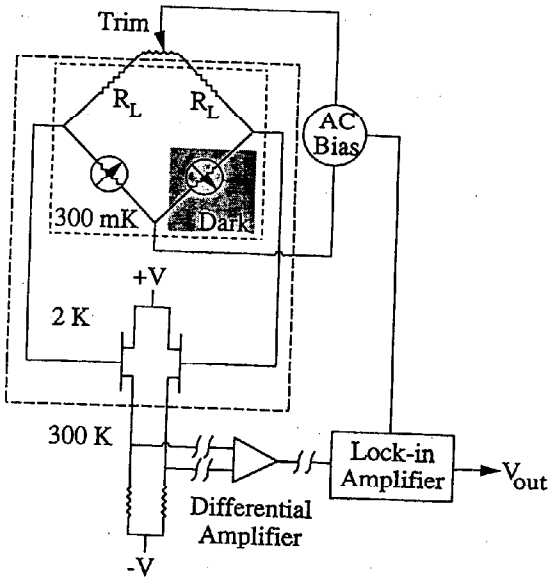

Fig.2 A schematic of the AC bridge readout used for the bolometric detectors. $R_L = 10.0$ MΩ denote the load resistors.

4.4 ^{3}He Refrigerator

The ^{3}He refrigerator provides the 300 mK base temperature needed for the operation of the FIRP detectors. The three main requirements for the FIRP ^{3}He refrigerator are: (i) the ability to condense ^{3}He and operate in zero-g with minimal heating of the focal plane, (ii) a long holdtime and high duty cycle in orbit, and (iii) a self-contained and compact design that requires no mechanical penetration of the instrument cavity. A detailed description of the design of the FIRP refrigerator is given by (Duband, Hui, & Lange 1990). A prototype refrigerator has been tested on a sounding rocket, verifying the performance in zero-g Duband et al. (1990).

The FIRP refrigerator has five major components, as shown in Fig. 1a: an evaporator, a helical pump tube, a sorption pump, and two heat switches.

The evaporator holds the ^{3}He liquid during normal operation. It is filled with a silicose sponge, which contains the liquid ^{3}He in the still by surface tension. A thin-walled, stainless-steel helical pump tube connects the evaporator to the sorption pump, and provides a large ratio of pumping speed to thermal isolation. The sorption pump is filled with activated charcoal, which adsorbs ^{3}He gas at low temperatures and releases the gas at temperatures > 15 K. The still and the pump are each separately suspended in Kevlar harnesses (Duband, Hui & Lange 1993). Thermal contact to each can be made via gas-gap heat switches that have switching ratios of 2000 (Duband, Hui & Lange 1990). The refrigerator is charged with 16.8 liter-STP of ^{3}He. The room temperature pressure is 68 bar. A burst disk limits the maximum operating pressure to 120 bar.

Operation of the ^{3}He refrigerator is initiated after all of the components have been cooled to 2 K, and the ^{3}He gas is absorbed in the pump. Liquid ^{3}He is condensed in the evaporator by thermally grounding the evaporator to the 2 K heat sink via the heat switch, and heating the pump to desorb the ^{3}He gas. The evaporator is the coldest point in the system at this point, ensuring that liquid condenses in it. A full cycle, which condenses 95 % of the gas, requires heating the pump to 40 K. The speed of condensation is limited by the thermal contact with the 2 K heat sink. A full condensation requires 16 hours, during which 27 mW of power is applied to the pump, 10 mW flows to the 2 K heat sink, and the remainder is stored in the heat of condensation of the liquid.

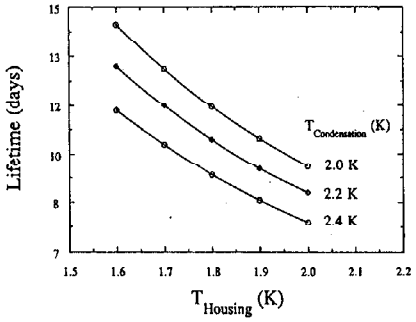

Fig.3 The calculated lifetime of the ^{3}He refrigerator as a function of housing temperature during operation and condensation temperature (2.0, 2.2, and 2.4 K). The most likely FIRP housing temperature is between 1.7 and 1.85 K, with a predicted condensation temperature of about 2.2 - 2.3 K. Therefore the most likely lifetime of the ^{3}He refrigerator is between 9.5 and 11 days.

In the second part of the cycle, the evaporator is thermally isolated, and the pump is thermally grounded to the 2 K heat sink. Absorption of ^{3}He gas in the pump reduces the vapor pressure in the evaporator, cooling it to 290 mK. The operating time between recycles is determined by the efficiency of condensation and by the heatload, both of which are functions of the heat sink temperature. With a 2 K heat sink, a total heatload of 15.1 mW is due to conduction through the evaporator heatswitch (7.5 mW), the helical pump tube (3.1 mW), the Kevlar suspension of the evaporator, the photometer (0.5 mW), and electrical leads (4 mW). Fig. 3 depicts the dependence of the lifetime of the still as function of both the condensation temperature ($T_{\rm still}$) and the housing temperature ($T_{\rm housing}$). For the operating conditions anticipated in orbit, the expected holdtime of the refrigerator is > 10 days, giving a duty cycle efficiency of > 90 %.

In order to achieve this efficiency, it is essential to provide good thermal contact between the FIRP and the liquid ^{4}He in the IRTS cryostat. A high purity Cu heat strap connects the Cu base of the evaporator heat switch and the FIRP housing directly to the Al ^{4}He tank. The strap is 0.4 cm^2 x 15 cm, and attaches to a 21 cm^2 flange on the cryostat with fifteen M3 screws. Electrical isolation of the FIRP from the cryostat is accomplished by a Cu-epoxy-Cu sandwich at the flange using Stycast epoxy (Emmerson Cuming) that has a thermal conductivity at 2 K of 350 mW/K. The thermal conductivity between the evaporator and the liquid ^{4}He is dominated by the Al cryostat itself, and is of the order of about 100 mW/K. A complete list of operating parameters of the FIRP ^{3}He refrigerator is included in Table 1.

4.5 Thermometry

The FIRP housekeeping continuously monitors temperatures at five positions: the photometer, the still, the pump, the shutter module, and the telescope primary. The pump thermometer is a Si diode. The photometer, still, and telescope primary thermometers are Ge resistance thermometers. The shutter thermometer is a carbon resistor. Zero-offsets are checked at 256 second intervals by nulling the bias currents for all thermometers (except the photometer thermometer) for one second. In addition to the FIRP housekeeping, the IRTS system housekeeping monitors a variety of temperatures in the telescope, baffle system, cryostat, and electronics.

4.6 Internal Calibration Source

The primary calibration of the FIRP will be provided by observing bright regions of the sky that will have already been mapped by the DIRBE

at similar angular resolution with good signal-to-noise in the two shortest wavelength channels. Extrapolations of the brightness of these regions to longer wavelengths using the FIRAS and balloon-borne data (Fischer et al. 1992) will be used to calibrate the longer wavelength channels. These primary calibrations will be frequent, since the scan path will cross the galactic plane twice each orbit.

In order to measure the gain stability more frequently, two internal calibrator lamps are activated every 256 seconds. The lamps consist of doped Ge thermistors, mounted on 1 mil (25 μm) brass wires, and suspended in a cavity. The cavity is connected to the light pipe by a 0.8 mm hole just behind the shutter and primary Yoshinaga filter. During the calibration sequence, the lamps are activated for 2 seconds with a constant current bias in the middle of an extended shutter close, which lasts 10 seconds. Electro-thermal feedback quickly stabilizes the temperature of the calibrator lamps at approximately 20 K, providing a signal to noise of several hundred in the four channels.

4.7 Electronics

Cold JFET amplifiers positioned a few cm from the photometer are used as the first stage of the differential amplifier for each AC bridge circuit. The JFET amplifiers are heat sunk to the 2 K instrument housing. A total power dissipation of 500 mW per JFET pair maintains the device at approximately 65 K, for optimum noise performance. The JFET amplifiers are operated as source followers, providing unity voltage gain, and with an output impedance of approximately 4 K Ohm.

The FIRP warm electronics is mounted on a single board, and consists of an analog part, which handles all the signals to and from the cold FIRP, the star sensor, and the telescope thermometer; and a digital part which interfaces with the IRTS common board and the IRTS data processing unit (DPU). The analog part provides the bias signals for the different FIRP channels and the photometer thermometer. The FIRP board generates six bias frequencies (between 73 and 215 Hz), which were chosen to minimize crosstalk and sensitivity to external noise sources. The signal from the cold JFET source followers (one for each detector) is preamplified and phase-synchronously demodulated. The total gain of the amplifier chain is about 50,000.

4.8 Data Acquisition and Signal Processing

The FIRP telemetry stream is interwoven with that of the other focal plane instruments and the housekeeping data. The DC analog output of each

detector bridge is low-pass filtered by a 2-pole filter with a cut-off at 2 Hz, and sampled at 8 Hz by a 16 -bit A/D converter. The sampling rate for the thermometers is 2 Hz.

Fig. 4 shows the digitally sampled output of the four detector channels during a calibration experiment in which the instrument is viewing a source which has brightness typical of the brighter regions of the sky. The modulation of the signal by the shutter at 1/8 Hz is apparent, as well as the response to the internal calibrator when the shutter is closed. There are 64 samples for each shutter period. We compute the average signal for the n^{th} shutter cycle, $\langle S_n \rangle$, as the difference

$$\langle S_n \rangle = \langle S_{open,\, n} \rangle - \frac{1}{2} \left(\langle S_{closed,\, n-1} \rangle + \langle S_{closed,\, n} \rangle \right).$$

This is the quantity that we are normally interested in, since the 8 s shutter period corresponds with the length of time required for the beam to move one diameter on the sky. In forming the signal averages for the shutter open and close periods, we normally delete several samples immediately following the shutter transient.

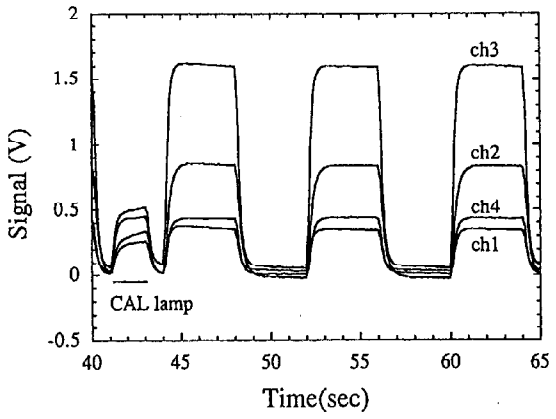

Fig.4 The digitally sampled signal output while the instrument views a 20 K blackbody source through a 0.1 % neutral density filter. The signal at the left during the period when the shutter is closed is due to the calibration lamp. In the normal flight calibration sequence, the calibration lamp is activated for 2 seconds every 256 seconds in the middle of a 10 second shutter closing.

5 Laboratory Performatnce and Calibration

The FIRP was tested and calibrated extensively in the laboratory prior to delivery to the flight cryostat. The testing and calibration proceeded in three phases: (1) spectroscopy of the flight filter system using a Michelson interferometer and high background 0.3 K bolometric detectors suitable for laboratory measurements (2) initial testing and calibration of the fully assembled instrument in a small test cryostat that contained the FIRP and a small blackbody calibration source that filled the field-of-view of the feedhorn, and (3) installation of the FIRP on the flight focal plane with the three other focal plane instruments, the star sensor, and the flight telescope, and calibration using a large blackbody calibrator.

5.1 Spectroscopy

The low-background flight detectors were unsuitable for measuring the spectral response of the instrument in the laboratory. The spectral response was measured prior to integrating the photometer into the flight housing, using high-background composite bolometric detectors with absorbing substrates identical to those used in the flight detectors. The bolometers were operated in a conventional AC-coupled, DC-biased readout to facilitate the measurements. The photometer and shutter module were installed in a small test cryostat that provided a 0.3 K cold stage for the photometer, and a 2 K cold stage for the shutter module containing the primary low-pass filter. All of the filters were thus at their normal operating temperature during the measurement.

The spectral response was measured using a step-and-integrate Fourier Transform Spectrometer, which keeps the signal modulation independent of wavelength, and thus eliminates effects due to finite detector time constants. The flight filter system viewed the spectrometer through a black polyethylene filter mounted on a LN_2 radiation shield, and a 1 mil polypropylene vacuum window at room temperature. Neither of these materials has any significant spectral features at sub-mm wavelengths. The output of the spectrometer was normalized by a using a second detector which viewed the spectrometer through separate, but identical, black polyethylene and polypropylene filters. The second detector was a composite bolometer (Lange et al, 1983) which accepted a larger throughput, corresponding to a long wavelength cut-off of 2 mm.

The measured spectral response for the four passbands are shown in Fig. 5. The spectral response should be independent of the specific bolometric detectors used, since the absorbing substrates of the composite bolometric detectors are tailored to have frequency independent absorption. That this is

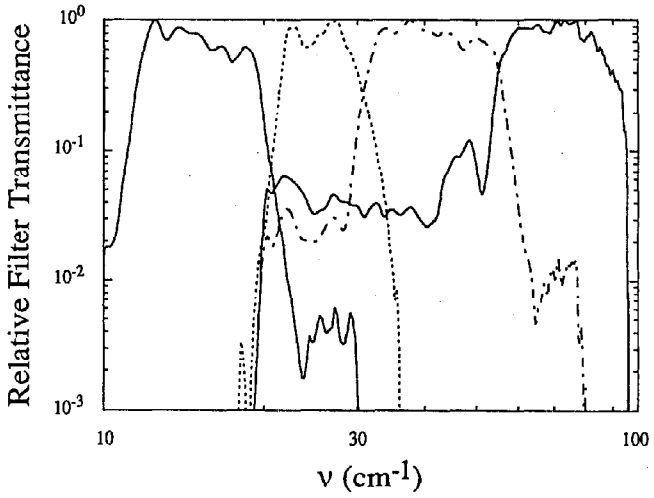

Fig.5 The measured spectral response of the four passbands. Note the low frequency leakage in the two highest frequency channels (ch 3 & 4).

so is confirmed by the laboratory calibration described below.

No evidence of out-of-band leaks from ≈ 50 μm to 3 mm was observed in the spectroscopy, to a level of < 0.1 % of the peak transmission. More stringent limits on the out-of-band response can be placed by separate measurements of the individual components. The transmission spectrum of the primary low-pass filter has been measured at wavelengths of 1 μm to 1 mm, and found to provide blocking throughout the infrared adequate to make the out-of-band response to the steeply rising spectrum of zodiacal light negligible in comparison with in-band response, even in the regions of the sky where ISD emission is dimmest. In addition, visible light measurements confirmed a high level of short wavelength rejection in the three longer wavelength channels by the dichroic filters. The measured response to a visible light source illuminating the entrance of the room temperature photometer was measured by placing a photo diode at the position of the 250, 400 and 700 μm detectors, and found to be 3×10^{-3}, 2×10^{-5}, and 10^{-7}, respectively.

5.2 Calibration

The responsivity of each channel was measured in several configurations using blackbody calibrators at temperatures between 1.6 and 30 K. In principle, only two blackbody temperatures are necessary in order to calibrate the gain and zero-offset of each channel. Measuring the response to a number of blackbody temperatures over a large range of temperature thus provides a powerful test for systematic errors in the calibration. For each blackbody temperature T, the power in each passband is calculated by convolving the measured spectral response with the Planck function $B_\nu(T)$. The measured response, normalized to the response to the calibrator lamps to correct for time-variations in the instrument gain, should be linearly related to the in-band power. Any errors in the spectroscopy or the blackbody thermometry, or non-linearities in the detector response, will be apparent as a deviation from linearity in the plot of response versus power. Particularly stringent tests of the spectroscopy are made when the measured data include temperatures which place the peak of the Planck function on either side of the passband.

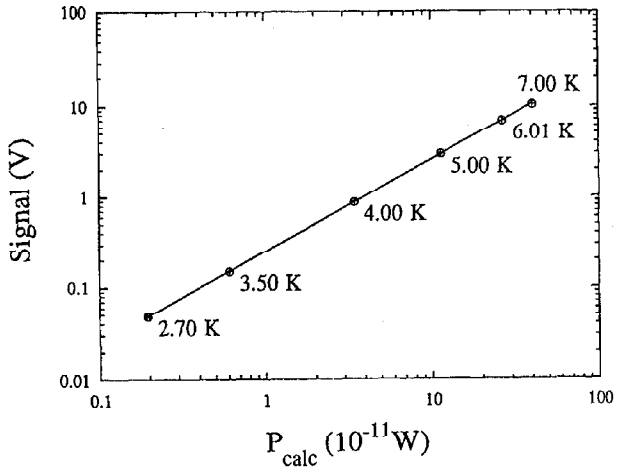

Fig.6 The result of the primary calibration experiment between 2.70 and 7.00 K for the 400 μm channel, as described in the text. The straight line is a linear fit, and the crosses are the error bars in the measured temperature and the measured signal.

The calibration was carried out in two environments. In the first, the FIRP was installed in a cryostat with a small blackbody that filled the field-of-view of the feedhorn. Two types of calibration experiment were performed in this configuration. In one, the blackbody was viewed directly over a temperature range of 1.6 to 8 K. In another the blackbody was viewed through a 0.1 % neutral density filter over a temperature range of 4 to 30 K. The overlap in temperature range of the two configurations confirmed the transmittance of the neutral density filter. Fig. 6 shows the calibration data for the 400 μm channel for the blackbody calibration from 2.70 to 7.00 K. The derived responsivity is constant to within 3 % over this temperature range. Fig. 7 shows a histogram of $\langle S_n \rangle$ for $T = 1.6$ K. The measured variance in $\langle S_n \rangle$ is 16 nV. The mean value, which corresponds to instrumental zero-offset that is not removed by the shutter modulation, is -0.7 nV. Since the typical amount of integration time per field of view will allow us to integrate down to a 1s noise level of approximately 2 nV, the offset is negligible in comparison.

The second experiment was conducted in a large test cryostat in which the flight telescope and all of the focal plane instruments were installed. A large blackbody cavity was installed just above the secondary shroud that contained a variable temperature blackbody, and had four exit apertures 4 mm in diameter, equally spaced around a 100 mm diameter circle in the face above the primary mirror. The holes were oriented so that the focal plane

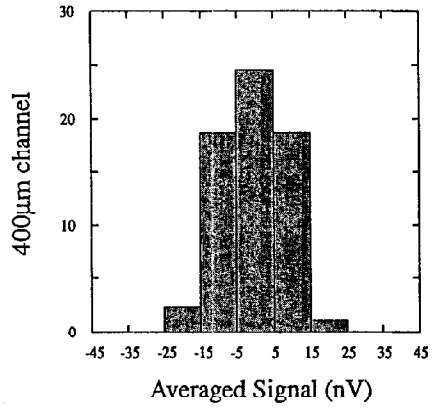

Fig.7 A histogram of the measured noise (in nV) of the shutter difference signal for the 400 μm channel, referred to the detector, after averaging over one shutter cycle.

would view them without obscuration by the secondary spiders. The copper walls of the cavity were maintained at close to 2 K, and the outside of the front surface, which was viewed by the focal plane, was painted black. The focal plane thus viewed a greybody with 0.3 % of the throughput at the temperature of the blackbody, and the remainder of the throughput at approximately 2 K. The blackbody temperature was controlled at six temperatures between 5 and 18 K.

This calibration was flawed by a small temperature rise of the black front surface for blackbody temperatures above about 10 K. Because the front surface fills such a large solid angle relative to the warm blackbody, even a small temperature rise produces significant emission, particularly in the long wavelength channels. The effects of the black front surface heating were modeled using the response of the 700 μm channel. The measured responsivity as a function of blackbody temperature after these effects are accounted for is shown in Fig. 8. The responsivity is constant to within 5 % for the three longer wavelength channels, for which the flux in band varies by more than two orders of magnitude. Larger deviations in the shortest wavelength channel are due to errors in spectroscopy, which underestimated the response at frequencies well below the passband. There is no evidence of any high frequency leak in any of the passbands.

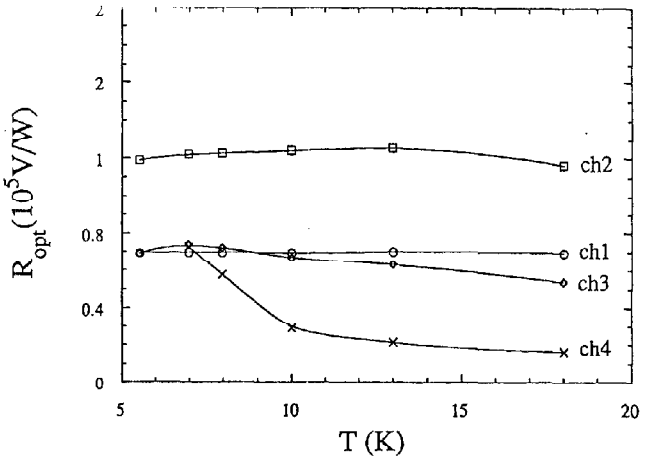

Fig.8 The results of the calibration in the telescope, as described in the text. R_{opt} is the optical responsivity accounting for the throughput of the intervening optics.

In a separate calibration experiment the IRTS telescope aperture was filled with a Eccosorb blackbody (Emmerson Cuming) with a single blackbody temperature. The responsivity of the system measured in this calibration relative to that measured without the telescope is 30 % lower, consistent with the obscuration due to the secondary mirror.

5.3 Beam Pattern Measurement

The beam pattern was measured by using a chopped thermal source which was collimated by a 50 cm Richy-Chretien telescope placed immediately in front of the IRTS. The collimating telescope was scanned in azimuth at several different altitude angles, in order to provide a 2-dimensional map of the beam. The FIRP shutter was disabled in the open position during the measurement, so that only the collimated source was modulated. High signal to noise measurements could be obtained only for the longer wavelength channels, due to atmospheric absorption. The beam pattern of the 400 μm channel is shown in Fig. 9. The beam has a FWHM of 0.4 degrees, with 90 % of the power contained within a diameter of 1 degree. Measurements for the other channels have lower signal to noise, but are consistent with the same pattern. The beams for the four channels are coincident with each other, as expected.

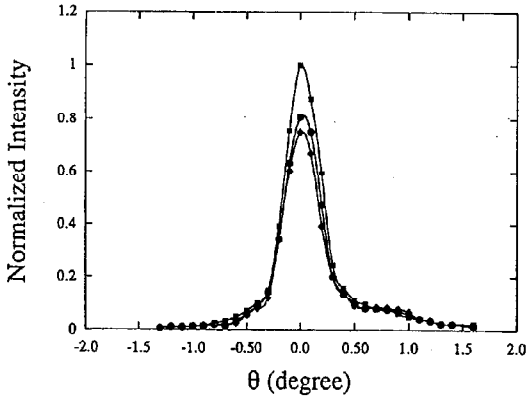

Fig.9 The measured beam pattern of the 400 μm channel. The squares indicate a scan through the center of the beam. The circles and the diamonds indicate scans displaced by ± 0.1 ° away from the center.

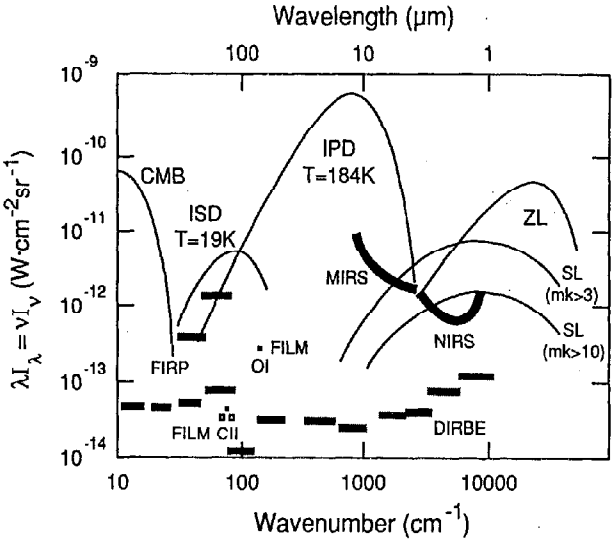

Fig.10 The sensitivity of the FIRP and the other three IRTS science instruments, compared with an estimate of the brightness of the diffuse background in a dark region of the sky. The different components are zodiacal light (ZL), thermal emission of the interplanetary dust (IPD) at 184 K and spectral index n = 1 (Hauser et al., 1984), integrated star light (SL), thermal emission from interstellar dust (ISD), and the 2.74 K cosmic background radiation (CMB). The two curves for integrated star light correspond to contributions from K magnitude m_k > 3 and m_k> 10. The FIRP sensitivity is calculated from the laboratory measurements of responsivity and noise. Also indicated are the published measured DIRBE sensitivity. All values correspond to 1s/ spectral element/ field of view/ mission. (values for DIRBE are for 1 year mission).

5.4 Sensitivity

The sensitivity of the FIRP depends on the responsivities determined by

the laboratory calibration and the measured noise. Of all four focal plane instruments on the IRTS, the FIRP is observed to be most vulnerable to excess noise produced by electromagnetic interference. This is not surprising, considering that the intrinsic spectral noise density of the detectors and cooled preamplifiers is < 20 nV / $\mathrm{Hz}^{1/2}$, at least one order of magnitude less than any of the other instruments. The degree of electromagnetic interference has been greatly reduced by isolating the FIRP electrically from the rest of the focal plane, connecting the housing to detector ground, and by adding pi filters to the focal plane cabling. In its present configuration, the variance of the average signals for each shutter cycle $\langle S_n \rangle$, is approximately 4.5 nV when all of the focal plane instruments are operating. The sensitivities of the four channels per pixel for this noise level are shown in Fig. 10, assuming that each pixel is observed in eight passes. The sensitivities for the four channels are about 4×10^{-14}, 4×10^{-14}, 5×10^{-14}, and 9×10^{-14} W cm^{-2} sr^{-1}, respectively. Pixels near the ecliptic poles will be observed more often, with correspondingly higher sensitivity.

6 Cnclusions

A Far Infrared Photometer for the Infrared Telescope in Space has been constructed, tested, and calibrated in the laboratory. The FIRP will provide observations of the diffuse sub-mm background with unprecedented sensitivity and/or spatial resolution at wavelengths of 100 to 800 μm. No other orbital mission now being planned will provide observations of the diffuse continuum from 200 to 800 μm, a region which contains an important window on the extragalactic background. FIRP observations over a fraction of the sky will, when combined with the all-sky coverage of the FIRAS and DIRBE instruments on COBE, help constrain models of the ISD emission. An improved understanding at the long wavelength spectrum and distribution of ISD emissions will reduce the effects of confusion by ISD emission on measurements of CMB anisotropy, and on searches for the sub-mm extragalactic background. Eventually, the calibrated data sets from all four focal plane instruments will be made available to the public through the Infrared Processing and Analysis Center.

Acknowledgements

Many people at U.C. Berkeley contributed to the development of the FIRP, including undergraduates Gary Brubaker, Sabrina Grannan, Sim Larkin, Steve Lumetta, and Fred Rieke; engineering aid Brent Grossman;

graduate students Dave Alsop, Jamie Bock, Mark Devlin, and Thor Wilbanks, and postdoctoral fellow Lionel Duband. Paul Richards was an active and invaluable participant in the early phases of this work. The Berkeley physics machine shop did an exceptional job in fabricating all of the mechanical components. Dr. Glen Eccord at NASA/JSFC provided invaluable help in safety qualifying the ^{3}He refrigerator for the STS.

The development of the FIRP has been supported primarily through NASA grant NAGW-1527. We gratefully acknowledge the support for development of technologies that made the FIRP possible from the National Science Foundation/Astronomical Instrumentation Division through a PYI grant to AEL and through a Research Opportunities for Undergraduates grant, from the Alfred P. Sloan Foundation, from the California Space Institute, and from NASA/AMES research consortium agreement NCA2-240. The integration of the FIRP into the IRTS was made possible in part by support from the Japan Society for the Promotion of Science in the form of a fellowship to MMF, and by support from the Japanese Institute of Space and Astronautical Science (ISAS) in the form of a Visiting Professorship for AEL. We especially thank Haruyuki Okuda, Hiroshi Murakami, Hiroshi Shibai, and other members of the ISAS staff and IRTS team for their kind support throughout this project.

References

Ade, P. A. R., Griffin, M. J., Cunningham, C. T., Radostitz, J. V., S.Predko, & Nolt, I. G., 1984, Infrared Phys., 24, 403

Beichman, C. A., & Helou, G., 1990, ApJ, 370, L1

Bock, J., et al., 1993a, ApJ, 410, 115

Bock, J., Lange, A. E., Matsuhara, H., Matsumoto, T., Onaka, T., & Sato, S., 1993b, Appl. Opt., submitted

Boggess, N. W., et al., 1992, ApJ, 397, 420

Bond, J. R., 1989, in Frontiers in Physics From Colliders to Cosmology, ed. A. Astbury et al. (Singapore: World Scientific), 182

Devlin, M., Lange, A. E., Wilbanks, T., Sato, S., IEEE Trans. Nucl. Sci., 1991, 40, 162

Duband, L., Alsop, D., Lange, A. E., & Kittel, P., 1990, Adv. Cryog. Eng., 35 1447

Duband, L., Hui, L., & Lange, A., 1990, Cryogenics, 30, 263

Duband, L., Hui, L., & Lange, A. E., 1993, Cryogenics, in press

Emmerson Cuming, 77 Dragon Ct., Wobern, MA 01888

Fischer, M. L., et al., 1992, ApJ, 388, 242
Fischer, M. L., et al., 1993, ApJ, submitted
Gush, H. P., Halpern, M., & Wishnow, E. H., 1990, Phys. Rev. Lett., 65, 537
Hauser, M. G., et al., 1984, ApJ, 278, L15
Hauser, M. G., Kelsall, T., Moseley, S. H., Jr., Silverberg, R. F., Murdock, T., Toller, G., Spiesman, W., & Weiland, J., 1991, in After the First Three Minutes., ed. S. S. Holt et al. (New York : American Institute of Physics)
Lange, A. E., Kreysa, E., McBride, S. E., Richards, P. L., & Heller, E. E., 1983, Int. J. Infrared Millim. Waves, 4, 689
Lange, A. E., Hayakawa, S., Matsumoto, T., Matsuo, H., Murakami, H., Richards, P. L., & Sato, S., 1987, Appl. Opt., 26, 401
Mather, J. C., 1984, Appl. Opt., 23, 584
Mather, J. C., et al., 1990, ApJ, 357, L37
Murakami, H., 1993, ApJ, in press
Noda, M., Matsumoto, T., Matsuura, S., Noguchi, K., Tanaka, M., Lim, M., & Murakami, H., 1993, ApJ, in press
Onaka, T., Yagi, T., Shibai, H., Kohno, T., Tanabe, T., & Murakami, H., 1993, Appl. Opt., in press
Roellig, T., Onaka, T., McMahon, T. J., & Tanabe, T., 1993, ApJ, in press
Sato, S. et al., 1993, preprint
Shibai, H., Yui, M., Matsuhara, M., Hiromoto, N., Nakagawa, T., & Okuda, H., 1993, ApJ, in press
Timusk, T., & Richards, P. L., 1981, Appl. Opt., 20, 1355
Wang, 1991, ApJ, 374, 465
Wilbanks, T., Devlin, M., Lange, A. E., Sato, S., Beeman, J. W., & Haller, E. E., 1990, IEEE Trans. Nucl. Sci., 37, 566
Winston, R., 1970, J. Opt. Soc. Am., 60, 245
Wright, E. L., 1987, ApJ, 320, 818
Wright, E. L., et al., 1991, ApJ, 381, 200
Yamada, Y., Mitsuishi, A., & Yoshinaga, H., 1962, J. Opt. Soc. Am., 52, 17

Optical System of the Infrared Telescope in Space

Takashi Onaka, Toyoji Yagi, Hiroshi Shibai,
Hiroshi Murakami, Toshihiko Tanabé, and Tsuguo Kohno

to appear in Applied Optics

Abstract

A 15-cm Ritchey-Chretien telescope with diamond-turned metallic mirrors has been developed for use in the cryogenically cooled infrared space mission, Infrared Telescope in Space (IRTS). The IRTS is designed to resister infrared emission from 1 μm to 1 mm with a relatively wide beam (8′ to 30′ depending on the wavelength). It will be operated at superfluid helium temperatures ($\sim$ 1.8 K). We tested the performance of the telescope system both at room temperature ($\sim$ 300 K) and at near-liquid-nitrogen temperature ($\sim$ 100 K) to investigate the effects of the support stress and the temperature on the telescope. The results indicated that the Hartmann constant stays within the design goal ($\sim$ 1′) even in the worst case. The origin of aberrations is examined and possible improvements for future application are discussed.

Key Words: Astronomy, infrared telescope, metallic mirror, space probe.

T. Onaka is with the Department of Astronomy, School of Science (formerly Faculty of Science), University of Tokyo, Bunkyo-ku, Tokyo 113, Japan; T. Yagi and T. Kohno are with the Department of Mechanical Systems Engineering, Tokyo Metropolitan Institute of Technology, Asahigaoka, Hino, Tokyo 191, Japan; H. Shibai and H. Murakami are with the Institute of Space and Astronautical Science, Sagamihara, Kanagawa 229, Japan; T. Tanabé is with the Institute of Astronomy, Faculty of Science, University of Tokyo, Mitaka, Tokyo 181, Japan.

Received 18 February 1993; revised manuscript received 21 June 1993.

1 Introduction

The Infrared Telescope in Space (IRTS) is one of seven experiments on the first Space Flyer Unit (SFU-1) to be launched in early 1995 in Japan. Four scientific instruments and a near-infrared star sensor that share the focal plane of a 15-cm Ritchey–Chretien telescope cover the infrared wavelength range from 1 μm to 1 mm. Descriptions of the four instruments and the IRTS system are given in other references.[1–5] The objective of the IRTS experiment is to make the observations of both extended and point sources, and special care was taken for the elimination of stray light. This paper reports the design and the performance testing of the IRTS telescope system. The baffle design employed in the IRTS telescope system is briefly described in Ref. 1. It consists of a deployable sun-shield, a specular aperture shade, a cooled forebaffle of a Winston-type reflector, and a cold black afthaffle. Details of the design and performance tests of the cooled baffle system are to be reported in a separate paper[6].

The IRTS is contained within a 100-L liquid-helium (LHe) cryostat and will be operated at superfluid-helium temperatures ($\sim$ 1.8 K) to minimize thermal emission from the telescope system. Thus the telescope must retain its image quality at low temperatures and against thermal contraction. The SFU-1 space mission dictated a strong weight constraint on the IRTS. Because the telescope mirror is one of the heaviest parts in astronomical missions, the development of light-weight mirrors is highly desired. Another requirement imposed by the SFU-1 space mission was that the IRTS has the mechanical strength to withstand launching shock. On-board instruments were tested according to the SFU-1 requirements,[1] which imposed an acceleration of 15 G for the frequency range $24.2-100$ Hz. In general, a 15-G acceleration requires that strong supports be used for the mirrors,; however, the use of such supports contradicts the requirement that the soft supports be used to avoid extra aberrations introduced by support stress. Therefore it necessitates a special design for the mirror supports. Good thermal contact between the mirrors and the helium tank is also necessary for the stability of the mirror temperature.

Some of these requirements have been incorporated in cooled telescopes used in past and currently scheduled infrared astronomical missions. The Infrared Astronomical Satellite (IRAS),[7] launched in 1983, had beryllium mirrors that reduced the telescope weight and the effects of thermal contraction.[8,9] One of three instruments, the Diffuse Infrared Background Experiment (DIRBE), in the Cosmic Background Explorer (COBE) [10] had superpolished aluminum mirrors. The alignment of the DIRBE at a low temperature (77 K) was carefully investigated.[11] The Infrared Space Observatory (ISO) to be launched in 1995 is designed to have light-weight glass mirrors and a sophisticated mirror-support system to overcome thermal-distortion problems.[12,13]

The IRTS adopts diamond-turned aluminum mirrors for which the thermal-contraction effects should be minimal if the support system is also made of an

aluminum alloy; thus sophisticated support mechanisms may not be necessary. The use of diamond-turned aluminum mirrors has the advantages of low cost, a short manufacturing period, and less brittleness when compared to glass mirrors. They also considerably reduce the thermal-cycle time scale, giving an advantage in efficiency during instrument tests. The manufacture of metallic mirrors through numerically controlled ultraprecision cutting also allows for achievement of the highly eccentric aspherical shape of the mirror surface required by the IRTS telescope design. Metal machining enables the inclusion of extra support structures in the design. However, despite these advantages diamond-turned metallic mirrors are rather new, and their performance has to be examined carefully. Also, if they are to be used in cooled telescope applications, their low-temperature performance has to be investigated.

We tested the finished IRTS telescope system at room temperature to study the support-stress effects and at a near liquid-nitrogen (LN_2) temperature ($\sim$ 100 K) to examine the temperature effects. Changes in both image quality and focus position were investigated. Because 70% of the contraction of aluminum that occurs during the transition from room temperature to liquid-helium temperature has occurred by the time 100 K is reached, most of the temperature effects can be inferred from the test described in this paper.

The design and the specifications of the IRTS telescope system are given in Section 2. The telescope test and the measured performance at both room temperature and 100 K are described in Section 3. In Section 4, the results are evaluated in terms of the design goals and possible improvements for future applications are discussed.

2 Telescope Design

A Design Goals

Observation of both extended and point sources is the major objective of the SFU-1 IRTS mission. To achieve this objective one must maximize the results that can be obtained with small sized-apertures (15-cm in diameter). The spatial resolution of each instrument is limited either by its entrance slit size or by its diffraction size, which ranges from a minimum of 8′ to a maximum of 30′. However, better resolution was required for the telescope attitude determination with the star sensor. As a result, an image size of 1′ was set as a design goal.

Each instrument, except the Far Infrared Photometer (FIRP),[5] is located 0.96° off the optical axis, and the instruments share a common focal plane (Fig. 1). The telescope was designed to have an image size of less than 1′ at 1.13° off the optical axis [the maximum instrument off-axis dimension is the 20′ entrance slit of the Far Infrared Line Mapper (FILM)[4]]. Because the off-axis angle is relatively large, a Ritchey–Chretien telescope design was adopted. The focal-plane curvature was also taken into account in the design of the location of each instrument.

Optical System

The design parameters are summarized in Table 1; the mirror-shape figures are given by the parameters defined in the equation

$$z = \frac{Cx^2}{1 + \sqrt{1 - KC^2x^2}}, \tag{1}$$

$$C = -1/R \qquad \text{and} \qquad K = 1 - e^2. \tag{2}$$

Here x is the distance from the optical axis, z is the depth at x, R is the curvature of the radius, and e is the eccentricity. A ray-tracing calculation shows that a telescope with these parameters satisfies the requirements described above.

The placement of a baffle behind the secondary mirror is essential for the reduction of stray light (see Fig. 3 below), although it introduces the disadvantage of obscuring the collection area by approximately 30%. The effective collection area—after the obscured area is accounted for and including the support of the secondary mirror—is 113 cm^2.

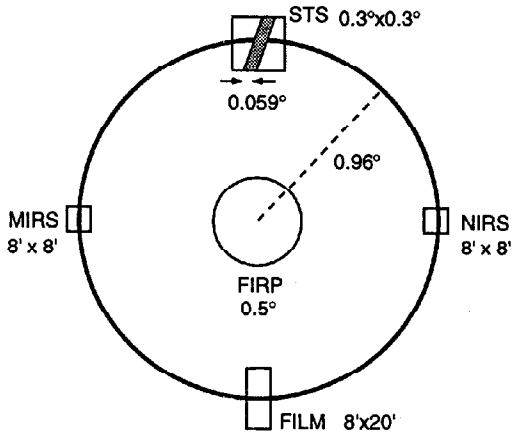

Figure 1: Designed locations of FPI's on the focal plane viewed from the telescope side. Measured locations are reported in Ref. 1. Squares and circles indicate the field of view for each instrument. A stripe in the star sensor (STS) field of view indicates a mask for accurate position determination.[1] The telescope scan direction is along the line connecting the positions of the Near-Infrared Spectrometer (NIRS) and the Mid-Infrared Spectrometer (MIRS) (horizontal). FILM is the Far Infrared Line Mapper.

Table 1. IRTS Parameters

Telescope type	Ritchey–Chretien
Effective aperture	150 mm
Focal length	600 (F/4) mm
Field of view radius[a]	$0.96° \perp 0.17°$
Image size	$< 1'$ at $0.96°$
Effective collecting area	1.13×10^4 mm^2
Back focus length[b]	64 mm at $0.96°$
Primary to secondary distance[c]	107 mm
Mirrors	
Material	aluminum alloy (A5086)
Coating (layers)	Au (0.2 μm)
	SiO_2 (0.1 μm)
Primary mirror	
Diameter (effective diameter)	154 mm (150 mm)
K^d	-0.0511
C^d	$-3.3317756 \times 10^{-3}$ mm^{-1}
Secondary mirror	
Diameter (effective diameter)	54 mm (52 mm)
K^d	-2.2025
C^d	8.7053742×10^{-3} mm^{-1}

a Each instrument is located 0.96° off the optical axis except for the Far Infrared Photometer (FIRP). The largest size entrance slit of the instruments located at 0.96° is 20′ (see Fig. 1).

b The distortion of the focal plane is taken into account and the back focus is evaluated at 0.96° off-axis.

c The actual distance was determined so as not to change the focus position by taking account of the measured shapes of the mirrors (see Fig. 2). The value indicated in this table is the design value.

d Shape parameters are defined in Eq. (1).

B Mirrors and Mirror-Support Design

The mirrors were made of an aluminum alloy (A5086) that was chosen for its capacity for high-quality ultraprecision machining. The aluminum blank was first cut by an ultraprecision cutting machine and then coated with nickel of electroless plating. After the blank was put through five thermal cycles between room temperature and the LN_2 temperature, the final cutting process was done. Only a small amount of polishing was applied at the final stage of manufacture. The

surface was finally coated with an 0.2-μm-thick layer of gold and an 0.1-μm-thickn layer of SiO_2.

The SiO_2 overcoating was applied to protect the mirror against scratching during handling and to allow easy cleaning during the integration time. However, the SiO_2 coating is known to have absorption bands in the infrared. The optimal thickness of the coating was determined with test pieces, and the final thickness chosen minimized absorption in the wavelength range longer than 1 μm. The adopted thickness of the coating was shown not to have more than 4% absorption throughout the entire 1-μm to 1-mm-wavelength range for near-normal reflection. SiO_2 also induces a polarization feature at approximately 10 μm when used at 45° reflection.[14] Because the main telescope system is used at near-normal incidence and the light rays are fairly symmetric, this effect is negligible.

The rear sides of both mirrors also were coated with Ni so as not to be bent by the difference in thermal contraction between the coating and the alloy, as indicated in Fig. 2. The attachment strength of the coating was tested by application of a thermal cycle between −40 °C and +150 °C, and attachment proved to be highly stable. The coating of the mirror has not shown any degradation after more than 20 thermal cycles between room temperature and the LHe temperature for 2 years from manufacture.

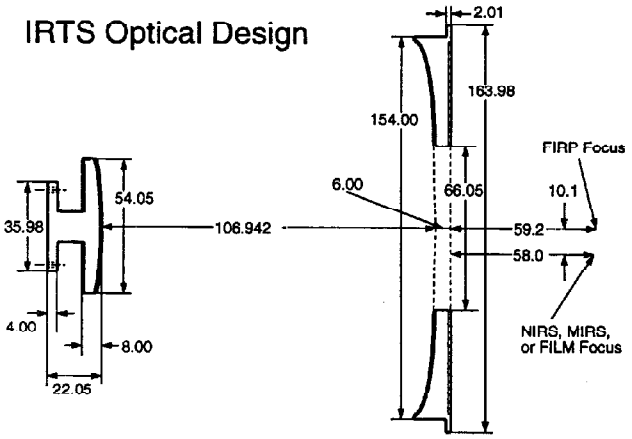

Figure 2: Optical design of the IRTS telescope. Indicated dimensions are the actual values rather than the designed ones (in mm). The striped areas indicate surfaces coated with Ni. The NIRS, MIRS, and FILM foci are located 0.96° off the optical axis, while the FIRP is located on the axis. The focal plane curvature is taken into account for the NIRS, MIRS, and FILM.

Optical System

The thickness at the edge of the primary mirror was set at 15.36 mm to meet the light weight requirement. The total weight of the IRTS telescope system including the mirrors and the mirror support was 1050 g, of which 500 g was attributed to the primary mirror.

The optical design is shown in Fig. 2 together with the dimensions of the actual mirror-surface parameters rather than the designed mirror parameters. There are no adjustable parts in the design (see also Fig. 3). The basic approach to alignment of the IRTS telescope is to rely on machining precision. However, the focus position is very sensitive to the distance between the primary and the secondary mirrors. The final distance was determined after the surface-shape figures and the thickness of the actual mirrors had been measured. Given the focus position and the known mirror-shape figures, the distance that would give the best image size in ray-tracing calculations was determined. The distance was adjusted by fine machining of the support plate of the secondary mirror (see below). Locations of all the focal instruments refer to their positions on the focal plane instrument (FPI) base plate and the telescope performance test was made referred to it.

Figure 3 shows a schematic drawing of the IRTS telescope. A complicated design for the mirror support system was avoided because space was limited and because easy assembly was desired. The primary mirror cell and the secondary mirror support were made of an aluminum alloy (6061-T6). This alloy is supposed to have a thermal-contraction ratio similar to that of alloy A5086 and to be stronger because it has been thermally treated, which results in some stress. Because it is the stress that increases the strength of the material, the thermal cycle before machining was kept to a minimum so as not to reduce the strength too much. The blank material was heated to 200 °C for 30 min once and then was subjected to two thermal cycles between room temperature and the LN_2 temperature before machining.

The primary mirror was fixed by a thin ring at its peripheral support brim (Fig. 3), and the ring was screwed to the mirror cell with 2-mm screws at 24 positions. The mirror cell was fixed to the FPI base plate at three positions with 5-mm screws. Figure 3 shows the 6 screw holes for the mirror cell. The screws holding the mirror cell were inserted in every other hole and the remaining holes were used only as stops for safety. The ring was made by regular machining. The horizontal position of the primary mirror was fixed by an inside ring that was attached directly to the FPI base plate. The mirror cell was designed to fix the mirror only at the brim as this would avoid extra stress as much as possible.

The thermal contact between the mirror and the helium tank was also considered in the design of the telescope. A heat strap of pure copper plate (2-mm thick and approximately 30-mm long) was screwed to the mirror cell and was connected to another pure copper plate that was 1-mm thick and 110-mm long and was screwed to the helium tank.

The secondary mirror has a leg and a flat stand, which was screwed directly

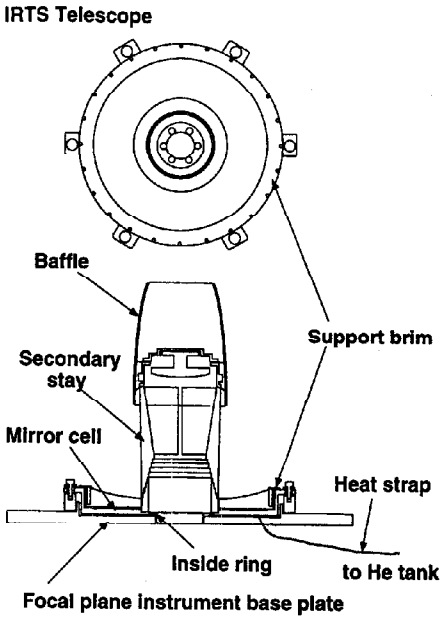

Figure 3: Schematic diagram of the IRTS telescope.

to a support plate with six 3-mm screws. Ultraprecision machining of the support plate eliminated any misalignment in the tilt of the mirror. The rear side of the mirror was finished to reflect the light specularly and was used as a reference surface during optical alignment. This surface is used when the alignment of the IRTS relative to the satellite is performed. The horizontal position of the secondary mirror was fixed to the support plate by a jig that guided the mirror when it was installed. The guide was removed after the installation of the mirror.

A vibration test at a level simulating launch conditions was conducted on the whole telescope system. It did not show any changes in alignment or image quality after the vibration test, indicating that the support system is strong enough to withstand the launching shock.

3 Telescope Test

A Test Setup

The mirrors were integrated into the telescope together with the base plate of the focal plane instruments. The whole system was installed in a test cryostat,

which permitted performance tests to be made at the LN_2 temperature. Two tests were attempted. The first was carried out to examine the image quality; the Hartmann test was employed for this purpose. The Hartmann test is a ray-tracing measurement in which light rays passing through holes on a plate—the Hartmann plate (see below)—are traced by taking images of the holes at positions ahead of and behind the focus. This provides a quantitative measurement of the deformation of the ideal surface figures. The second test measured the position and movement (if any) of the focus as the temperature changed.

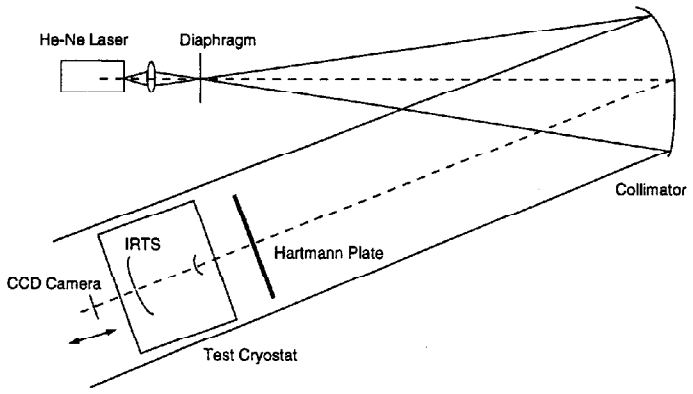

Figure 4: Schematic diagram of telescope test setup at the LN_2 temperature

The experiment setup is depicted schematically in Fig. 4. A 600-mm spherical collimator with a 6700-mm focal length converts the diverging beam from a lens placed in front of a He–Ne laser (633 nm) that is located at the focus of the collimator into a parallel beam and introduces the beam into the test cryostat. The optical alignment was based on the reflected light by the rear surface of the secondary mirror as mentioned above. The cryostat had a glass window as a vacuum seal at the front that completely covered the telescope aperture. On the other side of the cryostat a small quartz window was installed to permit observation of the beam passing out through the IRTS telescope. The effect of the back window on the converging beam was estimated and taken into account in the ray-tracing analysis. The front window was made thick enough so as not to be bent by the atmospheric pressure when the cryostat interior was in vacuum. The effect of the front window on the aberration was examined at room temperature and was found to be small ($< 5''$) compared with the required accuracy (see Table

4).

In the Hartmann test, a Hartmann plate with of 3-mm-diameter holes of 10-mm spacing was placed before the front window. The size and spacing of the holes were constrained by the diffraction and the dimensions of the detector. A CCD camera whose pixel size was 27 μm × 26 μm with an array of 256 pixels × 256 pixels was used as the detector. The spot positions were determined by averaging the data, and thus are more accurate than the pixel dimension. Because the CCD camera does not work at the LN_2 temperature, it was located outside the cryostat and registered the light rays through the back window. The camera could be moved by ±20 mm from the expected focus position to obtain both in-focus and out-of-focus images. No optics were used for the CCD; thus the actual scale of the spread to the Hartmann spots was easily estimated. The amount of CCD movement was limited by the back focus length of the telescope and the cryostat dimension. The Hartmann test was made on the optical axis at 0.5° and 1° off-axis positions if possible.

This type of Hartmann test obviously does not give the absolute position of the focus. The telescope mirror cell and the focal plane instruments are attached to the FPI base plate, which is screwed directly to the LHe cryostat. The focus position relative to the FPI base plate and its movement were measured in the following way: The focus position at room temperature was measured by another Hartmann test, in which the spot images were located on a frosted glass plate which was moved to in-focus and out-of-focus positions relative to the FPI base plate. The measurement was done at room temperature and the focus position relative to the plate was obtained. However, this method could not be used at the LN_2 temperature. Instead, the focus position at the LN_2 temperature was measured relative to that at room temperature. The glass plate was fixed at a position 20 mm ahead of the focus. A mask of 5 mm × 5 mm was put on the plate and the change of the spread of the spots relative to the mask was monitored with the camera outside of the cryostat, from which the relative movement of the focus position was estimated.

The focus position vertical to the optical axis on the base plate also was measured. The change with the temperature was monitored by a 1-mm-hole mask placed at the focus. The rear surface of the secondary mirror was used as the reference surface as before. It was found that the focus position did not change on the focal plane with temperature.

In the low-temperature test, the cryostat was evacuated for more than two days and then LN_2 was introduced into the cryostat tank. The temperature was monitored by thermometers attached to the rear side of the primary mirror and to the base plate. It took six hours to reach a stable temperature. The temperature of the primary mirror became stable near 100 K. This was probably a bit higher than the actual LN_2 temperature because of the large amount of thermal radiation coming into the mirror through the front window.

B Ray Tracing Measurement

The Hartmann test was made under several conditions: at room temperature and at near LN_2 temperature (100 K), and with the screws of the support weakly tightened (almost zero torque) and firmly tightened (2-mm screws with 2 kgf cm torque and 3-mm screws with 6 kgf cm torque).

Two mirror sets were manufactured and tested. The test results of the first set were reported in Ref. 15 in detail and are briefly summarized in the Table 2 of this paper. This paper reports mostly the results of the second set, which is to be used in the IRTS flight telescope.

The major conclusion from tests of the first set was that aberrations increased as the temperature decreased and the screws tightened but that the Hartmann constant stayed within the design goal (0.5′ at most). The circle of least confusion exceeded 2′ in the worst case, and the energy falling within a 1′ circle was estimated to be approximately 60% of the incoming flux. The design goal was therefore marginally achieved in the first mirror set.

Table 2. Results for the First Mirror Set[a]

Test Conditions			Circle of Least	Hartmann
Position	Torque[b]	Temperature (K)[c]	Confusion (′)	Constant (′)
0.0°	weak	300	1.40	0.22
0.0°	weak	100	1.62	0.32
0.0°	strong	300	1.58	0.37
0.0°	strong	100	2.18	0.48
0.5°	strong	100	2.06	0.49
0.8°[d]	strong	100	2.05	0.45

a See Ref. 15 for details.

b Almost no torque for the weak condition; and 2 kgf cm for 2-mm screws, 6 kgf cm for 3-mm screws for the strong condition.

c Room temperature was 300 K; LN_2 (cryostat) temperature was 100 K.

d The setup did not allow measurement of positions more than 0.8° off the axis position.

The image quality did not change appreciably with the off-axis position partly because the aberrations resulting from other factors were dominating. As indicated in Table 2, the aberrations were still large even at room temperature and with

a weak tightening of the screws. The errors in the surface figures of the mirrors made a significant contribution to the aberration, and those from the stress caused by contraction and tightening were relatively minor.

Based on these results, a machining process for the second mirror set was developed to reduce and to compensate for the surface figure errors found in the first set. The second mirror set had smaller errors, and the aberrations resulting from them were calculated to be small. The measured shape figure was approximated by an equation analogous to Eq. (1) as

$$z = \frac{Cx^2}{1+\sqrt{1-KC^2x^2}} + A_2x^2 + A_4x^4 + A_6x^6 + A_8x^8 + A_{10}x^{10}, \quad (3)$$

where C and K are the design values given in Table 1 and A_i (i = 2, 4, 6, 8, 10) represents the measured error coefficients given in Table 3. Spot diagrams calculated with these parameters are shown in Fig. 5 as are the aberration vectors projected on the primary mirror to indicate the characteristics of the aberrations. According to these data, the distance between the primary mirror and the secondary mirror was determined to be 106.942 mm as indicated in Fig. 2.

Table 3. Flight Mirror Parameters

Parameter	Primary Mirror	Secondary Mirror
Surface accuracy (in nm)		
Maximum roughness	8.1	8.1
Undulation [a]	< 20	< 20
Figure error	0 to +890	−120 to +150
Error coefficients[b]		
A_2	-1.49146×10^{-3}	1.29362×10^{-4}
A_4	9.26143×10^{-7}	-5.28574×10^{-6}
A_6	-2.95931×10^{-10}	2.07350×10^{-8}
A_8	4.52574×10^{-14}	-3.35997×10^{-11}
A_{10}	-2.64369×10^{-18}	1.97097×10^{-14}

a Less than the measurement errors.

b Defined in Eq. (3).

The results for various test conditions are summarized in Table 4 and some measured spot diagrams are shown in Fig. 6. The repeated measurements indicated that the reproducibility or measurement error is approximately 0.05′ in the circle of least confusion and approximately 0.01′ in the Hartmann constant. Table 4 indicates that the vacuum window and the vacuum condition did degrade the image, but the effect was relatively small (less than 5″ in total).

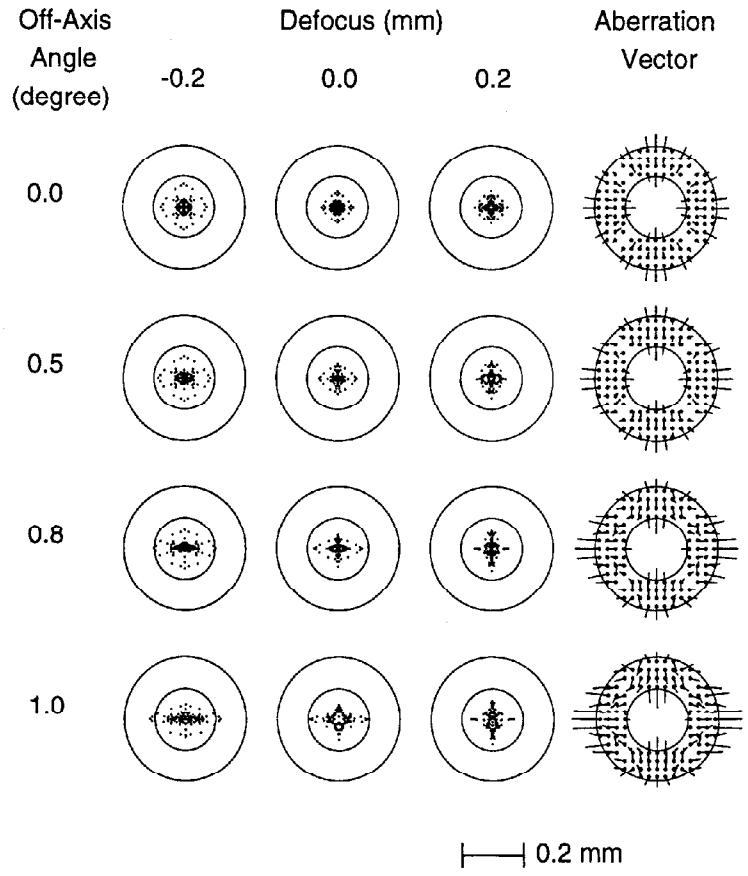

Figure 5: Calculated spot diagrams based on the measured surface figure. Diagrams at the same off-axis angles (0.0°, 0.5°, 0.8°, 1.0°) are placed in a row. In each row, spot diagrams at the best focus position and at ± 0.2 mm off-focus positions are presented and the aberration vectors are projected on the primary mirror. The radius of the bigger circle is 0.2 mm (1.1′).

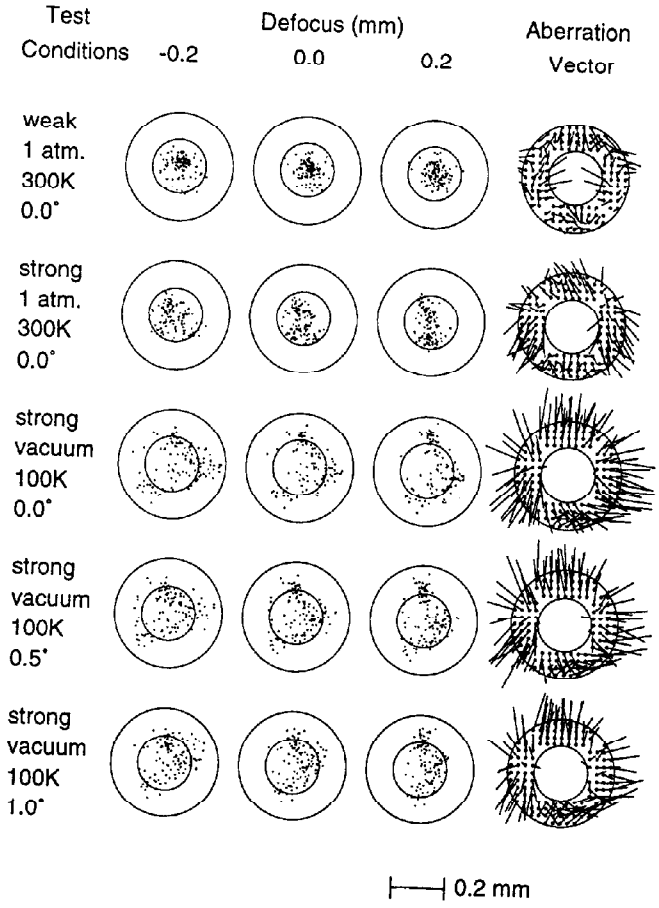

Figure 6: Measured spots of the Hartmann test under various conditions. For each condition, spot diagrams derived from the Hartmann test are shown at the best focus position and at ± 0.2 mm off of the focus position. In the rightmost column, the aberration vectors projected on the primary mirror are plotted. The scale is the same as in Fig. 5 and the larger circle radius is 0.2 mm (1.1′).

The measured pattern at room temperature without tightened screw is not much different from the ray-tracing calculation. For the second mirror set, the circle of least confusion at room temperature was smaller than that of the first mirror set, although there was not an appreciable improvement in the Hartmann constant. Thus it can be shown that the spread or the outer envelope of the image decreases, while the incident energy falling into a 1′ circle does not change when compared with the first set. Because the measured pattern is in agreement with that predicted by the ray-tracing calculation determined with the measured surface figures of the mirrors, the decrease of the size of circle of least confusion is attributed to improvement of the mirror-shape figure. This trend remains true for cases with strong screw torque. The strong torque on the screws increased the Hartmann constant by 50% and the circle of least confusion by only 5%. The spread of the rays did not increase greatly, but the energy distribution within the image changed to some degree. Strong torque produced a random undulation rather than a systematic distortion of the mirror-surface figure, probably because of a small-scale imbalance in the screw torques. Even with strong torque, however, approximately 90% of the incident energy is concentrated within a 1′ circle.

Table 4. Results for the Flight Mirror Set[a]

	Test Conditions					
Position	Torque	Temperature (K)	Front Window	Pressure	Circle of Least Confusion (′)	Hartmann Constant (′)
0.0°	weak	300	absent	1 atm	1.00	0.22
0.0°	weak	300	present	1 atm	1.08	0.22
0.0°	strong	300	absent	1 atm	1.05	0.33
0.0°	strong	300	present	1 atm	1.13	0.35
+0.5°	strong	300	present	1 atm	1.25	0.35
−0.5°	strong	300	present	1 atm	1.19	0.33
+0.8°	strong	300	present	1 atm	1.21	0.34
0.0°	strong	300	present	vacuum	1.15	0.35
0.0°	strong	100	present	vacuum	1.82	0.46
+0.5°	strong	100	present	vacuum	1.75	0.45
−0.5°	strong	100	present	vacuum	1.74	0.44
+1.0°	strong	100	present	vacuum	1.59	0.41
−1.0°	strong	100	present	vacuum	1.62	0.41

a Definitions and descriptions are the same as in Table 2.

The image quality of the second mirror set at low temperature was improved from that of the first set to a certain degree. The circle of least confusion increased with

the decrease in temperature in a ratio similar to that of the first set. The increase of the Hartmann constant with the decrease of temperature is, however, small compared with the change in circle of least confusion, thus the image concentration was not degraded appreciably. Although the difference in the Hartmann constants between the first and the second window sets is not very large, there is a clear improvement in the size of the circle of least confusion. This can be attributed to improvement of the mirror-shape figures. Figure 6 indicates that the distortion caused by strong torque increased at low temperature. It is concluded that for the second mirror set the errors in the mirror-surface figures are no longer a major source for the aberrations, and the stresses resulting from the screw torque and thermal-contraction effects became dominant. The time limitation was very severe in the IRTS project; thus no attempts were made to improve the mirror-support mechanism. Nonetheless the image size is shown to be within the design goal even in the worst case. Thus, it is concluded that the initial design goal has been achieved for the IRTS telescope.

C Focus Position

In the optical alignment test, the focus position in the focal plane was approximately 2′ off from center if the light reflected on the rear side of the secondary mirror is considered to be a reference surface. This degree of error from the machining processes is not unexpected and is not significant in the optical alignment. However, it has to be incorporated in the data analysis of the actual attitude determination. The alignment of the telescope to the satellite attitude-control system will be made with an alignment mirror attached to the IRTS cryostat, which is aligned to the rear surface of the secondary mirror.

The positions of the focus in the optical path direction was found to be +0.5 mm off from the designed position. The position moves with temperature and at the LN_2 temperature it is −0.5 mm away from the focus at room temperature. In total the focus is approximately on the design-goal position for the LN_2 temperature. The thermal effect is predicted to cause approximately −0.2 mm of movement of the focus position when changing from room temperature to the LN_2 temperature. The extra movement could be due to the temperature gradient remaining in the telescope at the cooled test, and this gradient may disappear during the actual observations because incoming thermal radiation in space will be much lower than in the laboratory. The distance of the change in focus position is, however, nearly the same as the error in the measurement. Thus it would be appropriate to conclude that the errors in the focal position in the optical axis direction do not exceed 0.5 mm. Because the F ratio of the telescope beam is 4, this leads to an out-of-focus image size of 1.5′ at most, which may be larger than the change in image size resulting from the measured aberrations described above. The actual image size at operating temperatures similar to those expected during actual observations can be estimated by the beam-pattern measurement of each

instrument. Although the size of the entrance slit for each instrument is not small enough to make a precise measurement, we have not found serious degradations in image size greater than the design value of 1′.[1–4]

4 Summary

A metallic-mirror telescope for the Infrared Telescope in Space mission, IRTS, was designed and tested. The IRTS mission requires a relatively wide field of view because of the four scientific instruments sharing the focal plane. Highly eccentric aspherical mirror shapes were needed to meet the design goals, and an ultraprecision machining technique made achievement of the goals possible. We reduced the weight of the primary mirror, which dominates in the weight in the telescope, to some extent by making the mirror thin. The metallic mirror also permitted the use of the easily fabricated mirror support. The support system was not extensively investigated in the present study because of the time limitation.

The image quality of the telescope was measured with the Hartmann test at both room and the LN_2 temperature. It was shown that the image quality obtained with the metallic-mirror telescope at room temperature could be estimated fairly well from measurements of the mirror surface if the screws in the support were not tightened firmly. Although the aberration caused by the mirror support was not dominant in the first productions of the mirrors, it became an important factor when the shape error was improved. The machining precision should be improved in the future. Thus the development of good mirror support system should be of utmost importance for future applications. In other words, it is expected that if the support system is good enough, the performance of the metallic mirror telescope can be inferred with reasonable accuracy from measurements taken at room temperature. The movement of the focus position also was found to be fairly small. No special adjustments in the mirror positions except those for correcting the figure errors, which can be known in advance, was needed. A metal mirror adequately met the requirements of this mission and was easier to mount and to heat sink than a glass mirror.

The tests described in this paper showed that the IRTS telescope has met its design goals for image quality at least at the LN_2 temperature. It should also be added that the measurements were done with a He–Ne laser (633 nm) and only the geometrical aberration was investigated. When applied in the infrared wavelength, diffraction may become more important and the effects of geometrical aberration may be less significant. The image quality at a number of wavelengths was examined at the superfluid helium temperature during each instrument calibration test and did not prove to be noticeably degraded.[1–3] Thus it is suggested that the IRTS design goal for the expected operating conditions also was achieved and that the measurements at the LN_2 temperature provide a reasonable simulation of the experiment at the LHe temperature as far as the effects of temperature

on the metallic-mirror telescope are concerned.

This work was carried out as part of the IRTS project. The IRTS project is managed and operated by the Institute of Space and Astronautical Science (ISAS) in collaboration with the NASA Ames Research Center; the University of California, Berkeley; the University of Nagoya, and the University of Tokyo. We are deeply indebted to all the members of the IRTS project, and the encouragement and the efficient support of H. Okuda, and T. Matsumoto are particularly appreciated. T. L. Roellig is acknowledged for reading the manuscript and making useful comments. The heat strap was prepared and installed by the FIRP group. The mirrors were made by NIKON Corporation, and the artistic telescope structures were designed and fabricated by Mitaka-koki. We thank NIKON for providing us with the mirror data and for having carefully read the draft. T. Onaka is grateful for the support by the Kurata foundation in the late stage of this work.

T. Yagi is now with Nippon Denso Company, Showa-machi, Kariya, Aichi 448, Japan.

References

1. H. Murakami, J. Bock, M. Freund, H. Guo, T. Hirao, A. E. Lange, H. Matsuhara, T. Matsumoto, T. J. McMahon, M. Murakami, T. Nakagawa, M. Noda, K. Noguchi, H. Okuda, K. Okumura, T. Onaka, T. L. Roellig, S. Sato, H. Shibai, T. Tanabe, T. Watabe, T. Yagi, N. Yajima, and M. Yui, "The Infrared Telescope in Space (IRTS)," Astrophys. J. (accepted for publication).

2. M. Noda, T. Matsumoto, S. Matsuura, K. Noguchi, M. Tanaka, and M. A. Lim, "Near-infrared spectrometer on the Infrared Telescope in Space," Astrophys. J. (accepted for publication).

3. T. L. Roellig, T. Onaka, T. J. McMahon, and T. Tanabe,"The mid-infrared spectrometer on the Infrared Telescope in Space," Astrophys. J. (accepted for publication).

4. H. Shibai, M. Yui, H. Matsuhara, N. Hiromoto, T. Nakagawa, and H. Okuda, "Far-Infrared Line Mapper (FILM) on IRTS," Astrophys. J. (accepted for publication).

5. A. E. Lange, M. Freund, S. Sato, H. Hirao, T. Matsumoto, and T. Watabe, "The far-infrared photometer on the Infrared Telescope in Space," Astrophys. J. (accepted for publication).

6. J. J. Bock, A. E. Lange, H. Matsuhara, T. Matsumoto, T. Onaka, and S. Sato, "Performance of a cooled baffle system for space-borne infrared telescopes," Appl. Opt. (submitted for publication).

7. G. Neugebauer, H. J. Habing, R. van Duinen, H. H. Aumann, B. Baud, C. A. Beichman, D. A. Beintema, N. Boggess, P. E. Clegg, T. de Jong, J. P. Emerson, T. N. Gautier, F. C. Gillett, S. Harris, M. G. Hauser, J. R. Houck, R. E. Jennings, F. J. Low, P. L. Marsden, G. Miley, F. M. Olnon, S. R. Pottasch, E. Raimond, M. Rowan-Robinson, B. T. Soifer, E. G. Walker, P. R. Wesselius, and E. Young, "The Infrared Astronomical Satellite (IRAS) Mission", Astrophys. J. (Lett.) **278**, L1–L6 (1984).

8. W. Irace and D. Rosing, "The IRAS telescope", J. Br. Interplanet. Soc. **36**, 27–33 (1983).

9. N. Harned, R. Harned, and R. Melugin, "Alignment and evaluation of the cryogenic corrected Infrared Astronomical Satellite (IRAS) telescope," Opt. Eng. **20**, 195–200 (1981).

10. J. C. Mather, "The Cosmic Background Explorer (COBE)," Opt. Eng. **21**, 769–774 (1982).

11. T. J. Magner, "Diffuse Infrared Background Experiment (DIRBE) optics module breadboard alignment methods and results," Opt. Eng. **26**, 264–269 (1987).

12. C. Singer, J. A. Massoni, B. Moβbacher, and C. Cinotti, "The Infrared Space Observatory," in *Space Astronomical Telescopes and Instruments*, P. Y. Bely and J. B. Breckinridge, eds., Proc. Soc. Photo-Opt. Instrum. Eng. **1494**, 255–264 (1991).

13. E. Ruch, "The manufacture of ISO mirrors," in *Space Astronomical Telescopes and Instruments*, P. Y. Bely and J. B. Breckinridge, eds., Proc. Soc. Photo-Opt. Instrum. Eng. **1494**, 265–278 (1991).

14. G. Hass, J.B. Heaney, H. Herzig, J. F. Osantowski, and J. J. Triolo, "Reflectance and durability of Ag mirrors coated with thin layers of Al_2O_3 plus reactively deposited silicon oxide," Appl. Opt. **14**, 2639–2644 (1975).

15. T. Yagi, H. Shibai, T. Onaka, and T. Kohno, "Hartmann Test of the Infrared Telescope in Space (IRTS) at Low Temperature", Rep. 69 (Institute of Space and Astronautical Science, Sagamihara, Kanagawa 229, Japan, 1990) pp.1–17.

Acronyms

A		
	ARC	NASA Ames Research Center
B		
	BICE	Balloon-borne Infrared Carbon Explorer
	BIRT	Balloon-borne Infrared Telescope
C		
	CCD	Charge-Coupled Device
	CDMS	Command and Data Management System (SFU)
	CMB	Cosmic Microwave Background Radiation
	CMOS	Complementary Metal-Oxide Semiconductor
	COBE	Cosmic Background Explorer (NASA)
	CRL	Communications Research Laboratory
D		
	DEP	Dedicated Experiment Processor (SFU)
	DIRBE	Diffuse Infrared Background Experiment (COBE)
	DMR	Differential Microwave Radiometer (COBE)
	DPU	Data Processing Unit (SFU)
	DSN	Deep Space Network (NASA)
E		
	EBL	Extragalactic Background Light
	ESA	European Space Agency
F		
	FILM	Far-Infrared Line Mapper (IRTS)
	FIRAS	Far-Infrared Absolute Spectrophotometer (COBE)
	FIRP	Far-Infrared Photometer (IRTS)
	FOV	Field of View
	FPI	Focal Plane Instrument
	FPI-E	FPI Electronics
	FWHM	Full Width at Half Maximum
G		
	GPS	Global Positioning System

Acronyms

I		
	IPAC	Infrared Processing and Analysis Center
	IPD	Interplanetary Dust
	IRAS	Infrared Astronomical Satellite
	IRTS	Infrared Telescope in Space
	ISAS	Institute of Space and Astronautical Science
	ISD	Interstellar Dust
	ISM	Interstellar Matter
	ISO	Infrared Space Observatory (ESA)
J		
	J-FET	Junction Field Effect Transistor
	Jy	Jansky (10^{-26} W m^{-2} Hz^{-1})
K		
	KAO	Kuiper Airborne Observatory (NASA)
L		
	LPF	Low-Pass Filter
	LRS	Low Resolution Spectrometer (IRAS)
	LWS	Long Wavelength Spectrometer (ISO)
M		
	MIRS	Mid-Infrared Spectrometer (IRTS)
N		
	NEP	Noise Equivalent Power
	NIRS	Near-Infrared Spectrometer (IRTS)
	NASA	National Aeronautics and Space Administration
	NASDA	National Space Development Agency
P		
	PAH	Polycyclic Aromatic Hydrocarbon
	PLU	Payload Unit (SFU)
S		
	SAA	South Atlantic Anomaly
	SFU	Space Flyer Unit
	SIRTF	Space Infrared Telescope Facility (NASA)
	SL	Star Light
	SOC	Sagamihara Operations Center (SFU)
	STS	(1) Space Transportation System (NASA) (2) Star Sensor (IRTS)
T		
	TGF	Thick-Grill Filter
	TIA	Transimpedance Amplifier

Acronyms

U

USEF	Institute for the Unmanned Space Experiment Free Flyer

V

VCS	Vapor-Cooled Shield

Z

ZL	Zodiacal Light

The production of this reprint is financially supported in part by the Scientific Research Fund of the Ministry of Education, Science, and Culture, Japan, under Grant No.05452022 (T. Nakagawa).